Numerical studies on complex axisymmetric flows using axisymmetric lattice Boltzmann method

F Morakabi

PhD 2023

Faculty of Science and Engineering

Numerical studies on complex axisymmetric flows using axisymmetric lattice Boltzmann method

Farokh Morakabi

A thesis submitted in partial fulfilment of the requirements of Manchester Metropolitan University for the degree of Doctor of Philosophy

Department of Computing and Mathematics
Manchester Metropolitan University

2023

Abstract

The lattice Boltzmann method (LBM) has proven to be an effective numerical technique for computational fluid dynamics (CFD). It has numerous advantages over traditional computational methods such as finite element and finite difference approaches. The method's simplicity, easy treatment of boundary conditions, and parallel programming features make it ideal for solving large-scale real-world problems. In this thesis, the development and use of a lattice Boltzmann model for both steady and unsteady two-dimensional axisymmetric flows are presented. Three-dimensional (3D) Navier-Stokes equations describe axisymmetric flows, which can be solved using the three-dimensional (3D) lattice Boltzmann method. Such 3D equations become 2D axisymmetric flow equations when cylindrical coordinates are used. The cavity flow benchmark has been used in our study to verify the axisymmetric lattice Boltzmann revised model(AxLAB®) for more complex axisymmetric flows in a cylindrical container. Also, systematic research on vortex breakdown has been done in a closed cylindrical container with one or two rotating lids. Furthermore, an investigation was carried out into unsteady-periodic flow in the cavity to see how the flow behaviour can be predicted. To the author's knowledge, this is the first numerical study to determine the periodicity of such flows. The formation of vortex breakdowns, their frequency, and the locations of stagnation points as the flow pattern enlarges are all explained in depth. In addition, the second-order bounce-back technique is introduced to the model for no-slip boundary conditions to increase the accuracy of the AxLAB®. The magnitude of the maximum axial velocities along the cylinder axis, their locations, and the locations of stagnation points have all been analysed to demonstrate the advantages of the described method. The most recent experimental and numerical approaches are then used to compare the results, indicating that the new method provides more accurate results in detail. Also, a more advanced version of AxLAB® is developed to model turbulent flows. By incorporating the conventional subgrid-scale stress (SGS) model into the axisymmetric lattice Boltzmann equation in a way that is consistent with lattice gas dynamics, the turbulent flow is effectively and naturally represented. By using the model to simulate two common engineering scenarios, (i) pipe flow through an abrupt axisymmetric constriction, and (ii) axisymmetric separated-reattached flow, the model is proven to be accurate. Analysis of the axial velocity profile and the reattachment length reveals how much more comparable the outcomes are to other experimental and computational methods, particularly in the region close to the wall domain, as a result of using the second-order bounce back method for the wall boundary conditions. The result demonstrates that the second-order bounce-back method in the upgraded AxLAB® is straightforward and has a higher level of accuracy than AxLAB® in its ability to predict axisymmetric turbulent flows as well as laminar flows.

Plagiarism Declaration

All information contained in this thesis, with the exception of any statements to the contrary, is the result of my own work. Furthermore, no parts of this material were taken or copied from other sources. I am aware that using data from unrecognised third parties or showing signs of plagiarism will be treated very seriously. Signed

Farokh Morakabi

Acknowledgements

I want to express my gratitude to my PhD project supervisor, Dr. Jian Guo Zhou, for all of his support, encouragement, and advice. His persistence, inspiration, zeal, and breadth of knowledge not only helped me at every stage of my research and thesis writing, but also served as a model for me to follow in the future.

My family and friends, who are the foundation of my strength, have my sincerest gratitude. Without their help, understanding, and love, I would not have been able to complete this job.

I want to use this opportunity to thank everyone who supported me during my PhD studies.

Contents

List of Figures

List of Tables

List of Abbreviations and Symbols

Abbreviations

1D	One dimensional
2D	Two dimensional
3D	Three dimensional
AxLAB	Axisymmetric lattice Boltzmann method
AxLAB®	Revised Axisymmetric lattice Boltzmann method
BGK	The single time relaxation approximation
BGK-LBM	Lattice Boltzmann method using BGK scheme
CFD	Computational fluid dynamics
CBE	Continuous Boltzmann equation
CA	Cellular automata
D2Q4	4-velocity square lattice
D2Q7	7-velocity square lattice
D2Q9	9-velocity square lattice
DNS	Direct numerical simulation
FDM	Finite difference methods
FEM	Finite element methods
FH	Method proposed by Filippova and Hanel
FHP	Model designed by Frisch, Hasslacher and Pomeau
FVM	Finite volume methods
HPP	Model designed by Hardy, de Pazzis and Pomeau

LABSWE	The lattice Boltzmann model for shallow water equations
LABSWE$^{\text{TM}}$	The lattice Boltzmann model for shallow water equations with turbulence modelling
LABSWE$^{\text{MRT}}$	The lattice Boltzmann model for shallow water equations with multiple relaxation-time
LBM	Lattice Boltzmann method
LES	Large-eddy simulation
LGA	Lattice gas automaton
LGCA	Lattice gas cellular automata
MRT	Multiple-relaxation-time
N-S	Navier-Stokes
PDF	Particle Distribution Function
SGS	Subgrid-Scale Stress model
BEM	Boundary Element Method

Symbols

Ω_α	is the collision operator,
M	is the number of directions of the particle velocities at each node,
P	is the pressure,
i, j	are space direction indices,
e_r, e_φ, e_z	are the standard orthonormal unit vectors,
φ	is coordinate in the azimuth direction,
r, x	are the coordinates in radial and axial directions,
δ_{ij}	is the Kronecker function,
k	is the turbulent kinetic energy ,
ε	is the turbulent dissipation rate,
$\overline{u_i}$	is the space-filtered velocity component in i direction,

G	is a spatial filter function,
τ_{ij}	is the subgrid-scale,
ν_e	is the eddy viscosity,
C_S	is the Smagorinsky constant,
l_s	is the characteristic length scale,
S_{ij}	is the magnitude of the large scale strain-rate tensor,
$\overline{\acute{u}_i\acute{u}_j}$	is the Reynolds stress tensor,
f_α	is the distribution function of the particles,
$\acute{f}$	is the value of distribution function before the stream,
e_α	is the velocity vector of a particle in the α link,
Δt	is the time step,
$\mathbf{X}$	is the space vector,
Δx	is the lattice size,
f_α^{eq}	is the local equilibrium distribution function,
ζ	is a relaxation time,
f_{eq}	is the Maxwell-Boltzmann equilibrium distribution function,
ω_α	is the weight,
ρ	is the fluid density,
θ	is the source or sink term,
F_i	is the force term,
$e_{\alpha i}$	is the component of e_α, which is the velocity vector of a particle in the α link,
τ_α	is the relaxation time,
ν	is the Newtonian fluid kinematic viscosity,
τ	is the Newtonian fluid relaxation time,
u_{ij}	is the velocity,
τ_t	is the relaxation time for turbulent flow,
τ_e	is the eddy relaxation time,
τ_f	is the wall shear stress vector,
C_f	is the friction factor at the wall,

τ_{fi}	is the wall shear stress,
$\bar{f}_\alpha$	is the distribution function for axisymmetric flows with swirl,
$\bar{f}_\alpha^{eq}$	is the local equilibrium distribution function for axisymmetric flows with swirl,
S_ϕ	is the source or sink term,
$\overline{e_\alpha}$	is the velocity vector of a particle on the D2Q4,
$\overline{\tau_\alpha}$	is effective relaxation time for rotation fluid,
$\overline{\tau}$	is the Newtonian fluid relaxation time for rotation fluid,
u_ϕ	is the azimuthal velocity,
H	is the height of the cylinder,
Re	is the Reynolds number,
e_x, e_y	is the particle velocity in the x and y directions respectively,

Chapter 1

Introduction

Simulating fluid flows with basic arithmetic computations rather than intricate flow equations is no longer a pipe dream, but a reality [1]. This is the fundamental concept behind the lattice Boltzmann technique, which is distinguished by its straightforward approach, parallel process, and simple and efficient treatment of boundary conditions [2]. The development of the lattice Boltzmann method (LBM) continues rapidly, as its numerous potential capabilities continue to be realized and demonstrated in different areas[3]. It has become a very successful computational method in interdisciplinary subjects, far beyond the original intention of simulating fluid flows described by the Navier-Stokes equations. Numerous computing methods are available to solve the Navier-Stokes equations, including the finite difference scheme, finite element method, finite volumes, spectral methods, Boundary Element Method (BEM)and lattice Boltzmann methods. To simulate complicated problems, these techniques require a long execution time, especially when dealing with complex boundary conditions. All of the aforementioned characteristics give the lattice Boltzmann approach a significant advantage over other numerical methods. Although originally designed to mimic fluid flows represented by the Navier-Stokes equations, LBM has since been enhanced and expanded to cover a wide range of flow issues. Swift et al. [4] used the lattice Boltzmann technique to model nonideal fluids, for example. The Brinkman equation was solved by Spaid and Phelan, Jr. [5] using the lattice Boltzmann technique. Zhou created lattice Boltzmann models for shallow and groundwater flows[6, 7]. In practice, axisymmetric flows represent a variety of essential flow challenges. The three-dimensional lattice Boltzmann technique has been used to simulate 3D axisymmetric flows using cubic lattices and curved boundary treatment. This indicates that one or more dimensional lattices are required for the modelling of such flows, reducing efficiency. 3D axisymmetric flows are fundamentally 2D issues in a cylindrical coordinate system. In order to take advantage of this property, Halliday et al.[8] initially investigated the lattice Boltzmann technique for axisymmetric flows in 2001. Halliday et al. incorporated two source terms and retrieved the macroscopic equations for axisymmetric flow. Halliday et al.'s solution has since been successfully applied to a number of axisymmetric flow problems. However, one term ($\frac{u_x u_r}{r}$) within the momentum equation associated with radial speed is overlooked in their formulation, where u_x and u_r are axial velocity and radial velocity components consecutively and r is the radius of the pipe. Lee et al.[9] observed that this mistake results in large errors for axisymmetric flows with considerable radial velocities in non-straight pipes. This mistake was corrected by Lee at al. who demonstrated an accurate solution for flows in which the radial velocity components cannot be overlooked. In addition, the method of Halliday et al.[8] has been extended to multiphase flow by Premnath and Abrahamand [10] and two-phase flow with a large density ratio by Shiladitya and Abraham [11]. Recently, Reis and Phillips[12] expressed the source terms in Halliday et al.' equation without the error made by Halliday et al. Despite this, the second source term involves velocity gradients, which may introduce additional errors and causes numerical instability. A complete lattice Boltzmann model for axisymmetric flows without or with swirling within the framework of the lattice Boltzmann approach is provided by Guo et al[13]. Later, Li et al.[14] gave an improved axisymmetric lattice Boltzmann scheme including the rotational effect. The key drawbacks of these methods are that: (a) the source or force terms are more complicated than those in the original governing equations, (b) due to the elimination of implicitness in the schemes, the equations for computing macroscopic variables, such as velocities, acquire complex forms rather than the typical simple sum of the distribution functions, complicating the algorithm, and (c) They gave their own expression for the viscosity that differs from the conventional definition in lattice Boltzmann dynamics. . In addition, Zhou[15] extended an axisymmetric lattice Boltzmann method without swirl. The force term introduced in this method contains velocity gradients, which is its only disadvantage. Therefore, Zhou[2] reformulated the original axisymmetric lattice Boltzmann approach to eliminate the requirement for calculations of the velocity gradients, while all the advantages of the original model are maintained. Compared to the Navier-Stokes equations, the source terms are identical to those in the governing equations with the exception of the velocity gradients, thus enabling straightforward consideration of more physical phenomena. Also, the standard calculations for density and velocity used in the conventional lattice Boltzmann method for fluid flows are preserved, unlike other existing simplified models. Also, one more distribution function is formulated for the solution of the azimuthal velocity Fig. 1.1 to boost the revised model with similar characteristics for generic axisymmetric flows involving swirling. This new method has been applied to simulate the vortex breakdown phenomenon for steady and unsteady cylindrical cavity flows and the results are compared with analytical solutions, demonstrating its accuracy and applicability. In Fig. 1.1, the θ direction typically refers to the circumferential direction. Cylindrical coordinates are defined using three coordinates: (r, θ, z), where r is the radial distance from the z-axis, θ is the azimuthal angle, and z is the vertical distance along the z-axis.

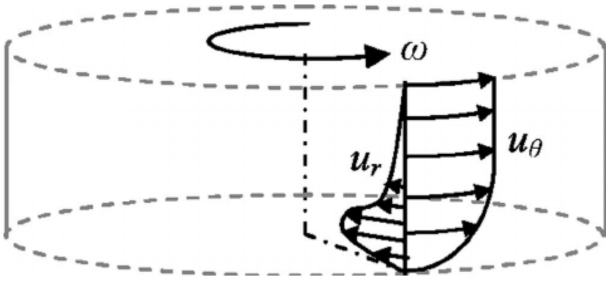

Figure 1.1: Sketch of the azimuthal and radial velocity profiles

1.1 Problem Definition

In the present work, vortex breakdowns in swirling flow are further investigated, and simulations of the flow in cylindrical containers with rotating endwalls are performed. Two parameters govern the flow behaviour in a cylindrical container: the height-to-radius ratio (Aspect ratio) $A = \frac{H}{R}$ and the rotation Reynolds number $Re= \Omega \frac{R^2}{\nu}$, where Ω is the constant angular velocity, R is the radius, H is the cylinder height, and ν is the kinematic viscosity. The rotating endwall of a closed container functions as a pump, and the spiraling motion of the flow inside the cylinder increases the swirl velocity, resulting in the vortex breakdown phenomena. The velocity profile and the reattachment length for turbulent flows are also investigated. Two engineering applications Are simulated using the novel code created for turbulent flows to demonstrate its capabilities. In the first case study, turbulent flow through an abrupt axisymmetric contraction is examined. A numerical analysis of turbulent flow in an axisymmetric separated and reattached flow through a longitudinal blunt circular cylinder is conducted as a case study.

1.2 Importance of the Problem

Swirling flows are frequently observed in nature such as tornadoes and typhoons, and have been employed for decades in technological applications including aeronautics, heat exchange, spray drying, separation, combustion, chemical mixing, etc. Swirling flows are created by a uniformly rotating infinitely long plane disk and vortex breakdown occurs in swirling flow when there is a drastic change in flow structure. In order to achieve flame geometries and heat release rates suitable for a particular production application, swirling flows have been used to improve and control the mixing rate between fuel and oxidant streams in combustion systems, such as in gas turbine engines, diesel engines, industrial burners, and boilers [16]. When there is enough swirl, an internal recirculation zone is created, allowing rapid heat release as the recirculated combustion products ignite the incoming fuel/oxidant streams. This creates a steady, compact flame [17] that performs well with challenging carboneous materials and poor gases [18].

In Figs. 1.2, 1.3, 1.4 and 1.5 a few industrial application of swirl flows are shown.

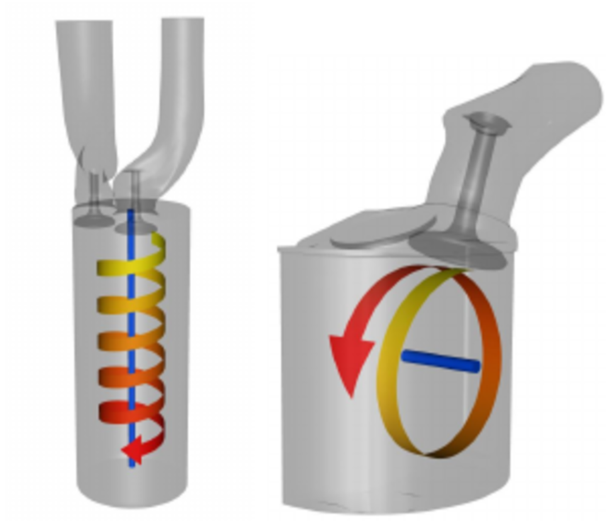

Figure 1.2: The swirling motion of flow in the combustion chamber of a diesel engine Swirl

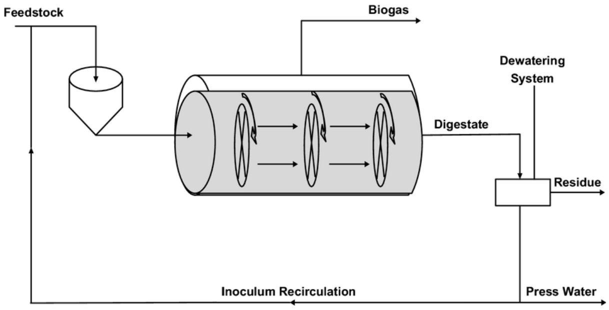

Figure 1.3: Horizontal plug flow bioreactor design with inoculum recirculation

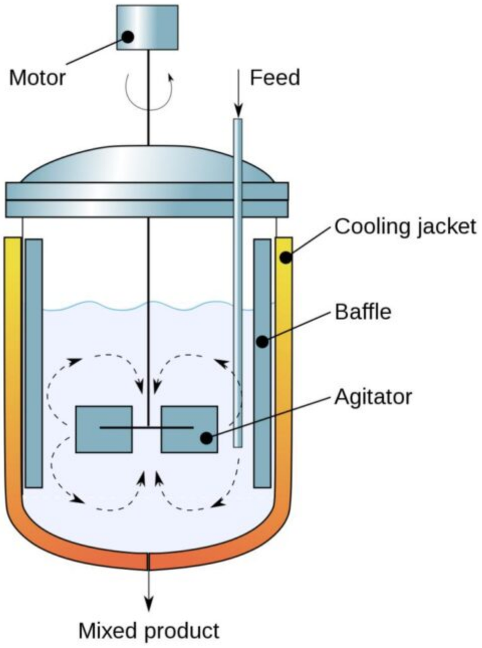

Figure 1.4: Chemical Process Mixing

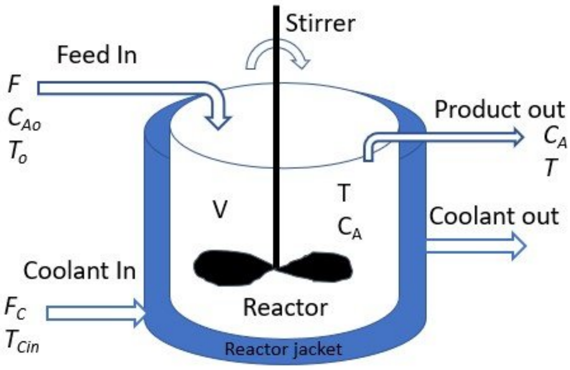

Figure 1.5: Continuous Stirred Tank Reactor (CSTR)

There is a need for further study of the vortex breakdown phenomenon to improve the performance of industrial machines and enhance their efficiency [19]. Moreover, the majority of flows, whether created naturally or artificially, are turbulent, a most important challenge in classical physics. When laminar flow transforms to turbulent flow, industrial machinery uses more fuel and operates less effectively due to the fluid's increased friction and resistance. In order to solve this problem and improve the efficiency of industrial equipment that contain turbulent flows, we must first use very accurate numerical algorithms to anticipate the flow behaviour as exactly as possible, leading to a better understanding of the flow characteristics. These improvements decrease greenhouse gas emissions and achieve low-level economic power generation which is one of the most important issues the world struggles with these days[20].

1.3 Outline of the Thesis

In Chapter 1, the research background, the research gaps, importance of the project and various numerical methods for solving the Navier-Stokes equations are introduced, a brief summary of the development and application of LBM in recent years is given, and the purpose and goals of this thesis are outlined.

The literature review in Chapter 2, discusses how and why the lattice Boltzmann method has evolved into one of the most effective methods for resolving the Navier-Stokes equations. To solve the Lattice Boltzmann Equation (LBE) a few models are also briefly explored, and also some details are provided about rotating flow and turbulent flow.

In Chapter 3, the governing N-S equations and their axisymmetric flow equations for laminar flow and turbulent flow, are briefly discussed.

The fundamentals of lattice Boltzmann techniques are introduced in Chapter 4. Two models are developed to simulate axisymmetric flows with or without swirl, and the derivation and theory for the axisymmetric lattice Boltzmann model are also presented. An overview of the recovery process for the axisymmetric flow equations is provided.

The initial and boundary conditions used in the lattice Boltzmann method are discussed in Chapter 5. No-slip, semi-slip, and slip boundary conditions are discussed in this chapter.

Chapter 6 briefly describes the subgrid-scale (SGS) stress model and how to combine it with AxLAB® for turbulence modelling. This chapter also contains the recovery procedure.

Several steady and unsteady flows in cylindrical containers with rotating end walls were simulated and analysed in Chapter 7. The process of determining the flow period for an unsteady-periodic flow is also described.

In Chapter 8, the second-order bounce-back method is used for no-slip boundary conditions in cylindrical containers, and the results are compared to other numerical and experimental studies. The results obtained from AxLAB and the new code are compared, demonstrating the consequence improvements in accuracy.

Chapter 9 describes two turbulent axisymmetric LBM simulations. The accuracy of the turbulence model with the second-order bounce-back method for no-slip boundary conditions is ascertained by comparison between the results of the previous and new code.

Conclusions and recommendations for future work are presented in Chapter 10.

Chapter 2

Literature Review

2.1 Background

Water flowing down rivers, air moving through the atmosphere, ocean currents, and blood flowing through the human body are all examples of fluid flow phenomena that are prevalent in nature. Fluid flows are subject to laws of conservation of mass and momentum. These conservation principles may be used to create a set of differential equations that reflect such flows. The Navier-Stokes (N-S) momentum equations and the continuity equation were developed in the middle of the nineteenth century to represent flow characteristics. Ongoing to the nonlinearity of the Navier-Stokes equations no analytical solution exists for the general governing equations, except for a few simple cases. Numerical solutions of the Navier-Stokes equations have been developed using computational fluid dynamics (CFD) methods such as the finite difference method (FDM), finite volume method (FVM), finite element method (FEM) and etc. Each has their own list of benefits. The Finite Difference Method (FDM) is non-conservative but easy to code. the Finite Element Method (FEM) is conservative but more difficult to code. The Finite Volume Method (FVM) combines the advantages of both FDM and FEM [21]. All the foregoing can be implemented on unstructured grids. The axisymmetric flow equations are frequently solved using the FVM, which can straightforwardly handle complicated geometries using unstructured meshes [22].

Murthy and Mathur used unstructured polyhedral meshes to extend the FVM to compute radiation in axisymmetric geometries [23]. The node-centred FVM employing an edge-based data structure, introduced by Lyra et al. [24], is very adaptable in handling control volumes of various shape connected to generic unstructured meshes. The N-S equations may be directly solved using these CFD techniques, and recovering the independent variables, velocity and pressure in space and time. These traditional CFD techniques rely on macroscopic level discretization of macroscopic continuum equations. At the microscopic level, the fluid contains atoms and molecules, and its behaviour of a fluid can be predicted by simulating molecular interactions and individual molecule movements. However, given that so many molecular movements must be computed, this microscopic calculation approach takes significantly longer than the conventional CFD method at the macroscopic level, a flaw in this approach. The mesoscopic scale, which lies halfway between these two computation scales, may be utilised to mimic the fluid system as well as other physical processes. Compared to the molecular dynamics approach, this theory takes into account a significantly smaller number of fluid "particles". A fluid "particle" is, in other words, a sizable collection of molecules. Even so, the size of the fluid' particle' is much smaller than the macroscopic simulation's smallest length scale for the macroscopic physical properties. In the late 1940s, Ulam, von Neumann, and Zuse created a cellular automata model at mesoscale [25]. Since then, the cellular automata approach it has undergone additional development and evolved into a highly potent instrument for modelling a variety of scientific issues [26, 27]. In a monograph, Zuse put forward a hypothesis regarding the numerous physical issues that cellular automata (CA) may solve [28]. The HPP (Hardy, de Pazzis, and Pomeau) lattice gas cellular automata were first proposed by Hardy et al. in 1973 [29]. Since then, research has been done on both one- and two-dimensional CA. Examples are Fredkin's game and Wolfram's four universal classes CA. Conway invented the well-known two-dimensional "Game of Life" in the 1970s [30]. This exemplifies the CA's key characteristic, which is that it can imitate very challenging physical issues in the actual world using just a few basic principles. In fact, several applications have demonstrated that CA is very straightforward to apply to a range of challenging phenomena [25, 31].

2.2 Lattice Gas Automata

Lattice gas automata (LGA) is a subtype of cellular automata. It is based on regular lattices of microscopic space, time, and particle velocitY[6]. Each such particle travels at its own speed and direction from one lattice unit to another. Collisions between two or more incoming particles are possible. The explicit conservation of mass and momentum, which is a key component in replicating actual physical issues, is a key characteristic of LGA. In fact, the Navier-Stokes equation for incompressible flow is asymptotically equal to summations of the micro-dynamic mass and momentum equations [32].

Hardy et al.[29]'s HPP model, the simplest LGA model for two-dimensional flows, was the first totally discrete model of a fluid. However, the N-S equations cannot be derived from this model using the HPP approach because of inadequate lattice symmetry. Instead, the N-S equations can be recovered by the corrected lattice gas automaton (FHP model) that Frisch et al. [33] presented.

LGA typically involves two sequential steps: a collision phase and a streaming step. Each particle moves at its own velocity to the nearest node along the streamwise directions, during the streaming step. Subsequently, when the particle velocity components at a given node are altered in accordance with the presumed rules, a collision occurs. At the macroscopic level in physics, these two stages replicate convection and diffusion, respectively.

Numerous issues arise with the LGA for the Navier-Stokes equations, including the nonisotropic advection component, fictitious invariants, numerical noise, etc. [34]. The lattice Boltzmann model was therefore created in response to this need.

2.3 Lattice Boltzmann Methods

The Lattice Boltzmann Method (LBM) was first hypothesized to deal with the deficiency of the Lattice Gas Automata (LGA) and to improve lattice gas cellular automata (LGCA) modelling [34], which used Boolean logic to simulate the flow by tracing the movement of particles on a discrete lattice. The lattice Boltzmann equation can be written by [35]:

$$f_\alpha(\mathbf{x}+e_\alpha, t+1) = f_\alpha(\mathbf{x}, t) + \Omega_\alpha[f_(\mathbf{x}, t)] \qquad \alpha = 0, 1, \cdots, M, \tag{2.1}$$

where f_α is the distribution function of particles; t is the time; e_α is the local constant particle velocity; $\mathbf{x}$ is the space vector; Ω_α is the collision operator, and M is the number of directions of the particle velocity components at each node. The fluid density ρ and velocity u_i can be calculated from

$$\rho = \sum_\alpha f_\alpha, \tag{2.2}$$

$$u_i = \frac{1}{\rho}\sum_\alpha e_{\alpha i} f_\alpha. \tag{2.3}$$

By providing an indirect solution to the incompressible Navier-Stokes (N-S) equations, the lattice Boltzmann method (LBM) is a relatively recent numerical technique for modelling complicated flows [35, 36]. LBM is established upon the microscopic kinetic equation for the particle distribution function (PDF), in contrast to classical CFD methods (such FDM and FVM), and the PDF defines the macroscopic variables. The LBM has a number of benefits: it is easy to program. The non-linear macroscopic advection terms are recovered in the streaming step and collision step, hence a single tow-stage loop is sufficient in LBM systems. Furthermore, when simulating the incompressible flow, the pressure in LBM satisfies a straightforward equation of state. Therefore, while simulating incompressible flow, it is not essential to solve the Poisson equation using iteration or relaxation methods, unlike conventional CFD methods. The numerical approach is simple to parallelize since LBM is explicit and non-iterative [37].

LBM, like other CFD techniques, has certain drawbacks notably the majority of calculations for the current LBM are for low-velocity flows; for more complicated flows, such as multiphase flows and porous flows, additional calculation terms must be included. Also, LBM has more disadvantages and limits, such as Accuracy for Complex Flows, Boundary Conditions, and Limited Numerical Stability.

2.4 Single Relaxation Time (SRT)

The Lattice Bhatnagar-Groos-Krook (LBGK) equation, based on the Single Relaxation Time (LBM-SRT) approximation, is the most basic LBE [38]. The LBGK equation is the most often used Lattice Boltzmann equation due to its remarkable simplicity. This approach, nevertheless, has several disadvantages. Stability issues can occur at a limiting value, for instance, in flow simulation at high Reynolds numbers, a key component of the LBM-SRT [39]. Given that the inherent Mach number of the model must be maintained as low as possible, incompressible flows are constrained in their flow velocities. The collision frequency is pushed toward the stability limit as a result of the decreased kinematic viscosity needed to achieve high Reynolds numbers for flow past certain body shape. By shrinking the size of the lattices, the collision frequency may be increased, but more computing power is required [40]. Alternatively, employing LBM-MRT raises the stability limit.

2.5 Two-Relaxation Time (TRT)

Ginzburg [41] suggested that the distribution function may be divided into symmetric and antisymmetric portions to address difficulties arising from advection-diffusion, timing, and stability. Servan-Camas and Tsai [42] used a similar approach for the advection-diffusion equation and attained second-order accuracy and decreased third-order numerical errors while maintaining the solution inside the linear stability zone.

2.6 Multi-Relaxation Time (MRT)

In the previous section, a single relaxation method was used to address several issues. There is evidence indicating that multi-relaxation systems offer greater accuracy and stability than a single relaxation scheme [43]. LBM initial matrix formulations serve as the foundation for Multiple Relaxation Times (MRTs), which shorten the computing time [44]. Additionally, MRT outperforms SRT in higher Reynolds number flow simulations, particularly in terms of numerical stability [45]. As a result, the distribution functions are linearly transformed to the velocity moments, allowing the collision term to be represented by a n x n matrix, where n is the number of lattice velocity components. This approach permits more latitude with the macroscopic quantities, enabling the moment of the equations to exert additional control [46]. The MRT has improved symmetry for the lid-driven cavity and can model flows of lower viscosity [47].

2.7 Axisymmetric Lattice Boltzmann Model

Numerous fluid problems with axial symmetry are encountered in practice. Examples include the collision of two binary droplets head-on [48], the continuous rise of a bubble [49], and the movement of shallow water and groundwater [7]. To model 3D axisymmetric flows utilising cubic lattices with a curved boundary condition, the three-dimensional (3D) lattice Boltzmann technique was created [50, 51, 52]. Theoretically, a cylindrical polar system can be used to reduce the 3D Navier Stokes (N-S) equations for axisymmetric flows to 2D flow equations. As a result, it is conceivable to create a lattice Boltzmann technique for 3D axisymmetric flows that is less complicated and will take much less time to compute. A source term in the Navier-Stokes equations may be incorporated into the LBE in order to fully utilise this capacity and model axisymmetric flow. Multiple spatial and velocity-dependent source components have been proposed for inclusion in the common lattice Boltzmann equation to imitate the extra axisymmetric contributions to 2D Navier-Stokes equations in cylindrical dimensions [53, 54, 55]. However, it's critical to recognise and emphasise the assumption's limitations, especially when working with flows that are essentially three-dimensional in nature. Flows in complex geometries, turbulent flows, and those involving swirling or vortical motion, for example, cannot always be accurately represented using a purely axisymmetric or asymmetric assumption. Researchers must evaluate the special characteristics of the flow, the simulation's aims, and the computational capabilities available. When considering whether to employ an asymmetry assumption in their simulations, engineers and researchers should carefully assess the consequences of choosing between computing expense and accuracy. Compare the simulation results to the experimental data or known analytical solutions whenever possible, and conduct the grid-independent test help researchers to understand the reliability of research findings.

The majority of axisymmetric lattice Boltzmann techniques, however, are documented in the literature for laminar axisymmetric flow equations in the absence of turbulence. However, these approaches are not immediately applicable because the majority of real-world natural flows are turbulent. In general, flow turbulence is modelled as a closure problem using $k - \epsilon$ model [56], where k is turbulent kinetic energy and ϵ is turbulent dissipation rate, which provides time-averaged characteristics. For turbulent flows, Teixeira [57] first proposed the lattice Boltzmann method, which transforms the single relaxation time into a variable relaxation time governed by resolving two differential equations, namely the $k - \epsilon$ equations. Employment of space-filtered governing equations with a subgrid-scale (SGS) stress model for the unresolved scale stress allows the large eddy simulation to effectively reproduce vertical structures that are larger than a prescribed scale. The Smagorinsky [58] subgrid-scale is typically used in space-filtered governing equations to model flow turbulence because it is the most straightforward and accurate method representing flow included turbulence. The space-filtered flow equations are utilised in the current study because, in accordance with Tutar and Hold's research [59], they are more precise than the time-averaged counterpart for calculating turbulent flows. The lattice Boltzmann approach for simulating turbulence may integrate the conventional Smagorinsky SGS stress model, as demonstrated by Hou et al. [60] who changed the single relaxation time into a variable relaxation time that is directly connected to the distribution function thus eliminating the need to carry out any derivative computations. A lattice Boltzmann model for the shallow water equations with turbulence modelling (LABSWE^{TM}) was created by Zhou [61] following Hou et al.[60], who determined its effectiveness and applicability for turbulence modelling [62].

2.8 Study of Rotational Flows

Axisymmetric flows with swirl or rotation are often encountered in engineering practice [63, 64]. However, axisymmetric flow with swirl exhibit more complicated features than axisymmetric flow without swirl. For many years, both computational and experimental studies of the flow in a closed cylindrical container with a rotating lid have been conducted. In 1968, Vogel [65] conducted an initial set of trials. The flow created in a cylindrical container by a spinning end wall was observed in studies by Ronnenberg [66] and Escudier [67], who discovered the development of a concentrated vortex core along the centre axis. Numerous experimental and numerical investigations have since been conducted as a result of the studies of Ronnenberg and Escudier. The existence of vortex breakdown bubbles in steady-state flow was experimentally investigated by Spohn et al. [68]in a closed cylindrical container with a rotating bottom. The electrolytic precipitation method was utilised to depict flow features, and a particle tracking method was employed to describe the overall flow field. Later, Sotiropoulos et al. [69] performed preliminary experiments that confirmed their early numerical findings of the occurrence of chaotic behaviour in Lagrangian transport with vortex-breakdown bubbles in steady flows. In order to study axisymmetric vortex breakdown, Lopez [63, 70, 71] published three studies between 1990 and 1992. In 2001, the three-dimensional structure of restricted whirling flows with vortex breakdown was investigated by Sotiropoulos et al. [72, 73]. In addition to one-sided rotation, experts

[74] believe two-sided rotation can offer fresh perspectives on these issues and provide new suggestions on how to manage the vortexes.

Experimental research on the effects of co- and counter-rotation of the end wall of a cylinder on vortex breakdown was conducted by Bar-Yoseph et al. [75], Gautier et al. [76], and Fujimura et al. [77]. Co-rotating end walls with the same angular velocity were examined in calculations by Valentine and Jahnke [78] and Lopez [79] for both steady and turbulent swirl flow. The lattice Boltzmann approach has recently drawn considerable interest from non-Newtonian fluid dynamics researchers. Based on the LBM, Yoshino et al. [80] suggested a numerical model for non-Newtonian fluid flow and addressed two test case problems: non-Newtonian fluid flow in a three-dimensional porous structure and power-law fluid flow in a radial corner geometry. Their computer simulations showed that LBM can be effective for simulating real-world non-Newtonian fluid flows. LBM was utilised by Wang and Bernsdorf [81] to analyse blood flow using the Carreau Yasuda model. Non-Newtonian and Newtonian flows were compared in their study in a three-dimensional (3D) generic stenosis.

Later, utilising LBM, many researchers created their own models to analyse axisymmetric flows. Halliday et al.'s model [8] was extended by Niu et al. [82], who incorporated the azimuthal rotation effect with the rotation terms regarded as inertia forces. Halliday's technique was attended to axisymmetric thermal systems by Peng et al. [83]. The azimuthal velocity component and temperature were estimated using finite differences in addition to the radial and axial velocity components solved by the lattice Boltzmann formulation. A revised version of the D2Q9 model proposed by He and Luo [84] was also suggested by Huang et al. [85, 86, 87], which had better numerical stability and a less compressibility impact. With the inner cylinder rotating, Huang et al. created a hybrid lattice Boltzmann system for axisymmetric flows. Azimuthal velocity and temperature equations were discretized using the finite difference approach, whereas the axial and radial velocities were solved using the two-dimensional lattice Boltzmann equation with source terms. A newer axisymmetric approach, appropriate for all axisymmetric flows, was devised by Zhou [15], in which the force and source/sink components were naturally incorporated into the lattice Boltzmann (LB) equation. An updated axisymmetric lattice Boltzmann approach was reported in 2011 by the same author [2]. The axisymmetric lattice Boltzmann model for cylindrical Couette flows for non-Newtonian fluid was later analytically solved by An et al. [88]. A more reliable incompressible axisymmetric D2Q9 model still needs to be constructed in order to increase numerical stability and remove the compressibility impact of ordinary LBM.

2.9 Study of Turbulent Flows

It is important to be able to examine turbulent flow from both perspectives. Using the Navier-Stokes equations and the continuity equation, it is theoretically possible to model such flows. However, a vast number of scales are encountered in turbulent flow and it is difficult to use typical approach to get the same results as experimentally. Direct numerical simulation (DNS) is the most conceptually obvious method of solving the Navier-Stokes equations. At present, the Reynolds (Re) numbers seen in most industrial applications and the corresponding time resolution meshes make the DNS technique computationally unfeasible except for tiny domain [89]. There are two main alternatives to the direct numerical simulation method for addressing turbulent flows. First, through time-averaging, the Reynolds-Averaged Navier-Stokes (RANS) theory avoids a complete resolution of the time and space history of turbulence. The second option is large-eddy simulation (LES) based on The idea of convolution with a spatial filter. Only these scales determined by the diameter of the filter are to be computed using LES. The PDE system of laws is subjected to a filtering process, producing a set of space-filtered Navier-Stokes equations. Joseph Smagorinsky was the first to present the Large Eddy Simulation concept [58]. According to Tennekes and Lumley [90], turbulent flow has the following characteristics:

- Turbulent flow has a spectrum of eddy sizes and is irregular, random, and chaotic.
- As the Reynolds number Re rises, the diffusivity in turbulent flow also rises. This implies that momentum exchange increases.

- Turbulent flow relates to high Reynolds numbers. As an illustration, turbulent axisymmetric pipe flow usually occurs when $Re > 4000$ [91], where $Re = uD/\nu$.
- There are always three dimensions to turbulent flow. However, such flows can exhibit two-dimensional properties and exists in practice as a two-dimensional flow issue when the governing equations are time-averaged or space-filtered [90].
- Turbulent flow is dissipative because the kinetic energy of tiny eddies is converted into internal energy by bigger eddies. The energy is extracted from the mean flow by the greatest eddies. This type of procedure is known as a cascade process [90].
- Despite the presence of eddies of various magnitude, the flow should still be thought of as a continuum.

  Unresolved small-scale impacts on big-scale dynamics must be incorporated when utilising the LBM to solve a high Reynolds number flow; otherwise, the outcomes will be unstable. According to Sterling and Chen [92], the LBM may be thought of as an explicit second-order finite-difference discretization approach. Two approaches have been suggested to extend the LBM to the small-scale dynamics of turbulent flows. Hou et al. [60] claimed that the LBM can be used to model large-scale motions and the lattice gas technique will simulate small-scale dynamics noting that LBM originated from the LGA method and lattice gas dynamics comprises tiny scale fluctuations. The other approach is significantly more straightforward and enables the LBM to be used in conjunction with a conventional subgrid model. This strategy was used by Benzi et al. [93] and Qian et al. [94], who both obtained acceptable results. The conventional Smagorinsky model [95], which employs positive eddy viscosity to simulate small-scale energy damping, is one of the most basic subgrid models. Hou et al. [60] discussed the conventional subgrid model and included its natural incorporation into the LBM's framework. Following the same principle as Hou et al.[60], Zhou [61] has created a lattice Boltzmann model for the shallow water equations with turbulence modelling (LABSWE$^{\text{TM}}$). Zhou also demonstrated the model's effectiveness and applicability for turbulence modelling [62]. Meanwhile, several alternative approaches to flow turbulence modelling have been proposed. Krafczyk et al. [96] created a large eddy simulation for the Navier-Stokes equations using a multiple-relaxation-time (MRT) lattice Boltzmann model. Similar research has been undertaken by Yu et al. [97] using the MRT lattice Boltzmann model to simulate the flow of a turbulent square jet.

2.10 Study of Vortex Breakdown Phenomenon

According to Benjamin [98], vortex breakdown involves an abrupt and extreme change in velocity structure that occasionally takes place in a whirling flow. However, despite decades of study, the physical process that causes vortex breakdown is still poorly understood. In the first kind of breakdown, the core expands quickly and creates a bubble-like shape that is almost axisymmetric. In the second type of breakdown, the vortex centerline spirals outward without appreciable core size expansion. The axial flow, which is required for vortex breakdown, decelerates along the vortex axis- an important feature of vortex breakdown. The general direction of axial flow is typically reversed inside the bubble. Peckham and Atkinson [99], Elle [100], and Lambourne and Bryer [101] all provide descriptions of early experimental work on vortex breakdown. In these experiments, spiral and bubble types of breakdown were observed, with one or more stagnation points appearing on or near the axis of the vortex. Michaud provided schematics showing breakdowns observed in tornadoes and waterspouts at various stages of their lifecycle [102]. Vortex breakdown appears as the 'eye' in hurricanes, which is a silent region with little known about the formation process and characterization of the eye. Sharma and Sameen [103] recently demonstrated that axisymmetric vortex breakdown prevents mixing by acting as a barrier to fluid transport. Vogel-Escudier [65, 67] flow is created by generating bubble-type vortex breakdown inside a circular cylinder with a rotating top lid.

2.11 Research Gaps

There is a lack of numerical studies of the vortex breakdown phenomenon and systematic simulations of unsteady-periodic cavity flows to find out the periodic time where the flow repeats itself. Furthermore, there is a shortage of high-accuracy numerical methods to simulate turbulent flows with complex boundary conditions. To fill research gaps, there is a need for systematic simulation of vortex breakdown for $1002 < Re < 3061$ and $2 < A < 3.5$, giving a solution for determining the flow periodicity, implementing the 2nd order BC to provide more precise results, and incorporating flow turbulence.

2.12 Aim and Objectives

The aim of this thesis is to utilise an enhanced version of the axisymmetric lattice Boltzmann method called AxLAB® to solve the axisymmetric equations of motion for a cylindrical container with a rotating wall. The overall objectives are

- To systematically simulate vortex breakdowns for $1002 < Re < 3061$ and $2 < A < 3.5$, compare the results to experimental data and determine the axial velocity component of the flow along the cylinder axis.
- To identify the period of vortex breakdown for A specific kind of unsteady-periodic flow with $Re = 2765$ and $A = 2.5$. The maximum axial velocity components of this flow along the cylinder axis will be used to calculate the absolute error and relative error between two patterns and hence estimate the period time. Knowledge of the period time enables us to predict and control the behaviour of unsteady-periodic flow aims improving industrial machine performance.
- To apply the new bounce back boundary method [104] for the axisymmetric lattice Boltzmann revised method. This method is of second-order accuracy enabling us to improve the accuracy of AxLAB® for boundary conditions concerning the flow in a cylindrical container with rotating top and bottom walls. ResultS obtained from

AxLAB® and the new code will be compared to demonstrate the improvements in accuracy.

- We will also incorporate flow turbulence into the new model to simulate complex flows such as turbulent pipe flow through an abrupt axisymmetric constriction and axisymmetric separated and reattached flows. Velocity components, reattachment length and streamlines will be examined, and numerical and experimental test cases used to validate the code. The results from AxLAB® and the new code will again be compared to demonstrate that the second-order bounce back method, when used in conjunction with AxLAB® for turbulent flows, yields more accurate results.

Chapter 3

Governing Equations for Axisymmetric Flows

3.1 Introduction

The laws of momentum and mass conservation apply to fluid flows. A set of differential equations are developed to represent the physical movement of a fluid flow based on these conservation rules. The Navier-Stokes (N-S) momentum equations and the continuity equation make up a common set of governing flow equations. Axisymmetric flow equations with and without turbulence terms, the governing equations in axisymmetric flows, and the continuity of N-S equations are all discussed in this chapter.

3.2 The Navier-Stokes Equations

The three-dimensional continuity and Navier-Stokes (N-S) equations, which are respectively derived from the principle of mass conservation and Newton's second law of motion, are the governing equations for general incompressible flows. In Cartesian coordinates; the continuity equation of an incompressible fluid may written

$$\frac{\partial u}{\partial x} + \frac{\partial v}{\partial y} + \frac{\partial w}{\partial z} = 0 \tag{3.1}$$

The Navier-Stokes momentum equations are

$$\frac{\partial u}{\partial t}+u\frac{\partial u}{\partial x}+v\frac{\partial u}{\partial y}+w\frac{\partial u}{\partial z}=\nu(\frac{\partial^2 u}{\partial x^2}+\frac{\partial^2 u}{\partial y^2}+\frac{\partial^2 u}{\partial z^2})-\frac{1}{\rho}\frac{\partial p}{\partial x}+f_x \tag{3.2}$$

$$\frac{\partial v}{\partial t}+u\frac{\partial v}{\partial x}+v\frac{\partial v}{\partial y}+w\frac{\partial v}{\partial z}=\nu(\frac{\partial^2 v}{\partial x^2}+\frac{\partial^2 v}{\partial y^2}+\frac{\partial^2 v}{\partial z^2})-\frac{1}{\rho}\frac{\partial p}{\partial y}+f_y \tag{3.3}$$

$$\frac{\partial w}{\partial t}+u\frac{\partial w}{\partial x}+v\frac{\partial w}{\partial y}+w\frac{\partial w}{\partial z}=\nu(\frac{\partial^2 w}{\partial x^2}+\frac{\partial^2 w}{\partial y^2}+\frac{\partial^2 w}{\partial z^2})-\frac{1}{\rho}\frac{\partial p}{\partial z}+f_z \tag{3.4}$$

where x, y and z are Cartesian coordinates; u, v and w are the corresponding velocity components; f_x, f_y and f_z are the body force components per unit mass; ν is the kinematic viscosity; p is the pressure; ρ is the fluid density; and t is the time. Another way to express the above equations in tensor form is as follows:

$$\frac{\partial u_j}{\partial x_j}=0, \tag{3.5}$$

$$\frac{\partial u_i}{\partial t}+u_j\frac{\partial u_i}{\partial x_j}=f_i-\frac{1}{\rho}\frac{\partial p}{\partial x_i}+\nu\frac{\partial^2 u_i}{\partial x_j\partial x_j}, \tag{3.6}$$

where i and j are space direction indices; and f_i is the body force per unit mass acting on the fluid in the i direction. The left side of Eq. 3.6 represents inertia, with the second term on the left representing convection. The three terms listed in order on the right-hand side are the body force term, the pressure gradient term, and the viscous diffusion term. The N-S equations have no analytical solution except for a few very simple cases. It is increasingly feasible to obtain numerical solutions to the continuity and N-S equations as computing power grows. In order to solve flow issues in engineering, numerical approaches are becoming increasingly routine.

3.3 Governing Equations in Axisymmetric Flows

3.3.1 Laminar Flow

Consider the movement of an isotropic, incompressible fluid through a three-dimensional tube. The conventional orthonormal unit vectors $\mathbf{e}_r, \mathbf{e}_\phi$ and $\mathbf{e}_z$ define a cylindrical coordinate system:

$$\mathbf{e}_r = (\frac{x}{r}, \frac{y}{r}, 0), \tag{3.7}$$

$$\mathbf{e}_\phi = (\frac{y}{r}, -\frac{x}{r}, 0), \tag{3.8}$$

$$\mathbf{e}_z = (0, 0, 1). \tag{3.9}$$

in which case ϕ is the azimuth, $r = \sqrt{x^2 + y^2}$, $x = rcos\phi$ and $y = rsin\phi$. If the solution to the Navier-Stokes equations has the form

$$\mathbf{u} = u_r(r, z)\mathbf{e}_r + u_z(r, z)\mathbf{e}_z, \tag{3.10}$$

the flow is said to be axisymmetric (without swirl) as the velocity field **u**is independent of ϕ. In cylindrical coordinates, the continuity equation is

$$\frac{\partial u_r}{\partial r} + \frac{u_r}{r} + \frac{\partial u_z}{\partial z} = 0, \tag{3.11}$$

and the N-S momentum equations are:

$$\frac{\partial u_r}{\partial t} + u_r \frac{\partial u_r}{\partial r} + u_z \frac{\partial u_r}{\partial z} = -\frac{1}{\rho}\frac{\partial p}{\partial r} + \nu(\frac{\partial^2 u_r}{\partial r^2} + \frac{1}{r}\frac{\partial u_r}{\partial r} - \frac{u_r}{r^2} + \frac{\partial^2 u_r}{\partial z^2}), \tag{3.12}$$

$$\frac{\partial u_z}{\partial t} + u_r \frac{\partial u_z}{\partial r} + u_z \frac{\partial u_z}{\partial z} = -\frac{1}{\rho}\frac{\partial p}{\partial z} + \nu(\frac{\partial^2 u_z}{\partial r^2} + \frac{1}{r}\frac{\partial u_z}{\partial r} + \frac{\partial^2 u_z}{\partial z^2}). \tag{3.13}$$

The tensor form representation of the governing equations for incompressible axisymmetric flow in a cylindrical coordinate system is as follows:

$$\frac{\partial u_j}{\partial x_j} = -\frac{u_r}{r} \tag{3.14}$$

$$\frac{\partial u_i}{\partial t} + u_j \frac{\partial u_i}{\partial x_j} = -\frac{1}{\rho}\frac{\partial p}{\partial x_j} + \nu \frac{\partial^2 u_i}{\partial^2 x_j} + \frac{\nu}{r}\frac{\partial u_i}{\partial r} - \frac{\nu u_i}{r^2}\delta_{ir}, \tag{3.15}$$

where ρ is the density; p is the pressure; r and x are the coordinates in radial and axial directions, respectively; i is the index standing for r or x; u_i is the component of velocity in the i direction; ν is the kinematic viscosity; t is time; δ_{ij} is the Kronecker δ function defined by

$$\delta = \begin{cases} 0, & i \neq j, \\ 1, & i = j, \end{cases} \tag{3.16}$$

and repeated indexes imply summation over space coordinates, known as the Einstein summation convention. Substitution of the continuity Eq. 3.14 into Eq. 3.15 results in [14]

$$\frac{\partial u_i}{\partial t}+\frac{\partial (u_i u_j)}{\partial x_j} = -\frac{1}{\rho}\frac{\partial p}{\partial x_j}+\nu\frac{\partial}{\partial x_j}\left(\frac{\partial u_i}{\partial x_j}+\frac{\partial u_j}{\partial x_i}\right)+\frac{\nu}{r}\left(\frac{\partial u_i}{\partial r}+\frac{\partial u_r}{\partial x_i}\right)-\frac{u_i u_r}{r}-\frac{2\nu u_i}{r^2}\delta_{ir}. \tag{3.17}$$

3.3.2 Turbulent Flow

Concepts for Space Filtering

Large eddy simulation (LES) computes only the scales determined by the filter's diameter, in contrast to DNS, which resolves all scales in the flow. The main function of LES is low-pass filtering, which involves retaining scales associated with low frequencies while filtering out scales related with high frequencies. Thus, the flow parameters that characterise the flow (such as velocity, pressure, etc.) are divided into the resolved scales and the resulting unresolved scales. The space-filtered Navier-Stokes equation can yield greater accurate solutions to turbulent flows and can reveal precise properties of flow turbulence, while being more expensive to utilise than the time-averaged Reynolds equations, according to a large body of research [54]. Therefore, turbulent flows in this work are simulated using LES. The convolution process in traditional LES defines the resolved larger-scale motion. The space-filtered conservation equations are created by convolving the conservation principles with a spatial filter function during the filtering operation. A generalised filter is described by Leonard [105] as a convolution integral,

$$\tilde{u}_i(X,t) = \int G(X-\xi)u_i(\xi,t)d\xi, \tag{3.18}$$

where the integration is conducted over the full domain, ξ is a variable in domain, and the filter G, is normalised by requiring that

$$\int G(X-\xi)d\xi = 1. \tag{3.19}$$

The residual field is defined by the difference between the space-filtered quantity, $\tilde{u}_i(X,t)$, and the actual solution, $u_i(X,t)$, given by

$$\acute{u}_j(X,t) = u_i(X,t) - \tilde{u}_i(X,t). \tag{3.20}$$

By adding a space-filtered quantity to the continuity equation (Eq. 3.5) and momentum equation (3.6), the flow equations for the large eddy simulation may be constructed. The Navier-Stokes equation and space-filtered continuity are represented as:

$$\frac{\partial \tilde{u}_i}{\partial x_j} = 0, \tag{3.21}$$

$$\frac{\partial \tilde{u}_i}{\partial t} + \frac{\partial(\tilde{u}_i\tilde{u}_j)}{\partial x_j} = f_i - \frac{1}{\rho}\frac{\partial p}{\partial x_i} + \nu\frac{\partial^2 \tilde{u}_i}{\partial x_j \partial x_j} - \frac{\partial \tau_{ij}}{\partial x_j}, \tag{3.22}$$

The subgrid-scale stress, abbreviated τ_{ij}, measures the interaction between the resolved and unresolved scales, i.e.

$$\tau_{ij} = u_i u_j - \tilde{u}_i\tilde{u}_j. \tag{3.23}$$

Concepts for Time-Averaged Model

In general, the Navier-Stokes equations, the Reynolds equations, space-filtered Navier-Stokes equations, large eddy simulation, or Direct Numerical Simulation (DNS) may all be used to explain turbulent flows. In DNS of turbulent flow, there is no need for closure models because DNS explicitly solves the Navier-Stokes equations for all scales of turbulence [106]. The variables in turbulent flows are split into two categories in time-averaged models: the perturbation category and the category that represents the time-averaged variation. Consider the velocity, which is

$$u_j = \bar{u}_j + \acute{u}_j, \tag{3.24}$$

where u_j is the universal variable, $\acute{u}_j$ is the perturbation part and $\bar{u}_j$ is the time-averaged part, which can be calculated from

$$\bar{u}_j = \frac{1}{T}\int_t^{t+T} u_j dt. \tag{3.25}$$

By incorporating of Eq. 3.25 into N-S equations Eq. 3.5 and Eq. 3.6 we have

$$\frac{\partial \bar{u}_j}{\partial x_j} = 0, \tag{3.26}$$

$$\frac{\partial \bar{u}_i}{\partial t} + \frac{\partial(\bar{u}_i\bar{u}_j)}{\partial x_j} = f_i - \frac{1}{\rho}\frac{\partial p}{\partial x_i} + \nu\frac{\partial^2 \bar{u}_i}{\partial x_j \partial x_j} + \frac{1}{\rho}\frac{\partial \tau_{ij}}{\partial x_j}, \tag{3.27}$$

where the new term $\tau_{ij} = -\rho\overline{\acute{u}_i\acute{u}_j}$ is called the Reynolds stress, which may be represented in terms of the mean strain rate using the Boussinesq approximation [107],

$$\tau_{ij} = -\rho\overline{\acute{u}_i\acute{u}_j} = -\rho\nu_t(\frac{\partial \overline{u_i}}{\partial x_j} + \frac{\partial \overline{u_j}}{\partial x_i}). \tag{3.28}$$

.

There are several degrees of approximation that may be used to close the set of governing equations Eq. 3.26 and Eq. 3.27 as discussed below.

1. Models using zero equations. Eddy viscosity in this model is determined by a straightforward algebraic relation as follow

$$\nu_t = l_m(l_m\frac{dU}{dy}), \tag{3.29}$$

the mixing length of turbulence motion l_m is calculated experimentally [108].

2. One-equation models. Typically, these models solve the transport equation for a

specific turbulent quantity, such as turbulence kinetic energy κ, and then derive a second turbulent quantity using an algebraic formula [109].

$$\nu_t = C_\mu \sqrt{\kappa} l_m. \tag{3.30}$$

$$\frac{\partial \kappa}{\partial t} + U_j \frac{\partial \kappa}{\partial x_j} = \frac{1}{\rho} \tau_{ij} \frac{\partial U_i}{\partial x_j} - \varepsilon + \frac{\partial}{\partial x_j} \left[\frac{1}{\rho} (\mu + \frac{\mu_t}{\sigma_\kappa}) \frac{\partial \kappa}{\partial x_j} \right] \tag{3.31}$$

C_μ is a constant established by Launder and Spalding [108] using basic benchmark tests and ε is the rate of turbulent dissipation.

3. Models with two equations. Two partial differential equations are used in this model to explain two transport scalars. The commonly used k-ε model is an example of a typical two-equation model [110],

$$\nu_t = C_\mu \frac{k^2}{\varepsilon} \tag{3.32}$$

$$\rho u_j \frac{\partial k}{\partial x_j} = \rho \tau_{ij} \frac{\partial u_i}{\partial x_j} + \frac{\partial}{\partial x_j} \left[\left(\mu + \frac{\mu_t}{\sigma_k} \right) \frac{\partial k}{\partial x_j} \right] - \left[\rho \varepsilon + 2\mu \left(\frac{\partial k^{\frac{1}{2}}}{\partial x_j} \right)^2 \right], \tag{3.33}$$

$$\rho u_j \frac{\partial \varepsilon}{\partial x_j} = C_1 \frac{\varepsilon}{k} \tau_{ij} \frac{\partial u_i}{\partial x_j} + \frac{\partial}{\partial x_j} \left[\left(\mu + \frac{\mu_t}{\sigma_\varepsilon} \right) \frac{\partial \varepsilon}{\partial x_j} \right] - C_2 \frac{\rho \varepsilon^2}{k} + \frac{2\mu\mu_t}{\rho} \left(\frac{\partial^2 u}{\partial x_2^2} \right)^2. \tag{3.34}$$

where ε is the rate of turbulent dissipation and κ is the kinetic energy of turbulent flow.

4. Reynolds-Average Navier-Stoke (RANS) model. For the Reynolds stress $\tau_{ij} = -\rho\overline{\acute{u}_i \acute{u}_j}$, a transport equation is obtained. The Reynolds stresses are then utilised to close the Reynolds-averaged momentum equation [111]. The RANS transport equation is expressed as

$$\begin{aligned} \frac{\partial \rho \overline{\acute{u}_i \acute{u}_j}}{\partial t} + \frac{\partial \rho u_k \overline{\acute{u}_i \acute{u}_j}}{\partial x_k} = -\frac{\partial}{\partial x_k} \left[\overline{\rho \acute{u}_i \acute{u}_j \acute{u}_k} + \overline{p(\delta_{kj} \acute{u}_i + \delta_{ik} \acute{u}_i)} - \mu \frac{\partial}{\partial x_k} (\acute{u}_i \acute{u}_j) \right] \\ + P_{ij} + G_{ij} + \Phi_{ij} + \varepsilon_{ij}, \end{aligned} \tag{3.35}$$

where

$$P_{ij} = -\rho\left(\overline{\acute{u}_i\acute{u}_k}\frac{\partial u_j}{\partial x_k} + \overline{\acute{u}_j\acute{u}_k}\frac{\partial u_j}{\partial x_k}\right), \tag{3.36}$$

$$G_{ij} = -\rho\beta(g_j\overline{\acute{u}_j\theta} - g_j\overline{\acute{u}_j i\theta}), \tag{3.37}$$

$$\Phi_{ij} = \overline{P\left(\frac{\partial \acute{u}_i}{\partial x_j} + \frac{\partial \acute{u}_j}{\partial x_i}\right)}, \tag{3.38}$$

$$\varepsilon_{ij} = -2\mu\overline{\frac{\partial \acute{u}_i}{\partial x_k}\frac{\partial \acute{u}_j}{\partial x_k}}. \tag{3.39}$$

Finding the turbulent diffusion, the pressure-strain correlation, and the turbulent dissipation rate are the three main goals of this model.

The subgrid-scale (SGS) stress with an SGS eddy viscosity ν_e was further expressed as the following by adhering to the Boussinesq assumption for turbulent stress:

$$\tau_{ij} = -\nu_e\left(\frac{\partial \tilde{u}_i}{\partial x_j} + \frac{\partial \tilde{u}_j}{\partial x_i}\right). \tag{3.40}$$

The following momentum equation is produced by substituting Eq. 3.40 into Eq. 3.22:

$$\frac{\partial \tilde{u}_i}{\partial t} + \frac{\partial(\tilde{u}_i\tilde{u}_i)}{\partial x_j} = f_i - \frac{1}{\rho}\frac{\partial p}{\partial x_i} + \nu_t\frac{\partial^2 \tilde{u}_i}{\partial x_j \partial x_j}, \tag{3.41}$$

where $\nu_t = \nu + \nu_e$ is the total viscosity, ν is the kinematic viscosity, and ν_e is the eddy viscosity, expressed by

$$\nu_e = (C_s l_s)^2\sqrt{S_{ij}S_{ij}}, \tag{3.42}$$

where S_{ij} is the size of the large scale strain-rate tensor, l_s is the characteristic length scale, and C_s is the Smagorinsky constant [58].

$$S_{ij} = \frac{1}{2\rho}\left[\frac{\partial(\rho\tilde{u}_i)}{\partial x_j} + \frac{\partial(\rho\tilde{u}_j)}{\partial x_i}\right]. \tag{3.43}$$

Fewer unresolved scale eddies occur in the subgrid-scale (SGS) stress model with finer grid sizes. A direct numerical simulation of the SGS model is possible if the grid size is small enough. It is believed that including a subgrid-stress model into the lattice Boltzmann technique would result in a more accurate solution for turbulent flows given that the lattice spacing and mesh size are often significantly smaller than those utilised in a classical computing approach [112]. The following momentum equation is produced by substituting Eq. 3.23 into Eq. 3.22:

$$\frac{\partial \tilde{u}_i}{\partial t} + \frac{\partial (\tilde{u}_i \tilde{u}_i)}{\partial x_j} = f_i - \frac{1}{\rho}\frac{\partial p}{\partial x_i} + (\nu + \nu_e)\frac{\partial^2 \tilde{u}_i}{\partial x_j \partial x_j} - \acute{u}_i \acute{u}_j, \tag{3.44}$$

It can be seen from the equation above that a new term $\acute{u}_i \acute{u}_j$, called the Reynolds stress, appears.

In order to make things easier, the hats of u_i and u_j are dropped in the following equations, which are of an identical form to the generic turbulent axisymmetric flow equations. However, corresponding symbols indicate space-filtered variables. It is possible to express the governing equations for incompressible axisymmetric turbulent flow in a cylinder-coordinate system as follows:

$$\frac{\partial u_j}{\partial x_j} + \frac{u_r}{r} = 0, \tag{3.45}$$

$$\frac{\partial u_i}{\partial t} + u_j \frac{\partial u_i}{\partial x_j} = -\frac{1}{\rho}\frac{\partial p}{\partial x_j} + \nu_t \frac{\partial^2 u_i}{\partial^2 x_j} + \frac{\nu_t}{r}\frac{\partial u_i}{\partial r} - \frac{\nu_t u_i}{r^2}\delta_{ir}, \tag{3.46}$$

where ν_t is the total viscosity in a turbulent flow, $\nu_t = \nu + \nu_e$.

Chapter 4

Lattice Boltzmann Method

4.1 Introduction

The lattice Boltzmann method (LBM), a discrete computing technique, evolved from lattice gas cellular automata (LGCA), a fictional and simplified molecular model. In general, LBM comprises three parts: (1) the local equilibrium distribution function which determines which flow equations, such as the axisymmetric flow equations, are recovered by the lattice Boltzmann model; (2) the lattice Boltzmann equation which regulates the transport of the particle distribution function from one lattice to the nearby lattice; and (3) a lattice pattern that represents the grid nodes and controls the movement of the particles (Figs. 4.1,4.2 and 4.3).

4.2 Lattice Boltzmann Equation

The two basic phases that make up the LBM in lattice Boltzmann theory are streaming and collision. During the streaming step particles are controlled by the following factors as they migrate in the direction of their closest neighbours:

$$f_\alpha(\mathbf{X} + \mathbf{e}_\alpha \Delta t, t + \Delta t) - \acute{f}_\alpha(\mathbf{X}, t) = \frac{\Delta t}{\kappa e^2} e_{\alpha i} F_i, \tag{4.1}$$

where f_α is the distribution function of particles; $\acute{f_\alpha}$ represents the value prior to streaming; Δt is the time step; $\mathbf{X}$ is the space vector, i.e., $\mathbf{X} = (r, x); e = \Delta x/\Delta t; \Delta x$ is the lattice size; $e_{\alpha i}$ is the component of $\mathbf{e}_\alpha$, which is the velocity vector of a particle in the α link; F_i is the force term and κ is a constant determined from

$$\kappa = \frac{1}{e^2} \sum_\alpha e_{\alpha x} e_{\alpha x} = \frac{1}{e^2} \sum_\alpha e_{\alpha y} e_{\alpha y}. \tag{4.2}$$

The particles arrive at the collision step, interact with one another, with each modifying its velocity components and direction in accordance with the scattering law, given by:

$$\acute{f_\alpha}(\mathbf{X}, t) = f_\alpha(\mathbf{X}, t) + \Omega_\alpha[f(\mathbf{X}, t)], \tag{4.3}$$

where the collision operator "Ω_α" regulates the rate of change in f_α during a collision. The collision operator, which takes the form of a matrix, may be found in kinetic theory. Higuera and Jimenez [36] nonetheless provided a fundamentally essential notion of simplifying the collision operator in response to the complexity of the analytical solutions. The collision operator was linearized around its immediate equilibrium state. The equilibrium value of this collision operator is then enlarged. The operator is as follows, with reference to Noble et al. [113]:

$$\Omega_\alpha(f) = \Omega_\alpha(f^{eq}) + \frac{\partial \Omega_\alpha(f^{eq})}{\partial f_\beta}(f_\beta - f_\beta^{eq}) + \mathcal{O}\left[(f_\beta - f_\beta^{eq})^2\right], \tag{4.4}$$

where the f_α^{eq} is the local equilibrium distribution function and f_β is the distribution function.

A linearized collision operator (Eq. 4.5) is produced when high-order components in Eq. 4.4 are ignored such that $\Omega_\alpha(f^{eq}) = 0$:

$$\Omega_\alpha(f) \approx \frac{\partial \Omega_\alpha(f^{eq})}{\partial f_\beta}(f_\beta - f_\beta^{eq}). \tag{4.5}$$

The local particle distribution reaches equilibrium over a single relaxation time τ

[114, 115],

$$\frac{\partial \Omega_\alpha(f^{eq})}{\partial f_\beta} = -\frac{1}{\tau}\delta_{\alpha\beta}, \tag{4.6}$$

where $\delta_{\alpha\beta}$ is the Kronecker delta function defined as:

$$\delta_{\alpha\beta} = \begin{cases} 0, & \alpha \neq \beta, \\ 1, & \alpha = \beta. \end{cases} \tag{4.7}$$

Then, Eq. 4.5 can be expressed as:

$$\Omega_\alpha(f) = -\frac{1}{\tau}\delta_{\alpha\beta}(f_\beta - f_\beta^{eq}), \tag{4.8}$$

the lattice BGK collision operator [110] is produced using the aforementioned Eq. 4.8,

$$\Omega_\alpha(f) = -\frac{1}{\tau}(f_\alpha - f_\alpha^{eq}), \tag{4.9}$$

where τ stands for a single relaxation time. The most well-known lattice Boltzmann equation, or the so-called single relaxation time lattice Boltzmann equation, may be written as follows by changing the collision operator 4.9 into 4.3 [116]:

$$f_\alpha(\mathbf{X} + \mathbf{e}_\alpha \Delta t, t + \Delta t) - f_\alpha(\mathbf{X}, t) = -\frac{1}{\tau}(f_\alpha - f_\alpha^{eq}) + \frac{\Delta t}{\kappa e^2} e_{\alpha i} F_i(\mathbf{X}, t). \tag{4.10}$$

4.3 Connectivity to the Continuum Boltzmann Equation

The continuous Boltzmann equation (CBE) may also be used to generate the lattice Boltzmann equation (4.10), which historically developed from the LGCA. The BGK approximation appears in the CBE, which reads [115]:

$$\frac{\partial f}{\partial t} + e.\nabla f = -\frac{1}{\zeta}(f - f^{eq}), \tag{4.11}$$

where $f = (X, e, t)$ represents the single-particle distribution in continuum phase space (X, e); e is the velocity of the particle; ζ is the relaxation time; $\nabla = i\frac{\partial}{\partial x} + j\frac{\partial}{\partial y}$ is called gradient operator; and f^{eq} is the Maxwell-Boltzmann equilibrium distribution function, which is given by:

$$f^{eq} = \frac{\rho}{\sqrt{(2\pi/3)^D}} exp\Bigg[-\frac{3}{2}(e - V)^2 \Bigg], \tag{4.12}$$

Where the fluid velocity V and particle velocity e are normalised by $\sqrt{3RT}$ in which R is the ideal gas constant, T is temperature results in sound speed of $U_s = 1/\sqrt{3}$ [3] and D is the spatial dimension. Hence, the fluid's velocity and density are estimated using the distribution function.

$$\rho = \int f\, de, \tag{4.13}$$

$$\rho V = \int ef\, de. \tag{4.14}$$

The equilibrium distribution function provided by Eq. 4.12 may be extended in the following manner to second-order accuracy [117], provided the fluid velocity V is small in relation to the speed of sound,

$$f^{eq} = \frac{\rho}{\sqrt{(2\pi/3)^D}} exp\Bigg(-\frac{3}{2}e^2 \Bigg) \Bigg[1 + 3(eV) + \frac{9}{2}(eV)^2 - \frac{3}{2}V^2 \Bigg]. \tag{4.15}$$

A small collection of velocities and related distribution functions are constructed rather than the whole Boltzmann distribution in order to establish a discrete Boltzmann model.

$$f_\alpha = f(X, e_\alpha, t), \tag{4.16}$$

$$f_\alpha^{eq} = f^{eq}(X, e_\alpha, t), \tag{4.17}$$

They satisfy Eq. 4.11

$$\frac{\partial f_\alpha}{\partial t} + e.\nabla f_\alpha = -\frac{1}{\zeta}(f_\alpha - f_\alpha^{eq}) + S_\alpha, \tag{4.18}$$

where for the D2Q9 square lattice (Fig. 4.1),

$$S_\alpha = \frac{1}{6e^2} e_{\alpha i} F_i, \tag{4.19}$$

Eq. 4.18 is discretized by

$$\begin{aligned} \frac{f_\alpha(\mathbf{X}, t+\Delta t) - f_\alpha(\mathbf{X}, t)}{\Delta t} &+ e_{\alpha x}\frac{f_\alpha(\mathbf{X}+\Delta x, t+\Delta t) - f_\alpha(\mathbf{X}, t+\Delta t)}{\Delta x} \\ &= -\frac{1}{\zeta}(f_\alpha - f_\alpha^{eq}) + S_\alpha, \end{aligned} \tag{4.20}$$

or

$$\begin{aligned} f_\alpha(\mathbf{X}, t+\Delta t) - f_\alpha(\mathbf{X}, t) &+ e_{\alpha x}\frac{\Delta t}{\Delta x}[f_\alpha(\mathbf{X}+\Delta x, t+\Delta t) - f_\alpha(\mathbf{X}, t+\Delta t)] \\ &= -\frac{1}{\zeta/\Delta t}(f_\alpha - f_\alpha^{eq}) + S_\alpha \Delta t. \end{aligned} \tag{4.21}$$

Lagrangian behaviour is then produced by selecting $\Delta x/\Delta t = e_{\alpha x}$ and cancelling the $f_\alpha(\mathbf{X}, t+\Delta t)$ terms, resulting in

$$f_\alpha(\mathbf{X}, t+\Delta t) - f_\alpha(\mathbf{X}, t) = -\frac{1}{\tau}(f_\alpha - f_\alpha^{eq}) + S_\alpha \Delta t, \tag{4.22}$$

where $\tau = \dfrac{\zeta}{\Delta t}$ and should be referred to as a single dimensionless relaxation time.

4.4 Lattice Pattern

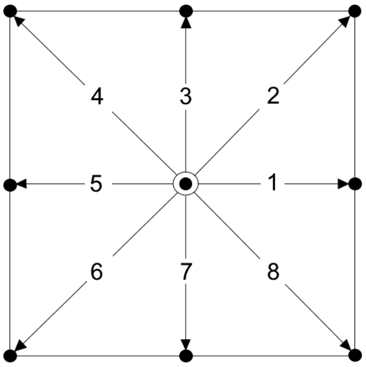

Figure 4.1: Nine-velocity square lattice(D2Q9).

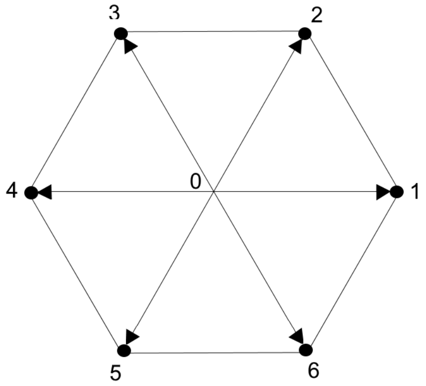

Figure 4.2: Seven-velocity hexagonal lattice(D2Q7).

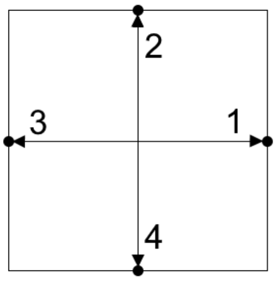

Figure 4.3: Four-velocity lattice(D2Q4).

The grid points are built up in a conventional manner using a lattice design. In the lattice Boltzmann technique, the grid is used for calculating particle movements and serving as a microscopic model for molecular dynamics. The lattice pattern controls the constant κ in the lattice Boltzmann equation Eq. 4.10. There are many regular lattice patterns to choose from in two dimensions, and the LBM may be expressed in a straightforward, explicit form for each of them [117]. Square and hexagonal lattices are the most popular of these lattice forms. According to Qian's notation [118], two-dimensional four or nine-velocity lattices are referred to in this thesis as D2Q4 and D2Q9, respectively.

Not all of these lattice arrangements, nevertheless, have sufficient symmetry, which is vital for recovering the proper flow equations [33]. Both the D2Q9 and D2Q7 lattices exhibit this feature, as shown by theoretical analysis and numerical experiments [119], and perform satisfactorily in these simulations. Fietz [120] reported that models built on the D2Q9 lattice typically yield more accurate findings than those built on the D2Q7 lattice. Additionally, the square lattice provides a simple method for implementing various boundary conditions [121], correlates the force term with a gradient, and computes the boundary conditions quickly and precisely. The D2Q9 lattice is therefore selected there.

Each particle in the nine-speed square lattice (D2Q9) shown in Fig. 4.1 travels one lattice unit along the eight connections denoted by the numbers 1 through 8, or remains at rest with zero speed at connection 0. Particle velocities are determined by:

$$\mathbf{e}_\alpha = \begin{cases} (0,0), & \alpha = 0 \\ \lambda_\alpha e[\cos\frac{(\alpha-1)\pi}{4}, \sin\frac{(\alpha-1)\pi}{4}], & \alpha \neq 0 \end{cases} \tag{4.23}$$

The 9-speed square lattice is shown to have the following fundamental characteristics.

$$\sum_\alpha e_{\alpha i} = \sum_\alpha e_{\alpha i} e_{\alpha j} e_{\alpha k} = 0, \tag{4.24}$$

$$\sum_{\alpha} e_{\alpha i} e_{\alpha j} = 6e^2 \delta_{ij}, \tag{4.25}$$

$$\sum_{\alpha} e_{\alpha i} = \sum_{\alpha} e_{\alpha i} e_{\alpha j} e_{\alpha k} e_{\alpha l} = 4e^4 (\sigma_{ij}\sigma_{kl} + \sigma_{ik}\sigma_{jl} + \sigma_{il}\sigma_{jk}) - 6e^4 \Delta_{ijkl}, \tag{4.26}$$

where

$$\Delta_{ijkl} = \begin{cases} 1, & i = j = k = l, \\ 0, & otherwise. \end{cases} \tag{4.27}$$

Substituting Eq. 4.23 into Eq. 4.2, we obtain

$$\kappa = \frac{1}{e^2} \sum_{\alpha} e_{\alpha x} e_{\alpha x} = \frac{1}{e^2} \sum_{\alpha} e_{\alpha y} e_{\alpha y} = 6. \tag{4.28}$$

The most typical version of a lattice Boltzmann model with a D2Q9 lattice may be derived by combining Eq. 4.28 and Eq. 4.10,

$$f_\alpha(\mathbf{X} + \mathbf{e}_\alpha \Delta t, t + \Delta t) - f_\alpha(\mathbf{X}, t) = -\frac{1}{\tau}(f_\alpha - f_\alpha^{eq}) + \frac{\Delta t}{6e^2} e_{\alpha i} F_i(\mathbf{X}, t). \tag{4.29}$$

4.5 Local Equilibrium Distribution Function

The lattice Boltzmann technique relies heavily on the local equilibrium distribution function, which determines the flow equations to be solved by the lattice Boltzmann model. If the two-dimensional axisymmetric flow equations 3.14 and 3.15 are solved using the lattice Boltzmann equation Eq. 4.29, then an appropriate local equilibrium distribution functionf_α^{eq} must be obtained. The Fermi-Dirac distribution, which is frequently extended as a Taylor series in macroscopic velocity to its second-order [33], is considered an equilibrium function in lattice gas cellular automata (LGCA) theory. The equilibrium distribution function for retrieving the Navier-Stokes equations using the lattice Boltzmann technique may be obtained [84] by applying a Taylor expansion to the Maxwell-Boltzmann distribution. These techniques, however, cannot be used to create axisymmetric flow equations. Thus, the correct formula for the local equilibrium distribution function is found using an alternate and effective technique known as the Ansatz approach [122]. An equilibrium function in the Ansatz technique may be thought of as a power series in macroscopic velocity [123].

$$f_\alpha^{eq} = A_\alpha + B_\alpha e_{\alpha i} u_i + C_\alpha e_{\alpha i} e_{\alpha j} u_i u_j + D_\alpha u_i u_j, \tag{4.30}$$

Due to this underlying premise, the procedure may be effectively applied to a variety of flow problems. Numerous studies have validated and illustrated the accuracy and adaptability of the technique [124, 125, 126]. The equilibrium function and the lattice have the same symmetry, and so

$$A_1 = A_3 = A_5 = A_7 = \dot{A}, \tag{4.31}$$

$$A_2 = A_4 = A_6 = A_8 = \ddot{A}, \tag{4.32}$$

with similar expressions for B_α, C_α and D_α. Eq. 4.30 is conveniently stated as

$$f_\alpha^{eq} = \begin{cases} A_0 + D_0 u_i u_i, & \alpha = 0, \\ \dot{A} + \dot{B} e_{\alpha i} u_i + \dot{C} e_{\alpha i} e_{\alpha j} u_i u_j + \dot{D} u_i u_j,, & \alpha = 1,3,5,7, \\ \ddot{A} + \ddot{B} e_{\alpha i} u_i + \ddot{C} e_{\alpha i} e_{\alpha j} u_i u_j + \ddot{D} u_i, & \alpha = 2,4,6,8. \end{cases} \tag{4.33}$$

The conservation relations, such as mass and momentum conservation, are employed as constraints on the equilibrium distribution function to calculate the coefficients in the equations above. The local equilibrium distribution function (Eq. 4.33) for the axisymmetric flow equations must meet the following three requirements:

$$\sum_\alpha f_\alpha^{eq} = \rho, \tag{4.34}$$

$$\sum_\alpha e_{\alpha i} f_\alpha^{eq} = \rho u_i, \tag{4.35}$$

$$\sum_\alpha e_{\alpha i} e_{\alpha j} f_\alpha^{eq} = P\delta_{ij} + \rho u_i u_j. \tag{4.36}$$

Computation of the lattice Boltzmann equation (4.29) based on the aforementioned restrictions then facilitates the solution of the two-dimensional axisymmetric flow equations (3.14) and (3.15). The friction force and wind shear stress, which are examples of source terms in the axisymmetric flow equations, are not taken into account in this process because they will be cancelled out. Substituting Eq. 4.33 into Eq. 4.34;

$$\begin{aligned} &A_0 - D_0 u_i u_i \\ &\quad + 4\dot{A} + \sum_{\alpha=1,3,5,7} \dot{B} e_{\alpha i} u_i + \sum_{\alpha=1,3,5,7} \dot{C} e_{\alpha i} e_{\alpha j} u_i u_j - 4\dot{D} u_i u_i \\ &\quad + 4\ddot{A} + \sum_{\alpha=1,3,5,7} \ddot{B} e_{\alpha i} u_i + \sum_{\alpha=2,4,6,8} \ddot{C} e_{\alpha i} e_{\alpha j} u_i u_j - 4\ddot{D} u_i u_i \\ &\quad = \rho. \end{aligned} \tag{4.37}$$

Eq. 4.23, which evaluates the coefficients of ρ and $u_i u_i$, is then substituted into the Eq. 4.37, giving

$$A_0 + 4\dot{A} + 4A = \rho \tag{4.38}$$

$$D_0 + 2e^2\dot{C} + 4e^2\ddot{C} + 4\dot{D} + 4\ddot{D} = 0. \tag{4.39}$$

Likewise, applying Eq. 4.33 to Eq. 4.35 results in

$$\begin{aligned} &A_0 e_{\alpha i} - D_0 e_{\alpha i} u_j u_j \\ &\quad + \sum_{\alpha=1,3,5,7} \left(\dot{A} e_{\alpha i} + \dot{B} e_{\alpha i} e_{\alpha j} u_i + \dot{C} e_{\alpha i} e_{\alpha j} e_{\alpha k} u_i u_j - \dot{D} e_{\alpha i} e_{\alpha j} u_i u_i \right) \\ &\quad + \sum_{\alpha=2,4,6,8} \left(\ddot{A} e_{\alpha i} + \ddot{B} e_{\alpha i} e_{\alpha j} u_i + \ddot{C} e_{\alpha i} e_{\alpha j} e_{\alpha k} u_i u_j - \ddot{D} e_{\alpha i} e_{\alpha j} u_i u_i \right) = \rho u_i. \end{aligned} \tag{4.40}$$

Assuming the coefficients of u_i to be equal, leads to

$$2e^2\dot{B} + 4e^2\ddot{B} = \rho. \tag{4.41}$$

Adding Eq. 4.33 once more to the third restriction, Eq. 4.35 produces

$$\begin{aligned}&\sum_{\alpha=1,3,5,7}\left(\dot{A}e_{\alpha i}e_{\alpha j}+\dot{B}e_{\alpha i}e_{\alpha j}e_{\alpha k}u_j u_k+\dot{C}e_{\alpha i}e_{\alpha j}e_{\alpha k}e_{\alpha l}u_k u_l-\dot{D}e_{\alpha i}e_{\alpha j}u_k u_k\right)\\&+\sum_{\alpha=2,4,6,8}\left(\ddot{A}e_{\alpha i}e_{\alpha j}+\ddot{B}e_{\alpha i}e_{\alpha j}e_{\alpha k}u_j u_k+\ddot{C}e_{\alpha i}e_{\alpha j}e_{\alpha k}e_{\alpha l}u_k u_l-\ddot{D}e_{\alpha i}e_{\alpha j}u_k u_k\right)\\&=P\delta_{ij}+\rho u_i u_j.\end{aligned}\tag{4.42}$$

Inserting Eq. 4.23 into the preceding equation yields

$$\begin{aligned}&2\dot{A}e^2\delta_{ij}+2\dot{C}e^4u_iu_i+2\dot{D}e^2u_iu_i+4\ddot{A}e^2\delta_{ij}\\&+8\ddot{C}e^2u_iu_j+4\ddot{C}e^4u_iu_i+4\ddot{C}e^2u_iu_i=P\delta_{ij}+\rho u_iu_i.\end{aligned}\tag{4.43}$$

Hence, four more relationships may be derived,

$$2e^2\dot{A}+4e^2\ddot{A}=p,\tag{4.44}$$

$$8e^2\ddot{C}=\rho,\tag{4.45}$$

$$2e^2\dot{C}=\rho,\tag{4.46}$$

$$2e^2\dot{D}+4e^2\ddot{D}+4e^4\ddot{C}=0.\tag{4.47}$$

Eqs. 4.45 and 4.46 may be combined to obtain

$$4\ddot{C}=\dot{C}.\tag{4.48}$$

Because of symmetry, three extra relations may be assumed with regard to Eq 4.48.

$$4\ddot{A}=\dot{A},\tag{4.49}$$

$$4\ddot{B}=\dot{B},\tag{4.50}$$

$$4\ddot{D}=\dot{D}.\tag{4.51}$$

Therefore, Eqs. (4.38), (4.39), (4.41) and (4.44)-(4.51) are available to determine the coefficients as follow:

$$A_0 = \frac{4}{9}\rho, \qquad B_0 = -\frac{2\rho}{3e^2} \tag{4.52}$$

$$\dot{A} = \frac{\rho}{9}, \qquad \dot{B} = \frac{\rho}{3e^2}, \qquad \dot{C} = \frac{\rho}{2e^4}, \qquad \dot{D} = -\frac{\rho}{6e^4}, \tag{4.53}$$

$$\ddot{A} = \frac{\rho}{36}, \qquad \ddot{B} = \frac{\rho}{12e^2}, \qquad \ddot{C} = \frac{\rho}{8e^2}, \qquad \ddot{D} = -\frac{\rho}{24e^2}. \tag{4.54}$$

As a result, the local equilibrium distribution function is obtained by substituting Eqs. 4.52, 4.53, and 4.54 into Eq. 4.33:

$$f_\alpha^{eq} = \omega_\alpha \rho (1 + 3\frac{e_{\alpha i} u_i}{e^2} + \frac{9}{2}\frac{e_{\alpha i} e_{\alpha j} u_i u_j}{e^4} - \frac{3}{2}\frac{u_i u_i}{e^2}), \tag{4.55}$$

where

$$\omega_\alpha = \begin{cases} \frac{4}{9}, & \alpha = 0, \\ \frac{1}{9}, & \alpha = 1, 3, 5, 7, \\ \frac{1}{36}, & \alpha = 2, 4, 6, 8; \end{cases} \tag{4.56}$$

The lattice Boltzmann equation is then utilised to solve the axisymmetric flow equations using this local equilibrium distribution function.

4.6 Lattice Boltzmann Equation for Axisymmetric Flow

4.6.1 Axisymmetric Flow without Swirl

On the nine-speed square lattice depicted in Fig. 4.1, the AxLAB® discretisation reads

$$f_\alpha(\mathbf{X} + \mathbf{e}_\alpha \Delta t, t + \Delta t) - f_\alpha(\mathbf{X}, t) = -\tau_\alpha (f\alpha - f_\alpha^{eq}) + \omega_\alpha \theta \Delta t + \frac{\Delta t}{\kappa e^2} e_{\alpha i} F_i \tag{4.57}$$

where f_α is the distribution function of particles; f_α^{eq} is the local equilibrium distribution function; Δt is the time step; $\mathbf{X}$ is the space vector, i.e., $\mathbf{X} = (r, x); e = \Delta x/\Delta t; \Delta x$ is the lattice size; ω_α is the weight given by Eq. 4.56 When using the nine-speed lattice pattern; θ is the source or sink term,

$$\theta = -\frac{\rho u_r}{r}, \tag{4.58}$$

F_i is the force term defined by

$$F_i = -\frac{\rho u_i u_r}{r} - \frac{2\rho\nu u_i}{r^2}\delta_{ir}. \tag{4.59}$$

where δ_{ij} denotes the Kronecker function in Eq. 4.59; $e_{\alpha i}$ is the component of $\mathbf{e}_\alpha$, which is the velocity vector of a particle in the α link defined by

$$\mathbf{e}_\alpha = \begin{cases} (0,0), & \alpha = 0 \\ \lambda_\alpha e[\cos\frac{(\alpha-1)\pi}{4}, \sin\frac{(\alpha-1)\pi}{4}], & \alpha \neq 0 \end{cases} \tag{4.60}$$

where λ_α is

$$\lambda_\alpha = \begin{cases} 1, & \alpha = 1,3,5,7, \\ \sqrt{2}, & \alpha = 2,4,6,8. \end{cases} \tag{4.61}$$

The constant κ is determined from

$$\kappa = \frac{1}{e^2}\sum_\alpha e_{\alpha x}e_{\alpha x} = \frac{1}{e^2}\sum_\alpha e_{\alpha r}e_{\alpha r}. \tag{4.62}$$

With Eq. 4.62 we have $\kappa = 6$. τ_α is the relaxation time and is expressed as

$$\tau_\alpha = \begin{cases} \frac{1}{\tau}, & r = 0 \\ \frac{1}{\tau}\left[1 + \frac{(2\tau - 1)e_{\alpha r}\Delta t}{2r}\right], & r \neq 0. \end{cases} \tag{4.63}$$

The fluid kinematic viscosity ν and constant relaxation time τ are related as follows:

$$\nu = \frac{e^2\Delta t}{6}(2\tau - 1). \tag{4.64}$$

The fluid density ρ and velocity u_i, are determined as

$$\rho = \sum_{\alpha} f_\alpha, \qquad u_i = \frac{1}{\rho}\sum_{\alpha} e_{\alpha i} f_\alpha. \tag{4.65}$$

4.6.2 Recovery of the Axisymmetric Flow Equations without Swirl

The Chapman-Enskog analysis is used to demonstrate how the lattice Boltzmann equation can be used to derive the macroscopic equations (3.14) and (3.17) from Eq. 4.57. The presumption is that t is small and equal to ε,

$$\Delta t = \varepsilon. \tag{4.66}$$

Inputting the aforementioned equation into Eq. 4.57 results in

$$\begin{aligned} &f_\alpha(\mathbf{X} + \mathbf{e}_\alpha \varepsilon, t + \varepsilon) - f_\alpha(\mathbf{X}, t) \\ &\qquad = -\frac{1}{\tau}(f\alpha - f_\alpha^{eq}) - \frac{(2\tau - 1)}{2\tau r} e_{\alpha r}\varepsilon(f\alpha - f_\alpha^{eq}) + \omega_\alpha \theta \varepsilon + \frac{\varepsilon}{6e^2} e_{\alpha i} F_i. \end{aligned} \tag{4.67}$$

By applying a Taylor expansion at the point$(\mathbf{X}, t)$ of Eq. 4.67 in time and space,

$$\begin{aligned} &\varepsilon\left(\frac{\partial}{\partial t} + e_{\alpha j}\frac{\partial}{\partial x_j}\right) f_\alpha + \frac{1}{2}\varepsilon^2\left(\frac{\partial}{\partial t} + e_{\alpha j}\frac{\partial}{\partial x_j}\right)^2 f_\alpha + O(\varepsilon^3) \\ &= -\frac{1}{\tau}(f_\alpha - f_\alpha^{eq}) - \frac{(2\tau - 1)}{2\tau r} e_{\alpha r}\varepsilon(f_\alpha - f_\alpha^{eq}) + \omega_\alpha \theta \varepsilon + \frac{\varepsilon}{6e^2} e_{\alpha i} F_i. \end{aligned} \tag{4.68}$$

The Chapman-Enskog extension states that f_α may be expressed as a series of ε,

$$f_\alpha = f_\alpha^{(0)} + \varepsilon f_\alpha^{(1)} + \varepsilon^2 f_\alpha^{(2)} + O(\varepsilon^3). \tag{4.69}$$

Both the source term θ and the force term F_i are calculated using the centred scheme [127] as

$$\theta = \theta\left(\mathbf{X} + \frac{1}{2}\mathbf{e}_\alpha\varepsilon, t + \frac{1}{2}\varepsilon\right) \tag{4.70}$$

and

$$F_i = F_i\left(\mathbf{X} + \frac{1}{2}\mathbf{e}_\alpha\varepsilon, t + \frac{1}{2}\varepsilon\right) \tag{4.71}$$

which, after Taylor expansion, may be expressed as

$$\theta\left(\mathbf{X} + \frac{1}{2}\mathbf{e}_\alpha\varepsilon, t + \frac{1}{2}\varepsilon\right) = \theta(\mathbf{X}, t) + \frac{1}{2}\varepsilon\left(\frac{\partial}{\partial t} + e_{\alpha j}\frac{\partial}{\partial x_j}\right)\theta(\mathbf{X}, t) + O(\varepsilon^2) \tag{4.72}$$

and

$$F_i\left(\mathbf{X} + \frac{1}{2}\mathbf{e}_\alpha\varepsilon, t + \frac{1}{2}\varepsilon\right) = F_i(\mathbf{X}, t) + \frac{1}{2}\varepsilon\left(\frac{\partial}{\partial t} + e_{\alpha j}\frac{\partial}{\partial x_j}\right)F_i(\mathbf{X}, t) + O(\varepsilon^2). \tag{4.73}$$

Eq. 4.68 is changed by substituting Eq. 4.69, 4.72, and 4.73. An equation to the order of ε^0 is thus obtained. Here, the expansion

$$f_\alpha^{(0)} = f_\alpha^{eq}, \tag{4.74}$$

to the order of ε is

$$\left(\frac{\partial}{\partial t} + e_{\alpha j}\frac{\partial}{\partial x_j}\right)f_\alpha^{(0)} = -\frac{f_\alpha^{(1)}}{\tau} + \omega_\alpha\theta + \frac{1}{6e^2}e_{\alpha i}F_i, \tag{4.75}$$

and the order of ε^2 is

$$\begin{aligned}\left(\frac{\partial}{\partial t} + e_{\alpha j}\frac{\partial}{\partial x_j}\right)f_\alpha^{(1)} + \frac{1}{2}\left(\frac{\partial}{\partial t} + e_{\alpha j}\frac{\partial}{\partial x_j}\right)^2 f_\alpha^{(0)} = -\frac{f_\alpha^{(2)}}{\tau} - \frac{(2\tau - 1)}{2\tau r}e_{\alpha r}f_\alpha^{(1)} \\ + \frac{1}{2}\left(\frac{\partial}{\partial t} + e_{\alpha j}\frac{\partial}{\partial x_j}\right)(\omega_\alpha\theta) + \frac{1}{12e^2}\left(\frac{\partial}{\partial t} + e_{\alpha j}\frac{\partial}{\partial x_j}\right)(e_{\alpha i}F_i).\end{aligned} \tag{4.76}$$

Using Eq. 4.75, Eq. 4.76 may be expressed:

$$\frac{(2\tau-1)}{2\tau}\left(\frac{\partial}{\partial t}+e_{\alpha j}\frac{\partial}{\partial x_j}\right)f_\alpha^{(1)}=-\frac{f_\alpha^{(2)}}{\tau}-\frac{(2\tau-1)}{2\tau}e_{\alpha r}f_\alpha^{(1)}. \tag{4.77}$$

by applying Eq. (4.75)+$\varepsilon\times$Eq. (4.77),

$$\begin{gathered}\left(\frac{\partial}{\partial t}+e_{\alpha j}\frac{\partial}{\partial x_j}\right)f_\alpha^{(0)}+\frac{(2\tau-1)\varepsilon}{2\tau}\left(\frac{\partial}{\partial t}+e_{\alpha j}\frac{\partial}{\partial x_j}\right)f_\alpha^{(1)}\\ =\frac{1}{\tau}(f_\alpha^{(1)}-\varepsilon f_\alpha^{(2)})-\frac{(2\tau-1)\varepsilon}{2\tau}e_{\alpha r}f_\alpha^{(1)}+\omega_\alpha\theta+\frac{1}{6e^2}e_{\alpha i}F_i.\end{gathered} \tag{4.78}$$

The sum of the above equations over α yields

$$\frac{\partial}{\partial t}\sum_\alpha f_\alpha^{(0)}+\frac{\partial}{\partial x_j}\sum_\alpha e_{\alpha j}f_\alpha^{(0)}=\theta. \tag{4.79}$$

If the variation in density is small enough to be overlooked, then taking $\sum(Eq.(4.75)+\varepsilon\times Eq.4.77)$ results in

$$\frac{\partial}{\partial t}\sum_\alpha e_{\alpha i}f_\alpha^{(0)}+\frac{\partial\Pi_{ij}^{(0)}}{\partial x_j}=\frac{\partial\Lambda_{ij}}{\partial x_j}+\frac{\Lambda_{ij}}{r}+F_i, \tag{4.80}$$

where the following formulae represent the zero-order momentum flux tensor:

$$\Pi_{ij}^{(0)}=\sum_\alpha e_{\alpha i}e_{\alpha j}f_\alpha^{(0)}, \tag{4.81}$$

$$\Lambda_{ij}=-\frac{\varepsilon}{2\tau}(2\tau-1)\sum_\alpha e_{\alpha i}e_{\alpha j}f_\alpha^{(1)}, \tag{4.82}$$

$$\Lambda_{ij}=-\frac{\varepsilon}{2\tau}(2\tau-1)\sum_\alpha e_{\alpha i}e_{\alpha r}f_\alpha^{(1)}, \tag{4.83}$$

Reviewing the terms in Eq. 4.81 using Eq. 4.55,

$$\Pi_{ij}^{(0)}=P\delta_{ij}+\rho u_i u_j, \tag{4.84}$$

where $P = \rho e^2/3$ is the pressure, resulting in a speed of sound $C_s = e/\sqrt{3}$. Substituting Eq. 4.84 into Eq. 4.80, the result is

$$\frac{\partial(\rho u_i)}{\partial t} + \frac{\partial(\rho u_i u_j)}{\partial x_j} = -\frac{\partial P}{\partial x_i} + \frac{\partial \Lambda_{ij}}{j} + \frac{\Lambda_{ir}}{r} + F_i. \tag{4.85}$$

Eq. 4.82 may be rewritten using Eq. 4.75 as:

$$\Lambda_{ij} = \Pi_{ij}^{(1)} - \frac{\varepsilon}{2}(2\tau - 1)\sum_{\alpha} e_{\alpha i} e_{\alpha r} \omega_\alpha \theta, \tag{4.86}$$

where the first-order momentum flux tensor $\Pi_{ij}^{(1)}$, is given by

$$\Pi_{ij}^{(1)} = \frac{\varepsilon}{2}(2\tau - 1)\sum_{\alpha} e_{\alpha i} e_{\alpha r}\left(\frac{\partial}{\partial t} + e_{\alpha k}\frac{\partial}{\partial x_k}\right) f_\alpha^{(0)}, \tag{4.87}$$

Using Eq. 4.81, we obtain:

$$\Pi_{ij}^{(1)} = \frac{\varepsilon}{2}(2\tau - 1)\frac{\partial}{\partial t}\Pi_{ij}^{(0)} + \frac{\varepsilon}{2}(2\tau - 1)\frac{\partial}{\partial x_k}\sum_{\alpha} e_{\alpha i} e_{\alpha r} e_{\alpha k} f_\alpha^{(0)}, \tag{4.88}$$

combining Eqs. 4.55, 4.74 and 4.81 leads to

$$\frac{\partial}{\partial x_k}\sum_{\alpha} e_{\alpha i} e_{\alpha r} e_{\alpha k} f_\alpha^{(0)} = \frac{e^2}{3}\frac{\partial}{\partial x_k}(\rho u_i \delta_{jk} + \rho u_j \delta_{ki} + \rho u_k \delta_{ij}). \tag{4.89}$$

For characteristic velocity U_c, characteristic length L_c and characteristic time t_c, the term $\frac{\partial}{\partial t}\Pi_{ij}^{(0)}$ is of the order of $\rho U_c^2/t_c$, and the term $\frac{\partial}{\partial x_k}\sum_\alpha e_{\alpha i} e_{\alpha r} e_{\alpha k} f_\alpha^{(0)}$ is of the order of $\rho e^2 U_c^2/L_c$. Using this information, we determine that the ratio of the former to the latter terms is of the order

$$\begin{aligned}\mathbf{O}\left(\frac{\frac{\partial}{\partial t}\Pi_{ij}^{(0)}}{\frac{\partial}{\partial x_k}\sum_\alpha e_{\alpha i} e_{\alpha r} e_{\alpha k} f_\alpha^{(0)}}\right) =& \mathbf{O}\left(\frac{\rho U_c^2/t_c}{\rho e^2 U_c^2/L_c}\right) = \\ & \mathbf{O}\left(\frac{U_c}{e}\right)^2 = \mathbf{O}\left(\frac{U_c}{C_s}\right)^2 = \mathbf{O}\left(M^2\right)\end{aligned} \tag{4.90}$$

in which $M = U_c/C_s$ is the Mach number. The first term in Eq. 4.88 is negligible in comparison to the second term if $M << 1$. This is in accordance with lattice Boltzmann dynamics. As a result, when Eq. 4.89 is substituted into Eq. 4.88 we obtain;

$$\Pi_{ij}^{(1)} = \frac{e^2\varepsilon}{6}(2\tau - 1)\frac{\partial}{\partial x_k}(\rho u_i\delta_{jk} + \rho u_j\delta_{ki} + \rho u_k\delta_{ij}), \tag{4.91}$$

or

$$\Pi_{ij}^{(1)} = \nu\left[\frac{\partial(\rho u_i)}{\partial x_j} + \frac{\partial(\rho u_j)}{\partial x_i} + \frac{\partial(\rho u_k)}{\partial x_k}\delta_{ij}\right], \tag{4.92}$$

in which ν is the kinematic viscosity, expresses by Eq. 4.64.

Eq. 4.92 is inserted into Eq. 4.86 and the remaining terms are evaluated, resulting in

$$\Lambda_{ij} = \nu\left[\frac{\partial(\rho u_i)}{\partial x_j} + \frac{\partial(\rho u_j)}{\partial x_i} + \frac{\partial(\rho u_k)}{\partial x_k}\delta_{ij}\right] - \nu\theta\delta_{ij}. \tag{4.93}$$

After solving the aforementioned problem using $\theta = -u_r/r$ and imposing continuity Eq. 3.14, gives

$$\Lambda_{ij} = \nu\left[\frac{\partial(\rho u_i)}{\partial x_j} + \frac{\partial(\rho u_j)}{\partial x_i}\right], \tag{4.94}$$

and

$$\Lambda_{ir} = \nu\left[\frac{\partial(\rho u_i)}{\partial x_r} + \frac{\partial(\rho u_r)}{\partial x_i}\right]. \tag{4.95}$$

Eq. 4.59, Eq. 4.94, and Eq. 4.95 combined with Eq. 4.85, yield

$$\begin{aligned}\frac{\partial(\rho u_i)}{\partial t} + \frac{\partial(\rho u_i u_j)}{\partial x_j} =& -\frac{\partial P}{\partial x_i} + \nu\frac{\partial}{\partial x_j}\left[\frac{\partial(\rho u_i)}{\partial x_j} + \frac{\partial(\rho u_j)}{\partial x_i}\right] \\ &+ \frac{\nu}{r}\left[\frac{\partial(\rho u_i)}{\partial x_r} + \frac{\partial(\rho u_r)}{\partial x_i}\right] - \frac{\rho u_i u_r}{r} - \frac{2\rho\nu u_i}{r^2}\delta_{ij}.\end{aligned} \tag{4.96}$$

Eq. 4.94 is essentially the momentum equation assuming sufficient small density variation.

4.6.3 Axisymmetric Flow with Swirl

The governing equation for the azimuthal velocity component in a cylindrical coordinate system subject to axisymmetric rotating flow is [15]:

$$\frac{\partial u_\phi}{\partial t} + \frac{\partial (u_j u_\phi)}{\partial x_j} = \nu \frac{\partial^2 u_\phi}{\partial x_j^2} + \frac{\nu}{r}\frac{\partial u_\phi}{\partial r} - \frac{2u_r u_\phi}{r} - \frac{\nu u_\phi}{r^2}. \tag{4.97}$$

By adding another term to the force term F in Eq. 4.59, the extra impact of solid on the flow field is taken into consideration,

$$F_i = -\frac{\rho u_i u_r}{r} - \frac{2\rho\upsilon u_i}{r^2}\delta_{ir} + \frac{\rho u_\phi^2}{r}\delta_{ir}. \tag{4.98}$$

In practice, a D2Q4 or D2Q5 lattice Boltzmann model may be used to precisely and quickly solve the advection-diffusion Eq. 4.59 [128, 129, 130]. The rotating lattice Boltzmann equation is solved as follows using D2Q4 lattice:

$$\bar{f}_\alpha(\mathbf{X} + \bar{\mathbf{e}}_\alpha \Delta t, t + \Delta t) - \bar{f}_\alpha(\mathbf{X}, t) = -\bar{\tau}_\alpha(\bar{f}\alpha - \bar{f}_\alpha^{eq}) + \frac{S_\phi \Delta t}{4}, \tag{4.99}$$

where $\bar{f}_\alpha$ is the distribution function; $\bar{f}_\alpha^{eq}$; is the local equilibrium distribution function; S_ϕ is the source or sink term given by

$$S_\phi = -\frac{2\rho u_r u_\phi}{r} - \frac{\rho\nu u_\phi}{r^2}; \tag{4.100}$$

$\bar{f}_\alpha^{eq}$ is defined by [131]

$$\bar{f}_\alpha^{eq} = \left(1 + \frac{2\bar{e}_{\alpha j} u_j}{e^2}\right)\frac{\rho u_\phi}{4}, \qquad \alpha = 1, 2, 3, 4, \tag{4.101}$$

in which $\bar{e}_{\alpha j}$ is the component of $\bar{\mathbf{e}}_\alpha$ which is the velocity vector of a particle on the D2Q4,

$$\bar{e}_{\alpha j} = e\left[\cos\frac{(\alpha-1)\pi}{4}, \sin\frac{(\alpha-1)\pi}{4}\right], \qquad \alpha = 1, 2, 3, 4; \tag{4.102}$$

and $\bar{\tau}_\alpha$ is an effective relaxation time linked with the single relaxation time $\bar{\tau}$;

$$\bar{\tau}_\alpha = \begin{cases} \frac{1}{\bar{\tau}}, & r = 0 \\ \frac{1}{\bar{\tau}}\left[1 + \frac{(2\bar{\tau}-1)\bar{e}_{\alpha r}\Delta t}{2r}\right], & r \neq 0. \end{cases} \tag{4.103}$$

The azimuthal velocity u_ϕ is calculated as

$$u_\phi = \frac{1}{\rho}\sum_\alpha \bar{f}_\alpha. \tag{4.104}$$

It can be shown that the Eq.4.101 has the following properties:

$$\sum_\alpha \bar{f}_\alpha^{eq} = \rho u_\phi, \tag{4.105}$$

$$\sum_\alpha \bar{e}_{\alpha i}\bar{f}_\alpha^{eq} = \rho u_i u_\phi, \tag{4.106}$$

and

$$\sum_\alpha \bar{e}_{\alpha i}\bar{e}_{\alpha j}\bar{f}_\alpha^{eq} = \rho e^2 u_\phi \delta_{ij}/2. \tag{4.107}$$

4.6.4 Recovery of Axisymmetric Lattice Boltzmann Equation with Swirl

Using a similar Chapman-Enskog analysis to that provided in Sec. 4.6.2 and a Taylor expansion of the lattice Boltzmann equation (4.99) in time and space at point x. Eq.

4.97 may be reconstructed from Eq. 4.99. We have,

$$\begin{aligned}&\varepsilon\left(\frac{\partial}{\partial t}+\bar{e}_{\alpha j}\frac{\partial}{\partial x_j}\right)\bar{f}_\alpha+\frac{1}{2}\varepsilon^2\left(\frac{\partial}{\partial t}+\bar{e}_{\alpha j}\frac{\partial}{\partial x_j}\right)^2\bar{e}_\alpha+\mathbf{O}(\varepsilon^3)\\&=-\frac{1}{\tau}(\bar{f}_\alpha-\bar{f}_\alpha^{eq})-\frac{(2\bar{\tau}-1)}{2\bar{\tau}r}\bar{e}_{\alpha r}\varepsilon(\bar{f}_\alpha-\bar{f}_\alpha^{eq})+\frac{S_\phi}{4}\varepsilon.\end{aligned}\tag{4.108}$$

For the term S_ϕ, a centred method is once more applied.

$$S_\phi=S_\phi\left(\mathbf{X}+\frac{1}{2}\bar{e}_\alpha\varepsilon,t+\frac{1}{2}\varepsilon\right).\tag{4.109}$$

It is expanded by the Taylor series to read as follows:

$$S_\phi\left(\mathbf{X}+\frac{1}{2}\bar{e}_\alpha\varepsilon,t+\frac{1}{2}\varepsilon\right)=S_\phi(\mathbf{X},t)+\frac{1}{2}\varepsilon\left(\frac{\partial}{\partial t}+\bar{e}_{\alpha j}\frac{\partial}{\partial x_j}\right)S_\phi(\mathbf{X},t)+\mathbf{O}(\varepsilon^3)\tag{4.110}$$

Eq. 4.108 to the order of ε^0 is obtained by combining Eqs. 4.69 and 4.110 into Eq. 4.108 hence,

$$\bar{f}_\alpha^{(0)}=\bar{f}_\alpha^{eq},\tag{4.111}$$

to the order of ε is

$$\left(\frac{\partial}{\partial t}+\bar{e}_{\alpha j}\frac{\partial}{\partial x_j}\right)\bar{f}_\alpha^{(0)}=-\frac{\bar{f}_\alpha^{(1)}}{\bar{\tau}}+\frac{S_\phi}{4},\tag{4.112}$$

and to the order of ε^2 is

$$\begin{aligned}&\left(\frac{\partial}{\partial t}+\bar{e}_{\alpha j}\frac{\partial}{\partial x_j}\right)\bar{f}_\alpha^{(1)}+\frac{1}{2}\left(\frac{\partial}{\partial t}+\bar{e}_{\alpha j}\frac{\partial}{\partial x_j}\right)^2\bar{f}_\alpha^{(0)}=-\frac{\bar{f}_\alpha^{(2)}}{\bar{\tau}}-\frac{(2\bar{\tau}-1)}{2\bar{\tau}r}\bar{e}_{\alpha r}\bar{f}_\alpha^{(1)}\\&+\frac{1}{2}\left(\frac{\partial}{\partial t}+\bar{e}_{\alpha j}\frac{\partial}{\partial x_j}\right)\frac{S_\phi}{4}.\end{aligned}\tag{4.113}$$

Equation (4.112) is substituted into Eq. 4.113 to produce

$$\frac{(2\bar{\tau}-1)}{2\bar{\tau}r}\left(\frac{\partial}{\partial t}+\bar{e}_{\alpha j}\frac{\partial}{\partial x_j}\right)\bar{f}_\alpha^{(1)}=-\frac{\bar{f}_\alpha^{(2)}}{\bar{\tau}}-\frac{(2\bar{\tau}-1)}{2\bar{\tau}r}\bar{e}_{\alpha r}\bar{f}_\alpha^{(1)}.\tag{4.114}$$

Taking $\sum(Eq.(4.112) + \varepsilon \times Eq.4.114)$ above α results in

$$\frac{\partial}{\partial t}\sum_{\alpha} \bar{f}_{\alpha}^{(0)} + \frac{\partial}{\partial x_i}\sum_{\alpha} \bar{e}_{\alpha j}\bar{f}_{\alpha}^{(0)} = \frac{\partial \Gamma_i}{\partial x_i} + \frac{\Gamma_r}{r} + S_{\phi}, \tag{4.115}$$

where

$$\Gamma_i = -\frac{\varepsilon}{2\bar{\tau}}(2\bar{\tau}-1)\sum_{\alpha} \bar{e}_{\alpha i}\bar{f}_{\alpha}^{(1)}, \tag{4.116}$$

and

$$\Gamma_r = -\frac{\varepsilon}{2\bar{\tau}}(2\bar{\tau}-1)\sum_{\alpha} \bar{e}_{\alpha r}\bar{f}_{\alpha}^{(1)}, \tag{4.117}$$

combining Eq. 4.112 with Eq. 4.116 results in

$$\Gamma_i = \frac{\varepsilon}{2}(2\bar{\tau}-1)\sum_{\alpha} \bar{e}_{\alpha i}\left(\frac{\partial}{\partial t} + \bar{e}_{\alpha j}\frac{\partial}{\partial x_j}\right)\bar{f}_{\alpha}^{(0)}, \tag{4.118}$$

combining Eq. 4.112 with Eq. 4.116,

$$\Gamma_i = \frac{\varepsilon}{2}(2\bar{\tau}-1)\left(\frac{\partial}{\partial t}\sum_{\alpha} \bar{e}_{\alpha i}\bar{f}_{\alpha}^{(0)} + \frac{\partial}{\partial x_j}\sum_{\alpha} \bar{e}_{\alpha i}\bar{e}_{\alpha j}\bar{f}_{\alpha}^{(0)}\right). \tag{4.119}$$

The term $\dfrac{\partial}{\partial t}\bar{e}_{\alpha i}\bar{e}_{\alpha j}\bar{f}^{(0)}$ is of the order of $\rho U_c^2/t_c$ from Eq. 4.106 and the term $\dfrac{\partial}{\partial x_j}\sum_{\alpha} \bar{e}_{\alpha i}\bar{e}_{\alpha j}e_{\alpha k}\bar{f}_{\alpha}^{(0)}$ is of the order of $\rho e^2 U_c^2/L_c$ from Eq. 4.107. Using this information, we determine that the ratio of the former to the latter terms is of the order

$$\begin{aligned}\mathbf{O}\left(\frac{\frac{\partial}{\partial t}\Pi_{ij}^{(0)}}{\frac{\partial}{\partial x_k}\sum_{\alpha} e_{\alpha i}e_{\alpha r}e_{\alpha k}f_{\alpha}^{(0)}}\right) =&\mathbf{O}\left(\frac{\rho U_c^2/t_c}{\rho e^2 U_c^2/L_c}\right) = \\ &\mathbf{O}\left(\frac{U_c}{e}\right)^2 = \mathbf{O}\left(\frac{U_c}{C_s}\right)^2 = \mathbf{O}\left(M^2\right)\end{aligned} \tag{4.120}$$

in which $M = U_c/C_s$ is the Mach number. The first term in Eq. 4.119 is negligible by comparison to the second term provided $M << 1$. This is consistent with the dynamics of the lattice Boltzmann method. As a result, Eq. 4.119 can be written as:

$$\Gamma_i = \frac{\varepsilon}{2}(2\bar{\tau} - 1)\frac{\partial}{\partial x_j}\sum_{\alpha} \bar{e}_{\alpha i}\bar{e}_{\alpha j}\bar{f}_{\alpha}^{(0)}, \tag{4.121}$$

Inserting the Eq. 4.107 into the Eq. 4.121,

$$\Gamma_i = \bar{\nu}\frac{\partial(\rho u_{\phi})}{\partial x_i} \tag{4.122}$$

where the kinematic viscosity $\bar{\nu}$ is indicated by

$$\bar{\nu} = \frac{e^2\Delta t}{4}(2\bar{\tau} - 1). \tag{4.123}$$

Similarly

$$\Gamma_r = \bar{\nu}\frac{\partial(\rho u_{\phi})}{\partial r} \tag{4.124}$$

Eq. 4.104, Eq. 4.105, Eq. 4.122, and Eq. 4.124 are substituted into Eq. 4.115. If one assumes that the density variation is sufficiently small, we obtain the governing equation (4.97). The same kinematic viscosity, $\bar{\nu} = \nu$, is required for hydrodynamic consistency, leading to

$$\bar{\nu} = \frac{1}{2} + \frac{1}{3}(2\tau - 1). \tag{4.125}$$

As can be seen from the above formulae, the technique does not include any calculation involving a velocity gradient, and the additional source/sink term that is added is identical to that in the governing equation without the velocity gradient.

4.7 Stability Conditions

As with all CFD approaches, the lattice Boltzmann equation method can also suffer from numerical instability. Theoretically, the stability criteria of LBM are unknown.

In practice, diffusion is present, given that the lattice Boltzmann equation models actual water flow. This means that the kinematic viscosity ν must be positive [124], as shown by :

$$\nu = \frac{e^2 \Delta t}{6}(2\tau - 1) > 0. \tag{4.126}$$

As a result, an apparent restriction on the relaxation time is:

$$\tau > \frac{1}{2}. \tag{4.127}$$

It should be noted that these criteria are readily met by selecting appropriate relaxation time values. In addition, the time step should follow

$$\Delta t = \frac{\Delta x}{e}. \tag{4.128}$$

Normally, the lattice velocity magnitude e should not be set to be considerably larger than the flow speed. This criterion ensures that the axisymmetric lattice Boltzmann technique is stable.

Chapter 5

Initial and Boundary Conditions

5.1 Introduction

The proper selection of boundary conditions is critical in numerical fluid dynamics when solving the governing equation. Several commonly used boundary conditions, such as no-slip, slip, and semi-slip, are discussed in this chapter. It is well known that boundary conditions significantly impact the accuracy and stability of simulation outcomes [123]. References [113, 132, 133, 134] are desirable and relevant studies. In the contact of LMB, Research on the importance of boundary and initial conditions on conventional CFD simulation has also received a lot of attention [?, 135, 136]. Succi [137] distinguished two types of boundary conditions in fluid dynamics: simple boundary conditions, which refer to conditions at a boundary that are relatively straightforward to apply and complex boundary conditions involve more intricate or challenging conditions to implement. The following are brief explanations of several sorts of boundaries.

5.2 Solid Boundary Conditions

5.2.1 No-slip Boundary Condition

Standard bounce back scheme

Lattice gas cellular automata LGCA boundary conditions, which are simple and frequently utilised in constructing wall boundary conditions, were used to generate the conventional bounce-back scheme [138, 139]. During the streaming stage, the post-collision distributions function in the lattice Boltzmann equation (4.29) from a solid node x_b to a fluid node x_f is unknown. The bounce-back approach is used to solve unknown distribution functions in the lattice Boltzmann equation [140]. To put it another way, the distribution function for a particle $f_\alpha(x_f, t)$ arriving at the wall boundary is reflected back into the fluid (see Figure 5.1).

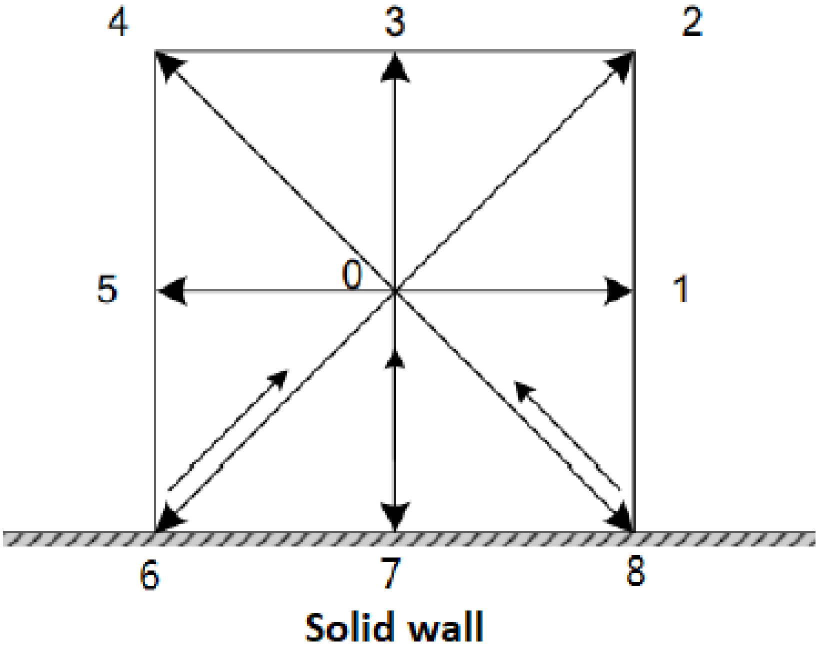

Figure 5.1: Layout of no-slip boundary conditions.

The bounce-back approach for a stationary wall is similar to establishing the distribution function as follows [140]:

$$f_2 = f_6, \tag{5.1}$$

$$f_3 = f_7, \tag{5.2}$$

$$f_4 = f_8. \tag{5.3}$$

Zero momentum of the particle near the solid wall is calculated using the above equations, resulting in a first-order no-slip boundary condition [140]. To attain second-order precision, the wall must be positioned in the centre of the lattice nodes, e.g. $x = 1/2$ with an extra staircase boundary method adjustment [113, 141].

Second-order bounce-back condition

For particles at the non-slip interface boundary, the lattice Boltzmann technique has historically been utilised with a bounce-back boundary condition. The bounce-back approach involves particles travelling toward a solid wall, then reflecting back into the fluid zone in the opposite direction while maintaining their velocity. For example, consider particles at the bottom boundary. A unit cell at the bottom boundary is depicted in Fig. 5.2. Let us start with the assumption that the fluid-solid interface boundary is on line A. The fluid is represented by the lattice sites 2, 3, 4 above the border, whereas the solid is represented by the lattice sites 6, 7, and 8 below the boundary. The lattice locations 1, 0, and 5 are on the edge. At time t, a given particle is at node 0 with location $\boldsymbol{X}$. A particle at $(\boldsymbol{X}, t)$ travelling into the solid area in the directions $\mathbf{e}_6$, $\mathbf{e}_7$, $\mathbf{e}_8$ reflectS back from boundary into the location $\boldsymbol{X}$, changing to the opposite directions $\mathbf{e}_2$, $\mathbf{e}_3$, $\mathbf{e}_4$ at the following time step *t+1*. The reflection form is,

$$f_2(\mathbf{X}, t+1) = f_6(\mathbf{X}, t) - \frac{1}{\tau}\left(f_6(\mathbf{X}, t) - f_6^{eq}(\mathbf{X}, t)\right), \tag{5.4}$$

$$f_3(\mathbf{X}, t+1) = f_7(\mathbf{X}, t) - \frac{1}{\tau}\left(f_7(\mathbf{X}, t) - f_7^{eq}(\mathbf{X}, t)\right), \tag{5.5}$$

$$f_4(\mathbf{X}, t+1) = f_8(\mathbf{X}, t) - \frac{1}{\tau}\left(f_8(\mathbf{X}, t) - f_8^{eq}(\mathbf{X}, t)\right). \tag{5.6}$$

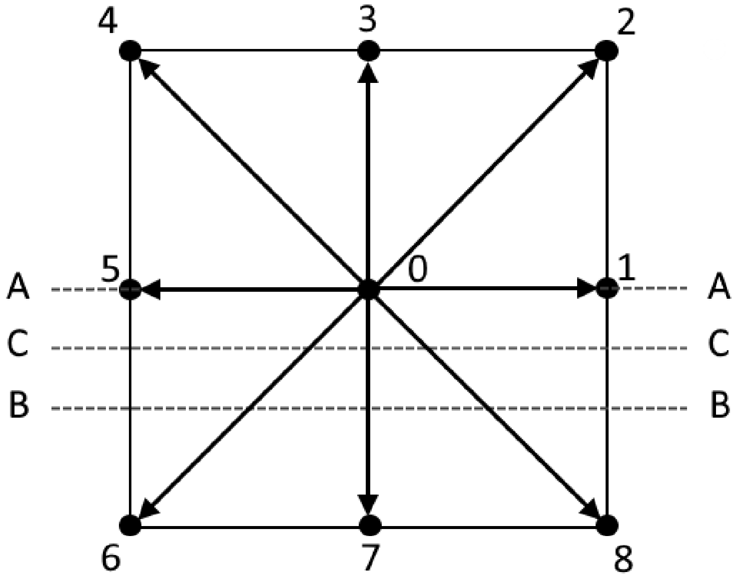

Figure 5.2: Unit cell for a particle in a two-dimensional square lattice. Line B is located midway between line A and the line linking lattice sites 6 and 8. Line C is located midway between lines A and B.

Distribution functions in directions other than $\mathbf{e}_6$, $\mathbf{e}_7$, $\mathbf{e}_8$ are calculated by the LBGK equation [38]

$$f_i(\mathbf{X} + \mathbf{e}_i, t+1) = f_i(\mathbf{X}, t) - \frac{1}{\tau}\left(f_i(\mathbf{X}, t) - f_i^{eq}(\mathbf{X}, t)\right), \qquad i = 0, 1, 2, 3, 4, 5. \tag{5.7}$$

This bounce-back method is first-order accurate. Kim [104] applied an interpolation parameter ω to the particles travelling in the $\mathbf{e}_6$, $\mathbf{e}_7$ and $\mathbf{e}_8$ directions. The particle distributions are calculated by

$$f_2(\mathbf{X}, t+1) = f_6(\mathbf{X}, t) - \frac{\omega}{\tau}\left(f_6(\mathbf{X}, t) - f_6^{eq}(\mathbf{X}, t)\right), \tag{5.8}$$

$$f_3(\mathbf{X}, t+1) = f_7(\mathbf{X}, t) - \frac{\omega}{\tau}\left(f_7(\mathbf{X}, t) - f_7^{eq}(\mathbf{X}, t)\right), \tag{5.9}$$

,

$$f_4(\mathbf{X}, t+1) = f_8(\mathbf{X}, t) - \frac{\omega}{\tau}\left(f_8(\mathbf{X}, t) - f_8^{eq}(\mathbf{X}, t)\right). \tag{5.10}$$

Allowing $\omega = 0$ causes the reflection to occur at location $\mathbf{X}$ of line **A** in Fig. 5.2, and $\omega = 1$ causes the reflection to occur at $\mathbf{X} + \frac{1}{2}\mathbf{e}_7$ of line **B**. Allowing $0 < \omega < 1$ will cause the reflection to occur in between. Selecting of $\omega = \frac{1}{2}$, for example, causes the reflection to occur at the location $\mathbf{X} + \frac{1}{4}\mathbf{e}_7$ on the boundary represented by the line **C** in Fig. 5.2. The LBGK solution by the above bounce-back method of Eqs. 5.7 - 5.10 is second-order accurate where $\omega = \frac{1}{2}$ is chosen [104]. The line **C** in the picture is separated from the normal lattice sites by one-fourth of the mesh size.

5.2.2 Slip Boundary Condition

A slip boundary condition, which is shown in Fig. 6.2, should be used when the boundary is smooth and has negligible friction. Fluid flow of the wall should achieve tangential momentum equilibrium in this situation. Along the tangential direction, there is no momentum transfer to the wall. The other unknown distribution functions f_2, f_3 and f_4 are given by

$$f_2 = f_8, \tag{5.11}$$

$$f_3 = f_7, \tag{5.12}$$

$$f_4 = f_6. \tag{5.13}$$

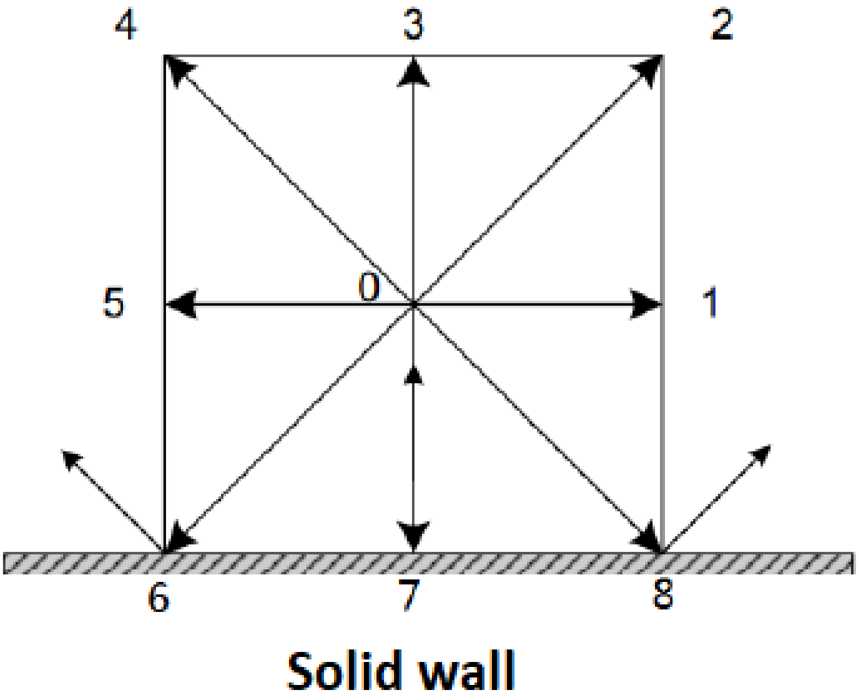

Figure 5.3: Slip boundary condition layout.

5.2.3 Semi-slip Boundary Condition

Wall shear stress, which occurs when fluid flows over a stationary frictional surface, causes the fluid in contact with the surface to come to rest [3, 142]. Due to friction, some fluid particles flow over the surface while others bounce back into the mainstream. At the microscopic scale, a thin layer of fluid travels tangentially along the surface; hence, a combination of no-slip and slip boundary conditions appears optimal results. There is no motion normal to the surface. To create a semi-slip boundary condition, Zhou [143] argued that it is necessary to take wall shear stress into account. An expression for the wall shear stress vector τ_f caused by wall friction is:

$$\tau_f = -\rho\nu \frac{\partial V\tau}{\partial n^*} = -\rho C_f \mid V_\tau \mid V_\tau, \tag{5.14}$$

where C_f is the friction factor at the wall, n^* is the outward coordinate normal to the wall, and V_τ is the velocity vector parallel to the wall. The Manning roughness n_f may be used to determine the wall friction factor as follows

$$C_f = \frac{gn_f^2}{r^{1/3}}, \tag{5.15}$$

where C_f is the Manning coefficient. If the slip boundary condition is implemented at a boundary node, the fluid velocity vector relative to the wall leads to zero, and so

$$V_\tau = v. \tag{5.16}$$

The tensor form of wall shear stress can be written as

$$\tau_{f_i} = -\rho C_f u_i \sqrt{u_i u_j}. \tag{5.17}$$

As a result, at a boundary node, a semi-slip boundary condition may be applied by incorporating wall shear stress τ_{f_i} in the force component F_i in the lattice Boltzmann equation (4.10) together with the slip boundary condition.

5.3 Inflow and Outflow Conditions

Proper inlet and outlet boundary conditions are critical for obtaining realistic simulation results because they act as limits to maintain consistency with the neighbouring flow conditions. Indeed, many flow characteristics (such as velocity and pressure) near the boundary must accurately reflect the condition.

It is typical in older numerical approaches to impose a particular fluid velocity at the outflow while assigning a predetermined velocity profile at the inlet [3]. It has been demonstrated that using zero gradients for these physical variables in the computational analysis of LBM yields adequate results [121]. As an illustration, in Fig. 5.4 the unknown f_1, f_2 and f_8 are easily determined after streaming by:

$$f_\alpha(1,j) = f_\alpha(2,j), \qquad \alpha = 1,2,8. \tag{5.18}$$

Similarly, the unknown distribution functions f_4, f_5 and f_6 for the outflow have the same relations:

$$f_\alpha(N_x,j) = f_\alpha(N_x-1,j), \qquad \alpha = 4,5,6. \tag{5.19}$$

where N_x denotes the total number of lattices in the x direction. All of the distribution functions can be adjusted to their respective local equilibrium distribution functions, $f_\alpha = f_\alpha^{eq}$ and $\overline{f}_\alpha = \overline{f}_\alpha^{eq}$, for axisymmetric flow with a swirl. This method was suggested by Zhou [14] and shown to yield precise solutions for rotating axisymmetric flows. The following chapters demonstrate how this might lead to precise solutions to the issue, even if an actual individual distribution function may differ from the local equilibrium distribution function. It should be emphasised that other methods, such as the non-equilibrium extrapolation method by Guo et al. [54], may be used to obtain correct solutions for flows with large non-equilibrium effects.

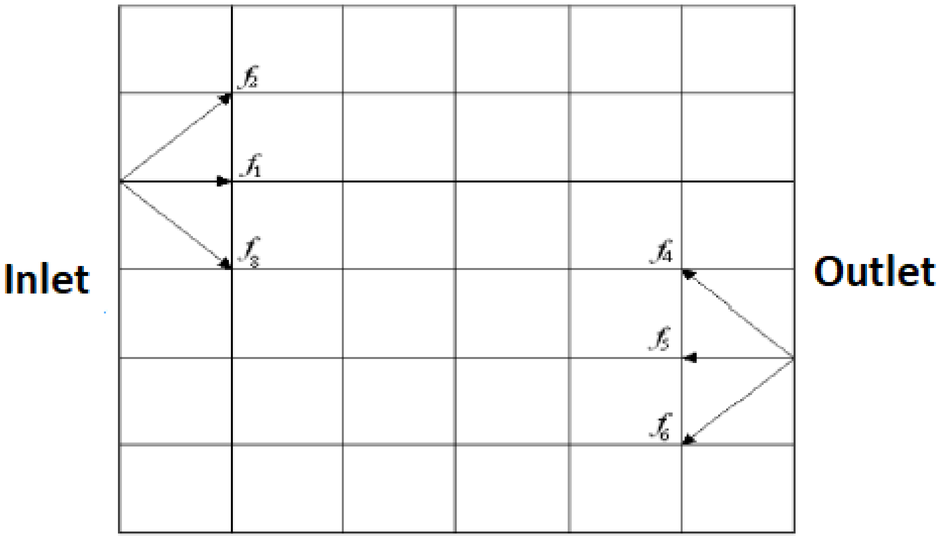

Figure 5.4: Sketch of inflow and outflow boundaries.

5.4 Periodic Boundary Condition

Periodic boundary conditions are utilised for a variety of reasons and in a variety of scenarios in computational fluid dynamics and other numerical simulations. They are used when it is acceptable to simulate a bounded region that repeats on a regular basis, allowing the simulation of a wider domain while using fewer computer resources. Examples are tidal flow and oscillating U-tube, Shear Flow and turbulence, repetitive geometries, and flow in channels and pipes. When the input and outflow borders of the computation are connected, the computational domain effectively becomes closed. The unknown f_1, f_2 and f_8 at the inflow boundary after streaming must be specified as equal to their counterparts at the outflow boundary in order to obtain a periodic boundary condition (see Fig. 5.5).

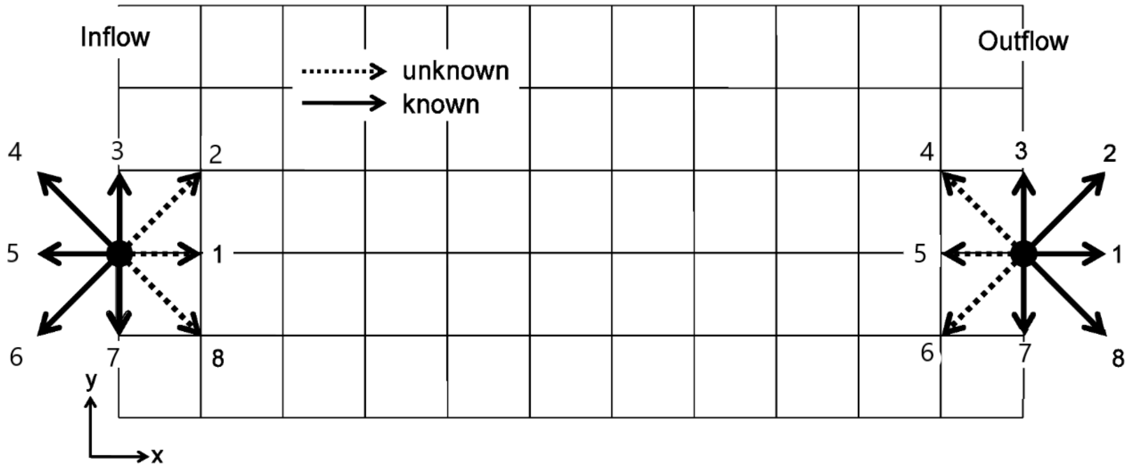

Figure 5.5: Sketch of the Periodic Boundary Condition

In this case,

$$f_\alpha(1, j) = f_\alpha(L_x, j), \qquad \alpha = 1, 2, 8. \tag{5.20}$$

The unknown f_4, f_5, and f_6 at the outflow boundary are equivalent to their counterparts at the inflow boundary, such that

$$f_\alpha(L_x, j) = f_\alpha(1, j), \qquad \alpha = 4, 5, 6, \tag{5.21}$$

where, L_x is the last node in the x direction inside the computational domain. A similar periodic boundary condition applies in the y direction.

5.5 Initial Condition

The flow field at the beginning of the simulation at $t = 0s$ is the initial condition. The distribution function must have a starting condition before being calculated. The starting condition in the lattice Boltzmann technique can be specified in one of two ways [15]. For the distribution function, one option is to enter a random number between 0 and 1. The alternative is first to establish a flow field with presupposed fluid velocity and density, and then to evaluate the local equilibrium distribution function, or f_α^{eq}, and use it as a starting point for f_α. The definition of a macroscopic value is typically simpler than a microscopic one. Thus, in actual computations, the second method—which is employed in the present model—is selected.

5.6 Solution Procedure

AxLAB® and AxLAB® with turbulence have fairly straightforward solution procedure consistency of the following actions and requiring explicit calculations:

1. Precall initial fluid density and flow velocity field.
2. Calculate f_α^{eq}.
3. Calculate f_α from the lattice Boltzmann equation.
4. Refresh fluid's density and flow velocity field.
5. Return to step 2 and repeat the procedure until a solution is reached.

The LBM calculating technique is depicted in the flow chart given in Fig. 5.6.

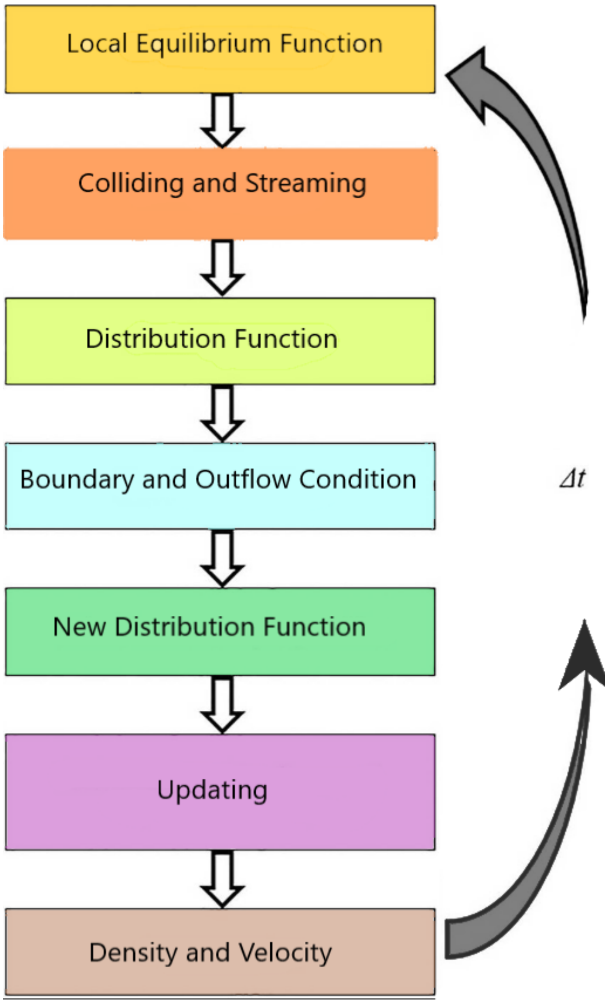

Figure 5.6: Flow chart for the LBM computation process

Chapter 6

Large Eddy Simulation of Turbulent Flow

6.1 Introduction

Axisymmetric lattice Boltzmann approaches have been documented for the vast majority of laminar axisymmetric flow equations without flow turbulence in the literature [144]. These techniques cannot be used for real-world natural flows because of the procedure of turbulence. The general rule is that flow turbulence may be described by adding another scheme, with the model utilising modified governing flow equations such as time-averaged or space-filtered flow. Teixeira [57] first proposed a lattice Boltzmann method for turbulent flows; which involved transforming the single relaxation time into a variable relaxation time governed by the solution of two differential equations, the $k - \varepsilon$ equations, where k is turbulent Kinetic Energy and ε stands for turbulent Dissipation Rate. Large eddy simulation (LES) successfully represents vorticity larger than a defined scale when space-filtered governing equations are utilised with an SGS stress model of the unresolved scale stress. The most straightforward and precise model in this class was developed by Smagorinsky [58], who used the eddy viscosity and a large-scale strain tensor to describe the Reynolds stress tensor. Following prior research [59], space-filtered flow equations are used in the present thesis because they are more accurate for turbulent flows. The lattice Boltzmann approach for simulating turbulence may integrate the conventional Smagorinsky SGS stress model, as demonstrated by Hou et al. [60]. In this case, the single relaxation time is changed to a variable relaxation time that is directly connected to the distribution function and eliminates the need for any derivative computations. A similar concept is used in this chapter to create an axisymmetric LBM for modelling turbulence. The chapter first presents a brief overview of generic modelling techniques for turbulent flows. The turbulent axisymmetric stress subgrid-scale model is then discussed. Finally, the axisymmetric flow governing equations are used to reconstruct the AxLAB® with turbulence.

6.2 AxLAB® with the Subgrid-Scale Stress Model (SGS)

With present computer technology, the majority of real-world, high-Reynolds-number flows in nature are too complex to be properly recreated. It is very difficult to forecast the behaviour of extremely turbulent flows without explicitly reproducing all motion scales. A useful method to overcome this constraint is a large eddy simulation based on a subgrid-scale stress model. Smagorinsky [58] created the simplest and most often used approach in this field by expressing the Reynolds stress tensor using the eddy viscosity and a large-scale strain tensor. Space-filtered flow equations, which are utilised in the present work, are thought to be more precise than time-averaged flow equations for the computation of turbulent flows, according to Tutar and Hold [59].

AxLAB®, which is described in Chapter 4 is an axisymmetric lattice Boltzmann model based on the axisymmetric flow equations without turbulence modelling. In the present thesis, AxLAB® is extended to modelling including turbulence [145]. It can be shown that the sole distinction between the axisymmetric flow equations (3.14) and (3.15) and the turbulent axisymmetric equations (3.45) and (3.46) is due to viscous factors. Unlike the conventional laminar axisymmetric flow equations, the turbulent axisymmetric flow equations incorporate additional viscosity that mimics the behaviour of turbulent eddies in the viscous factor. The only factor used to define the kinematic viscosity ν is the relaxation time from Eq. 4.64. Using eddy viscosity in the turbulence modelling,

$$\nu_e = \tau_e . \frac{e^2 \Delta t}{3}, \tag{6.1}$$

an updated relaxation time τ is given as:

$$\tau_t = \tau_\alpha + \tau_e, \tag{6.2}$$

The definition of a total viscosity, ν_t, is

$$\nu_t = \nu + \nu_e. \tag{6.3}$$

So, the lattice Boltzmann equation with total relaxation time τ_t may be expressed as follows:

$$f_\alpha(\mathbf{X} + \mathbf{e}_\alpha \Delta t, t + \Delta t) - f_\alpha(\mathbf{X}, t) = -\tau_{\alpha t}(f\alpha - f_\alpha^{eq}) + \omega_\alpha \theta \Delta t + \frac{\Delta t}{\kappa e^2} e_{\alpha i} F_i \tag{6.4}$$

where

$$\tau_{\alpha t} = \begin{cases} \frac{1}{\tau_t}, & r = 0 \\ \frac{1}{\tau_t}\left[1 + \dfrac{(2\tau_t - 1)e_{\alpha r}\Delta t}{2r}\right], & r \neq 0, \end{cases} \tag{6.5}$$

and

$$F_i = -\frac{\rho u_i u_r}{r} - \frac{2\rho \nu_t u_i}{r^2}\delta_{ir}. \tag{6.6}$$

This equation, along with Eqs. 3.45 and 3.46, can be used to find the solution of the turbulent axisymmetric flow equations. The lattice Boltzmann approach and a subgrid-scale stress model were presented by Hou et al. [60] using this as its fundamental premise. In this method, the standard version of the lattice Boltzmann equations was used to simply and effectively represent flow turbulence.

The total relaxation time τ_t is now determined. The strain-rate tensor S_{ij} requires the computation of derivatives, which are problematic to apply, as stated in Eq. 3.43. It makes sense have to calculate S_{ij} in terms of the distribution function to maintain consistency with the lattice gas dynamics. The strain-rate tensor S_{ij} is readily calculated by utilising the Chapman-Enskog expansion given that it is connected to the non-equilibrium momentum flux tensor as follows:

$$S_{ij} = -\frac{3}{2e^2\rho\tau_t\Delta t}\sum_{\alpha} e_{\alpha i}e_{\alpha j}\left(f_\alpha - f_\alpha^{eq}\right). \tag{6.7}$$

Assuming that ν_t and τ_t also meet the relation Eq. 4.64, we have

$$\tau_t = \frac{1}{2} + \frac{3\nu_t}{e^2\Delta t}. \tag{6.8}$$

Eqs. 6.2 and 6.3 are substituted into Eq. 6.8 to produce

$$\tau_e + \tau = \frac{1}{2} + \frac{3(\nu_e + \nu)}{e^2\Delta t}. \tag{6.9}$$

When Eq. 4.64 is substituted into the above equation, the result is

$$\tau_e = \frac{3}{e^2\Delta t}\nu_e. \tag{6.10}$$

Eq. 3.42 is substituted into the previous equation to obtain

$$\tau_e = \frac{3}{e^2\Delta t}(C_s l_s)^2\sqrt{S_{ij}S_{ij}}. \tag{6.11}$$

Eq. 6.7 may be inserted into Eq. 6.11 to give

$$\tau_e = \frac{3}{e^2\Delta t}(C_s l_s)^2\frac{3}{2e^2\rho\tau_t\Delta t}\sqrt{\Pi_{ij}\Pi_{ij}}, \tag{6.12}$$

where

$$\Pi_{ij} = \sum_{\alpha} e_{\alpha i} e_{\alpha j} \big(f_\alpha - f_\alpha^{eq} \big). \tag{6.13}$$

Letting $l_s = \Delta t$ and replacing to Eq. 6.2, hence Eq. 6.12 becomes

$$\tau_e = \frac{9C_s^2}{2e^2 \rho (\tau + \tau_e)} \sqrt{\Pi_{ij}\Pi_{ij}}, \tag{6.14}$$

Finally, the eddy relaxation time may be calculated by solving Eq. 6.14 and disregarding the negative value of τ_e,

$$\tau_e = \frac{-\tau + \sqrt{\tau^2 + 18C_s^2/(e^2\rho)\sqrt{\Pi_{ij}\Pi_{ij}}}}{2}, \tag{6.15}$$

As a result, Eq. 6.2 gives the total relaxation time τ_t as

$$\tau_t = \frac{\tau + \sqrt{\tau^2 + 18C_s^2/(e^2\rho)\sqrt{\Pi_{ij}\Pi_{ij}}}}{2}. \tag{6.16}$$

Flow turbulence may be simply and intuitively described in the basic lattice Boltzmann equation with total relaxation time τ_t which includes the eddy relaxation time τ_e form Eq. 5.2. The 2D incompressible axisymmetric turbulent flow equations Eqs. 3.14 and 5.17 may be retrieved from the lattice Boltzmann equation 4.57 via Chapman-Enskog analysis,

$$\frac{\partial u_i}{\partial t} + \frac{\partial (u_i u_j)}{\partial x_j} = -\frac{1}{\rho}\frac{\partial p}{\partial x_j} + \nu_t \frac{\partial}{\partial x_j}\left(\frac{\partial u_i}{\partial x_j} + \frac{\partial u_j}{\partial x_i}\right) + \frac{\nu_t}{r}\left(\frac{\partial u_i}{\partial r} + \frac{\partial u_r}{\partial x_i}\right) - \frac{u_i u_r}{r} - \frac{2\nu_t u_i}{r^2}\delta_{ij}. \tag{6.17}$$

6.3 Recovery of the AxLAB® with Turbulence

This section explains how the lattice Boltzmann equation (6.4) was used to extract the turbulent axisymmetric flow equations (3.45) and (3.46). Assuming that Δt is small and equal to ε,

$$\Delta t = \varepsilon. \tag{6.18}$$

Substituting the aforementioned equation into Eq. 6.4, using Eq. 6.5, yields

$$\begin{aligned} f_\alpha(\mathbf{X} + \mathbf{e}_\alpha\varepsilon, t + \varepsilon) - f_\alpha(\mathbf{X}, t) = -\frac{1}{\tau_t}(f\alpha - f_\alpha^{eq}) - \frac{(2\tau_t - 1)}{2\tau_t r} e_{\alpha r}\varepsilon(f\alpha - f_\alpha^{eq}) \\ + \omega_\alpha\theta\varepsilon + \frac{\varepsilon}{6e^2} e_{\alpha i}F_i. \end{aligned} \tag{6.19}$$

By applying a Taylor expansion to Eq. 6.19, at point (x, t), in time and space,

$$\begin{aligned} &\varepsilon\left(\frac{\partial}{\partial t} + e_{\alpha j}\frac{\partial}{\partial x_j}\right) + \frac{1}{2}\varepsilon^2\left(\frac{\partial}{\partial t} + e_{\alpha j}\frac{\partial}{\partial x_j}\right)^2 f_\alpha + \mathbf{O}(\varepsilon^3) \\ &= -\frac{1}{\tau_t}(f_\alpha - f_\alpha^{eq}) - \frac{(2\tau_t - 1)}{2\tau_t r} e_{\alpha r}\varepsilon(f_\alpha - f_\alpha^{eq}) + \omega_\alpha\theta\varepsilon + \frac{\varepsilon}{6e^2} e_{\alpha i}F_i. \end{aligned} \tag{6.20}$$

The Chapman-Enskog extension states that f_α may be expressed as a series of ε,

$$f_\alpha = f_\alpha^{(0)} + \varepsilon f_\alpha^{(1)} + \varepsilon^2 f_\alpha^{(2)} + \mathbf{O}(\varepsilon^3) \tag{6.21}$$

For the source term and force term F_i, the centred scheme is employed as

$$\theta = \theta\left(\mathbf{X} + \frac{1}{2}e_\alpha\varepsilon, t + \frac{1}{2}\varepsilon\right) \tag{6.22}$$

and

$$F_i = F_i\left(\mathbf{X} + \frac{1}{2}e_\alpha\varepsilon, t + \frac{1}{2}\varepsilon\right) \tag{6.23}$$

which, after Taylor expansion, may be expressed as

$$\theta\left(\mathbf{X} + \frac{1}{2}e_\alpha\varepsilon, t + \frac{1}{2}\varepsilon\right) = \theta(\mathbf{X}, t) + \frac{1}{2}\varepsilon\left(\frac{\partial}{\partial t} + e_{\alpha j}\frac{\partial}{\partial x_j}\right)\theta(\mathbf{X}, t) + O(\varepsilon^2) \tag{6.24}$$

and

$$F_i\left(\mathbf{X}+\frac{1}{2}e_\alpha\varepsilon, t+\frac{1}{2}\varepsilon\right) = F_i(\mathbf{X},t)+\frac{1}{2}\varepsilon\left(\frac{\partial}{\partial t}+e_{\alpha j}\frac{\partial}{\partial x_j}\right)F_i(\mathbf{X},t)+O(\varepsilon^2). \tag{6.25}$$

After substituting Eqs. 6.21, 6.24, and 6.25 into Eq. 6.20, the following equations are obtained to order $\varepsilon^{(0)}$

$$f_\alpha^{(0)} = f_\alpha^{eq}, \tag{6.26}$$

to order ε

$$\left(\frac{\partial}{\partial t}+e_{\alpha j}\frac{\partial}{\partial x_j}\right)f_\alpha^{(0)} = -\frac{f_\alpha^{(1)}}{\tau_t}+\omega_\alpha\theta+\frac{1}{6e^2}e_{\alpha i}F_i, \tag{6.27}$$

and to order ε^2 is

$$\begin{aligned}\left(\frac{\partial}{\partial t}+e_{\alpha j}\frac{\partial}{\partial x_j}\right)f_\alpha^{(1)}+\frac{1}{2}\left(\frac{\partial}{\partial t}+e_{\alpha j}\frac{\partial}{\partial x_j}\right)^2 f_\alpha^{(0)} &= -\frac{f_\alpha^{(2)}}{\tau_t}-\frac{(2\tau_t-1)}{2\tau_t r}e_{\alpha r}f_\alpha^{(1)}\\ +\frac{1}{2}\left(\frac{\partial}{\partial t}+e_{\alpha j}\frac{\partial}{\partial x_j}\right)(\omega_\alpha\theta)+\frac{1}{12e^2}\left(\frac{\partial}{\partial t}+e_{\alpha j}\frac{\partial}{\partial x_j}\right)(e_{\alpha i}F_i).&\end{aligned} \tag{6.28}$$

Using Eq. 6.27, Eq. 6.28 becomes:

$$\frac{(2\tau_t-1)}{2\tau_t}\left(\frac{\partial}{\partial t}+e_{\alpha j}\frac{\partial}{\partial x_j}\right)f_\alpha^{(1)} = -\frac{f_\alpha^{(2)}}{\tau_t}-\frac{(2\tau_t-1)}{2\tau_t}e_{\alpha r}f_\alpha^{(1)}. \tag{6.29}$$

By applying Eq. (6.27)+$\varepsilon\times$Eq. (6.29),

$$\begin{aligned}&\left(\frac{\partial}{\partial t}+e_{\alpha j}\frac{\partial}{\partial x_j}\right)f_\alpha^{(0)}+\frac{(2\tau_t-1)\varepsilon}{2\tau_t}\left(\frac{\partial}{\partial t}+e_{\alpha j}\frac{\partial}{\partial x_j}\right)f_\alpha^{(1)}\\ &=\frac{1}{\tau_t}(f_\alpha^{(1)}-\varepsilon f_\alpha^{(2)})-\frac{(2\tau_t-1)\varepsilon}{2\tau_t}e_{\alpha r}f_\alpha^{(1)}+\omega_\alpha\theta+\frac{1}{6e^2}e_{\alpha i}F_i.\end{aligned} \tag{6.30}$$

The sum of the foregoing equation (6.28) over α yields

$$\frac{\partial}{\partial t}\sum_\alpha f_\alpha^{(0)}+\frac{\partial}{\partial x_j}\sum_\alpha e_{\alpha j}f_\alpha^{(0)} = \theta. \tag{6.31}$$

The continuity equation is reestablished by applying Eq. 6.26 and substituting Eqs. 4.64and 4.65 into the Eq. 3.14 provided the density fluctuation is and small enough to be negligible.

Taking $\sum(Eq.(6.27) + \varepsilon \times Eq.6.29)$ for each α results in

$$\frac{\partial}{\partial t}\sum_{\alpha} e_{\alpha i} f_{\alpha}^{(0)} + \frac{\partial \Pi_{ij}^{(0)}}{\partial x_j} = \frac{\partial \Lambda_{ij}}{\partial x_j} + \frac{\Lambda_{ij}}{r} + F_i, \tag{6.32}$$

where the following formulae represent the zero-order momentum flux tensor:

$$\Pi_{ij}^{(0)} = \sum_{\alpha} e_{\alpha i} e_{\alpha j} f_{\alpha}^{(0)}, \tag{6.33}$$

$$\Lambda_{ij} = -\frac{\varepsilon}{2\tau_t}(2\tau_t - 1)\sum_{\alpha} e_{\alpha i} e_{\alpha j} f_{\alpha}^{(1)}, \tag{6.34}$$

$$\Lambda_{ij} = -\frac{\varepsilon}{2\tau_t}(2\tau_t - 1)\sum_{\alpha} e_{\alpha i} e_{\alpha r} f_{\alpha}^{(1)}, \tag{6.35}$$

By reviewing the terms in Eq. 6.33 using Eq. 4.55,

$$\Pi_{ij}^{(0)} = P\delta_{ij} + \rho u_i u_j, \tag{6.36}$$

where $P = \rho e^2/3$ is the pressure, resulting in a speed of sound $C_s = e/\sqrt{3}$. Substituting Eq. 6.36 into Eq. 6.32, the result is

$$\frac{\partial(\rho u_i)}{\partial t} + \frac{\partial(\rho u_i u_j)}{\partial x_j} = -\frac{\partial P}{\partial x_i} + \frac{\partial \Lambda_{ij}}{j} + \frac{\Lambda_{ir}}{r} + F_i. \tag{6.37}$$

Eq. 6.34 may be rewritten using Eq. 6.27 as:

$$\Lambda_{ij} = \Pi_{ij}^{(1)} - \frac{\varepsilon}{2}(2\tau_t - 1)\sum_{\alpha} e_{\alpha i} e_{\alpha r} \omega_{\alpha} \theta. \tag{6.38}$$

Using the first-order momentum flux tensor $\Pi_{ij}^{(1)}$, which is described by

$$\Pi_{ij}^{(1)} = \frac{\varepsilon}{2}(2\tau_t - 1)\sum_{\alpha} e_{\alpha i} e_{\alpha r} \left(\frac{\partial}{\partial t} + e_{\alpha k}\frac{\partial}{\partial x_k}\right) f_{\alpha}^{(0)}, \tag{6.39}$$

then, using Eq. 6.33, we obtain:

$$\Pi_{ij}^{(1)} = \frac{\varepsilon}{2}(2\tau_t - 1)\frac{\partial}{\partial t}\Pi_{ij}^{(0)} + \frac{\varepsilon}{2}(2\tau_t - 1)\frac{\partial}{\partial x_k}\sum_{\alpha} e_{\alpha i}e_{\alpha r}e_{\alpha k}f_{\alpha}^{(0)}, \tag{6.40}$$

With Eqs. 4.55, 6.37 and 6.26, the second term in Eq. 6.40 may be expressed:

$$\frac{\partial}{\partial x_k}\sum_{\alpha} e_{\alpha i}e_{\alpha r}e_{\alpha k}f_{\alpha}^{(0)} = \frac{e^2}{3}\frac{\partial}{\partial x_k}(\rho u_i\delta_{jk} + \rho u_j\delta_{ki} + \rho u_k\delta_{ij}). \tag{6.41}$$

For a characteristic velocity U_c, characteristic length L_c and characteristic time t_c, the term $\frac{\partial}{\partial t}\Pi_{ij}^{(0)}$ is of order $\rho U_c^2/t_c$, and the term $\frac{\partial}{\partial x_k}\sum_\alpha e_{\alpha i}e_{\alpha r}e_{\alpha k}f_{\alpha}^{(0)}$ is of order $\rho e^2 U_c^2/L_c$. Using this information, we determine that the ratio of the former to the latter terms is of order

$$\begin{aligned}\mathbf{O}\left(\frac{\frac{\partial}{\partial t}\Pi_{ij}^{(0)}}{\frac{\partial}{\partial x_k}\sum_\alpha e_{\alpha i}e_{\alpha r}e_{\alpha k}f_{\alpha}^{(0)}}\right) =&\mathbf{O}\left(\frac{\rho U_c^2/t_c}{\rho e^2 U_c^2/L_c}\right) = \\ &\mathbf{O}\left(\frac{U_c}{e}\right)^2 = \mathbf{O}\left(\frac{U_c}{C_s}\right)^2 = \mathbf{O}\left(M^2\right)\end{aligned} \tag{6.42}$$

in which $M = U_c/C_s$ is the Mach number. The first term in Eq. 6.41 is negligible by comparison to the second term for $M << 1$. This is in accordance with lattice Boltzmann dynamics. As a result, when Eq. 6.42 is substituted into Eq. 6.41, the new equation becomes

$$\Pi_{ij}^{(1)} = \frac{e^2\varepsilon}{6}(2\tau_t - 1)\frac{\partial}{\partial x_k}(\rho u_i\delta_{jk} + \rho u_j\delta_{ki} + \rho u_k\delta_{ij}), \tag{6.43}$$

or

$$\Pi_{ij}^{(1)} = \nu_t\left[\frac{\partial(\rho u_i)}{\partial x_j} + \frac{\partial(\rho u_j)}{\partial x_i} + \frac{\partial(\rho u_k)}{\partial x_k}\delta_{ij}\right], \tag{6.44}$$

where ν_t is the kinematic viscosity, given by

$$\nu_t = \frac{e^2\Delta t}{6}(2\tau_t - 1). \tag{6.45}$$

By inserting Eq. 6.44 into Eq. 6.38 and evaluating the remaining terms we obtain

$$\Lambda_{ij} = \nu_t\left[\frac{\partial(\rho u_i)}{\partial x_j} + \frac{\partial(\rho u_j)}{\partial x_i} + \frac{\partial(\rho u_k)}{\partial x_k}\delta_{ij}\right] - \nu_t\theta\delta_{ij}. \tag{6.46}$$

Solving the aforementioned problem using $\theta = -u_r/r$ and continuity Eq. 3.14, gives

$$\Lambda_{ij} = \nu_t\left[\frac{\partial(\rho u_i)}{\partial x_j} + \frac{\partial(\rho u_j)}{\partial x_i}\right], \tag{6.47}$$

and

$$\Lambda_{ir} = \nu_t\left[\frac{\partial(\rho u_i)}{\partial x_r} + \frac{\partial(\rho u_r)}{\partial x_i}\right]. \tag{6.48}$$

Eq. 6.6, Eq. 6.47, Eq. 6.48 and Eq. 6.37, yield

$$\begin{aligned}\frac{\partial(\rho u_i)}{\partial t} + \frac{\partial(\rho u_i u_j)}{\partial x_j} =& -\frac{\partial P}{\partial x_i} + \nu_t\frac{\partial}{\partial x_j}\left[\frac{\partial(\rho u_i)}{\partial x_j} + \frac{\partial(\rho u_j)}{\partial x_i}\right]\\ &+ \frac{\nu_t}{r}\left[\frac{\partial(\rho u_i)}{\partial x_r} + \frac{\partial(\rho u_r)}{\partial x_i}\right] - \frac{\rho u_i u_r}{r} - \frac{2\rho\nu_t u_i}{r^2}\delta_{ij}.\end{aligned} \tag{6.49}$$

The above reduces to the momentum equation so the density variation approaches zero,

$$\frac{\partial u_j}{\partial x_j} + \frac{u_r}{r} = 0, \tag{6.50}$$

$$\frac{\partial u_i}{\partial t} + u_j\frac{\partial u_i}{\partial x_j} = -\frac{1}{\rho}\frac{\partial p}{\partial x_j} + \nu_t\frac{\partial^2 u_i}{\partial^2 x_j} + \frac{\nu_t}{r}\frac{\partial u_i}{\partial r} - \frac{\nu_t u_i}{r^2}\delta_{ij}. \tag{6.51}$$

Chapter 7

Numerical study of vortex breakdown phenomena

7.1 Introduction

Swirling flows are often employed in engineering applications in aeronautics, heat exchange, spray drying, separation, combustion, etc. They occur in natural flows such as tornadoes and typhoons. Such flows are fascinating because of their significance and intricacy. For combustion systems, such as gas turbine engines, industrial burners, boilers, and diesel engines, swirling flows were initially employed to enhance and regulate the mixing rate in order to create flames, between fuel and oxidant streams [16]. In practice, an internal recirculation zone is created at a suitable level of swirl, facilitating a high rate of heat release when the combustion products are recirculated and igniting the incoming fuel/oxidant streams. This produces a steady, compact flame [17] that performs well with challenging carboneous materials and substandard gases [18]. It has been demonstrated that swirl has significant influence on the flow field at large scale [146]. Swirl represents the ratio of the radial velocity component to the axial (tangential) velocity component. When swirl is added to a turbulent jet, the rate of entrainment, decay, and jet expansion all accelerate. As the swirl intensity rises, these properties are, also enhanced.

In whirling flows, a severe and drastic transformation of the flow structure can occur, called vortex breakdown [98]. Harvey [147] conducted tests on turbulent flows inside a tube, and discovered that the breakdown was a transitional state between weakly swirling flows that do not exhibit flow reversals and rapidly swirling flows with columnar flow reversals by adjusting the swirl level. Knowledge of vortex breakdown can lead to improved overall efficiency of industrial machinery and its enhanced performance [19]. A such improvements increase low-level financial energy generation while reducing each greenhouse gas output, and hence may help mitigate the global climate change [20]. Peckham and Atkinson [**?**], Elle [100], and Lambourne and Bryer [101] carried out the earliest experimental studies on vortex breakdown.

Flow in an enclosed cylinder with a rotating top or bottom endwall can be interpreted in terms of vortex breakdown when stagnation points occur near the axis of rotation, resulting in one or more separation bubbles [148]. Escudier [67] enlarged Vogel's region for up to three vortex breakdowns and further characterised the region for unstable flows. Vogel [65] was the first to map the region of one vortex breakdown in flow in a cylindrical container with one rotating end wall in Reynolds number-aspect ratio space. The flow created in a cylinder with a revolving endwall was studied by Lugt and Abboud [149], who also explained how thermal gradients might affect the Boussinesq approximation. Computational analyses of rotating front wall problems by Lopez [63], Brown and Lopez [70], and Lopez and Perry [71] highlighted the mechanisms of vortex breakdown, periodic internal separation, and bubble coalescence. Tsitverblit later discovered that increasing the Reynolds number over the critical value for an aspect ratio $A = 2.5$ resulted in unstable flow. Yalagach and Salih [150] solved the three-dimensional Navier-Stokes equations for three aspect ratios ($A = 1.5, 2,$, and $2, 5$) and compared to axisymmetric solutions, which the flow fluctuations altering from axisymmetric to three-dimensional observed at higher Reynolds numbers.

The axisymmetric lattice Boltzmann revised approach is used in the present work to model incompressible rotating cavity flows, demonstrating the tool's capacity to anticipate the occurrence of a vortex breakdown. In addition, systematic simulations of vortex breakdown for $1002 < Re < 3061$ and $2 < A < 3.5$ were run, and the results compared to experimental data. An unsteady-periodic scenario (A=2.5, Re=2765) was also simulated with the highest axial velocity of the flow along the cylinder axis utilised to determine the flow periodicity.

7.2 Problem Definition and Solution

In this chapter, we use the axisymmetric lattice Boltzmann approach to investigate vortex breakdowns in swirling flows and flow in cylindrical containers with rotating endwalls. Figure 7.1 illustrates cylindrical cavity flow. Two non-dimensional parameters, the height-to-radius ratio (Aspect ratio) $A = \frac{H}{R}$ and the rotation Reynolds number $Re = \Omega\frac{R^2}{\nu}$ govern the flow behaviour in a cylindrical container, where Ω is the constant angular velocity, R is the radius, H is the height of the cylinder, and ν is the constant kinematic viscosity. The rotating endwall of a closed container functions as a pump, and the spiralling motion of the flow inside the cylinder increases the swirl velocity. As a result of this, the vortex breakdown phenomenon occurs. According to Brown and Lopez [70], who discussed the circumstances in which vortex breakdown takes place, the creation of negative azimuthal vorticity is a necessary component of vortex breakdown. The aspect ratio of the cylinder and the Reynolds number of flow both affect how many breakdown bubbles form. In the A-Re plane, the quantity of vortex breakdown bubbles was depicted on a map by Vogel [65]. Fig. 7.3 shows an extended version of the map produced by Escudier [67] for a variety of combinations of A and Re, covering steady and unsteady regimes and different numbers of breakdown bubbles. In the present work, the LBM results are compared to published experimental data and alternative numerical solutions. In numerical computations, all dimensional physical variables are given in the International System (SI) of units. All of the distribution functions in this simulation are set to their respective local equilibrium functions, $f_\alpha = f_\alpha^{eq}$ and $\bar{f}_\alpha = \bar{f}_\alpha^{eq}$, at the boundaries. In the simulations, $R = 1, \rho = 1,$

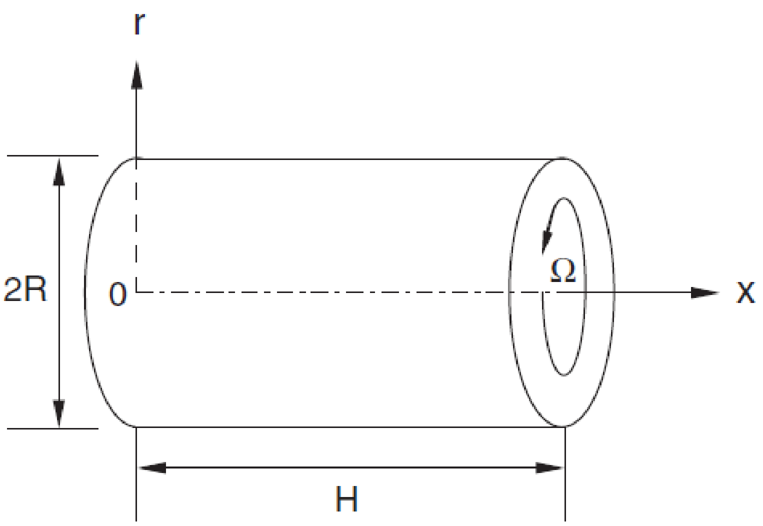

Figure 7.1: Schematic diagram of flow in a cylindrical container with a rotating endwall

and $\tau = 0.55$ are implemented and the boundary conditions(BC) are

$$\begin{cases} u_x = u_r = u_\phi = 0, & x = 0, \\ u_x = u_r = u_\phi = 0, & r = \pm R, \\ u_x = u_r = 0, u_\phi = r\Omega, & x = H. \end{cases} \tag{7.1}$$

As this is a complex flow involving vortex breakdown, different lattices in the r and x directions, i.e., 100 × 75, 150 × 112, 200 × 150, and 400 × 300, were used to establish solution independence from lattice size and convergence order. The findings are given in Fig. 7.2, revealing that if more than 150 × 112 lattices are utilised, solutions are independent of the choice of lattice number. Based on the findings, a lattice size of $\Delta x = 0.01$ that corresponds to 200 × 150 with $A = 1.5$ and $Re = 1290$ is expected to produce correct solutions and employed in all situations.

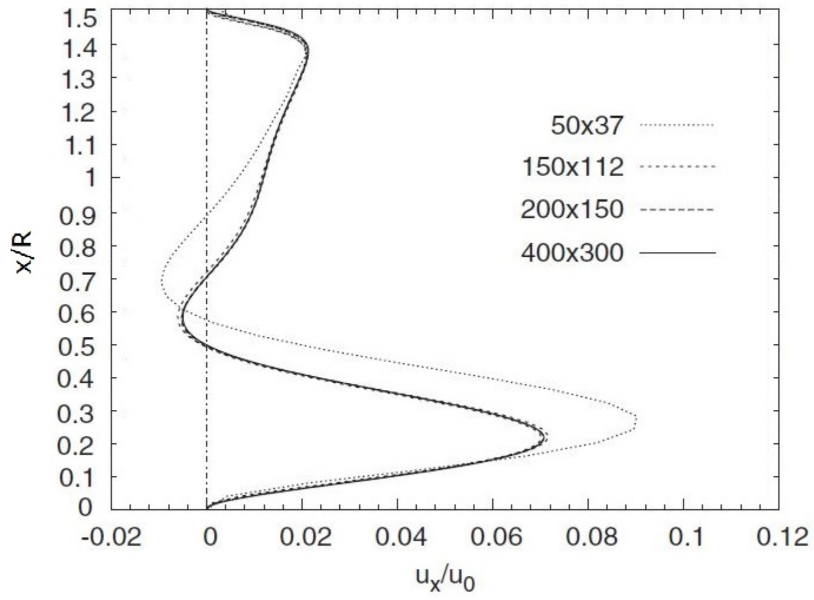

Figure 7.2: Lattice number effect on case with $A = 1.5$ and $Re = 1290$

7.3 Numerical Results

7.3.1 Steady Cylindrical Flows

Steady cylindrical flows with various aspect ratios and Reynolds numbers are considered in validating the updated axisymmetric lattice Boltzmann scheme. The flow pattern is examined in order to demonstrate the vortex breakdown phenomena. Furthermore, plots of the axial velocity components along the cylinder axis are created to determine the influence of Reynolds number changes on the minimum and maximum values of axial velocity components.

Steady flows for A=2, Re=1002, 1449, 1492 and 1854

The first set of simulations was performed for an aspect ratio of $A = 2$ and four distinct Reynolds numbers: $Re = 1002, 1449, 1492$, and 1854. The flow structure exhibits a basic pattern with no vortex breakdown for $Re = 1002$ and $A = 2$, as seen in Fig. 7.4.

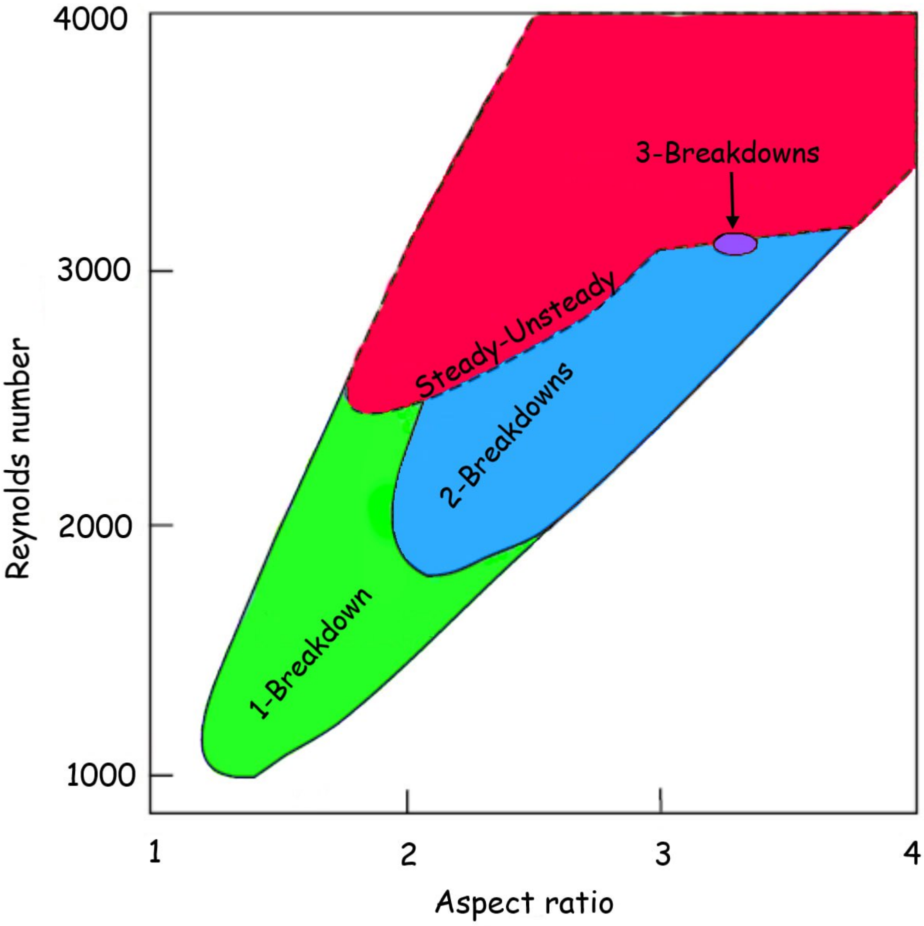

Figure 7.3: Stability boundaries for vortex breakdowns, as well as the border between unsteady and steady flow in the (A, Re) plane (Escudier, 1984).

Figure 7.3 shows that Vogel's stability limit confirms our simulation by proving the absence of a vortex breakdown. For this scenario, Bertela and Gori [151] observed a central viscous core that expands in size with distance from the revolving endwall. For ($Re = 1002$) in Fig.7.4 there is no vortex breakdown. The axial velocity profile for this case is shown in Fig.7.5. In Fig.7.6, an hour-glass structure is found in the streamlines for $Re = 1449$ and the axial velocity profile can be seen in Fig.7.7 . When the rotation rate is increased ($Re = 1449$), the form of the vortices changes, and there is a tiny difference in the recirculation zone near the wall with Re=1492 in Fig. 7.8. In both circumstances, however, there is a visible vortex breakdown. Fig.7.9 shows that the maximum axial velocity has been increased. For Re=1854, the initial bubble expands and a second bubble emerges independently. The second bubble is extremely small in

Fig. 7.10 because it is near to the limit of one-breakdown and two-breakdown areas inside the stability diagram (Fig. 7.3). Furthermore, investigating the axial velocity along the cylinder axis reveals that as *Re* increases, the minimum and maximum axial velocities along the cylinder axis decrease for fixed aspect ratio $A = 2$ (Figs. 7.5, 7.7, 7.9 and 7.11) but the vortex breakdown patterns remain axisymmetric with respect to the cylinder axis.

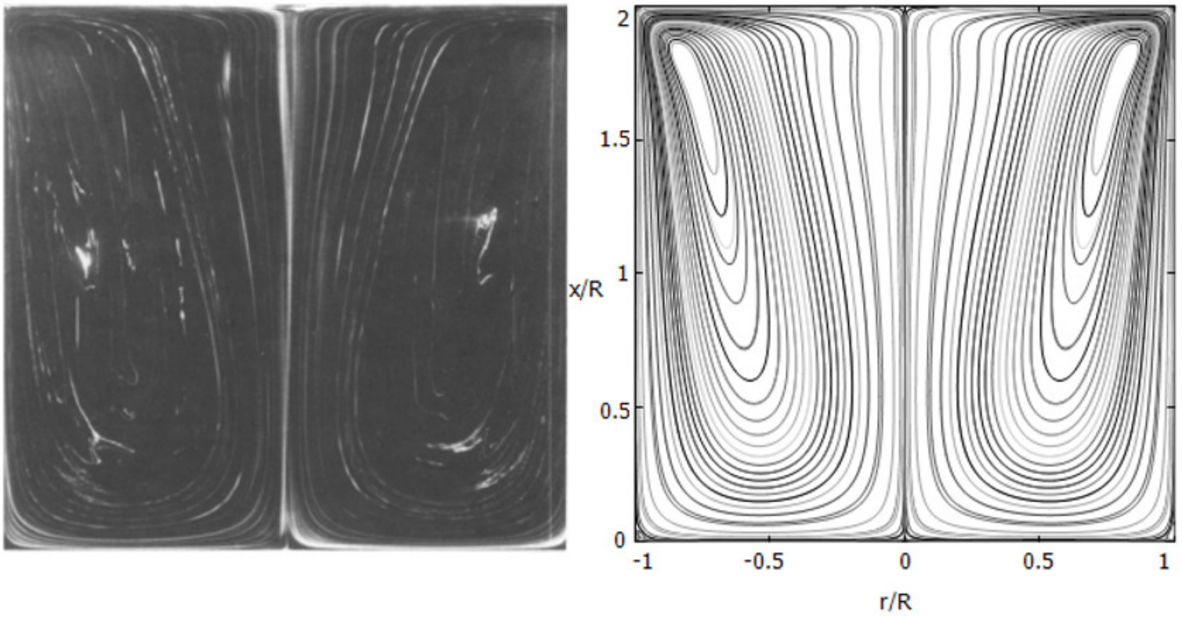

Figure 7.4: Comparison between computed streamlines and experimental flow visualisation (Escudier, 1984) of steady, axisymmetric flow in a cylindrical container, A=2, Re=1002

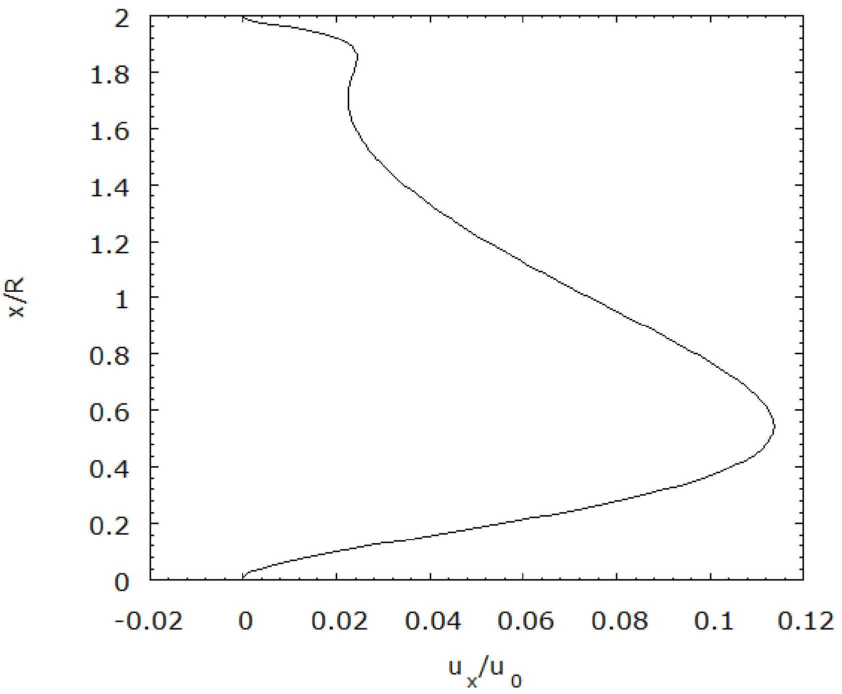

Figure 7.5: Axial velocity profile along the cylinder axis for A=2, Re=1002

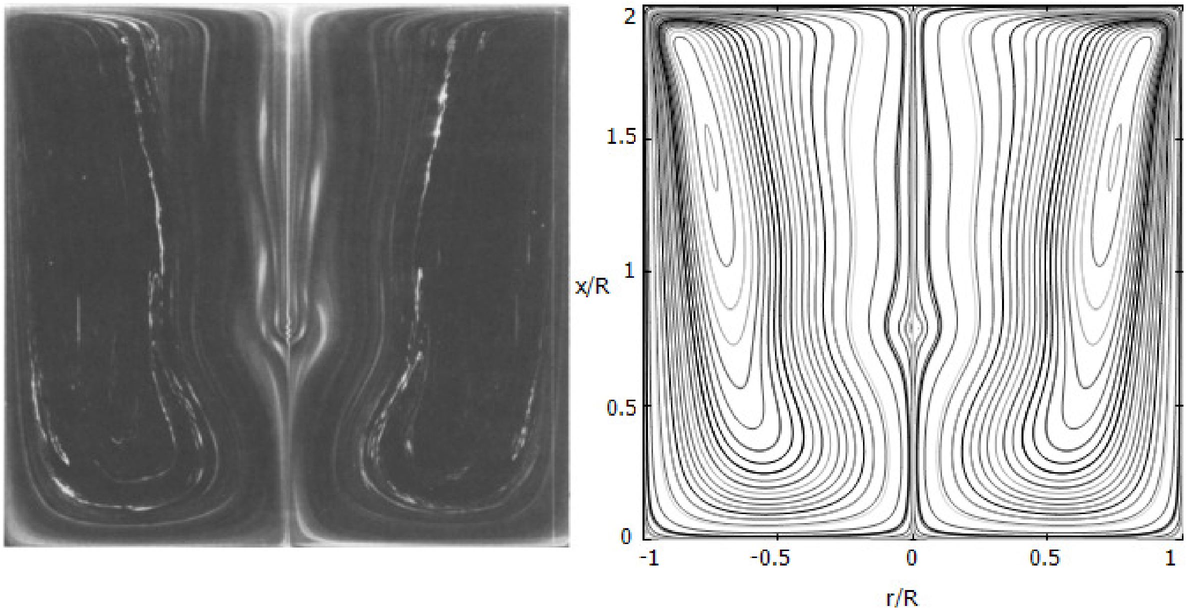

Figure 7.6: Comparison between computed streamlines and experimental flow visualisation (Escudier, 1984) of steady, axisymmetric flow in a cylindrical container for A=2, Re=1449

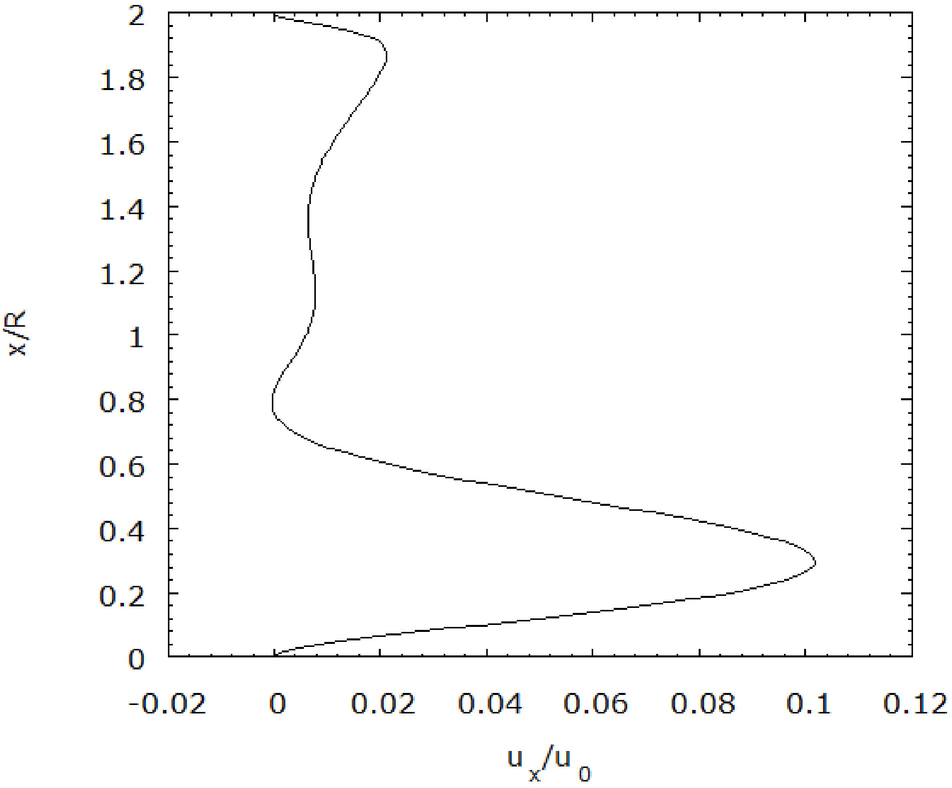

Figure 7.7: Axial velocity profile along the cylinder axis for A=2, Re=1449

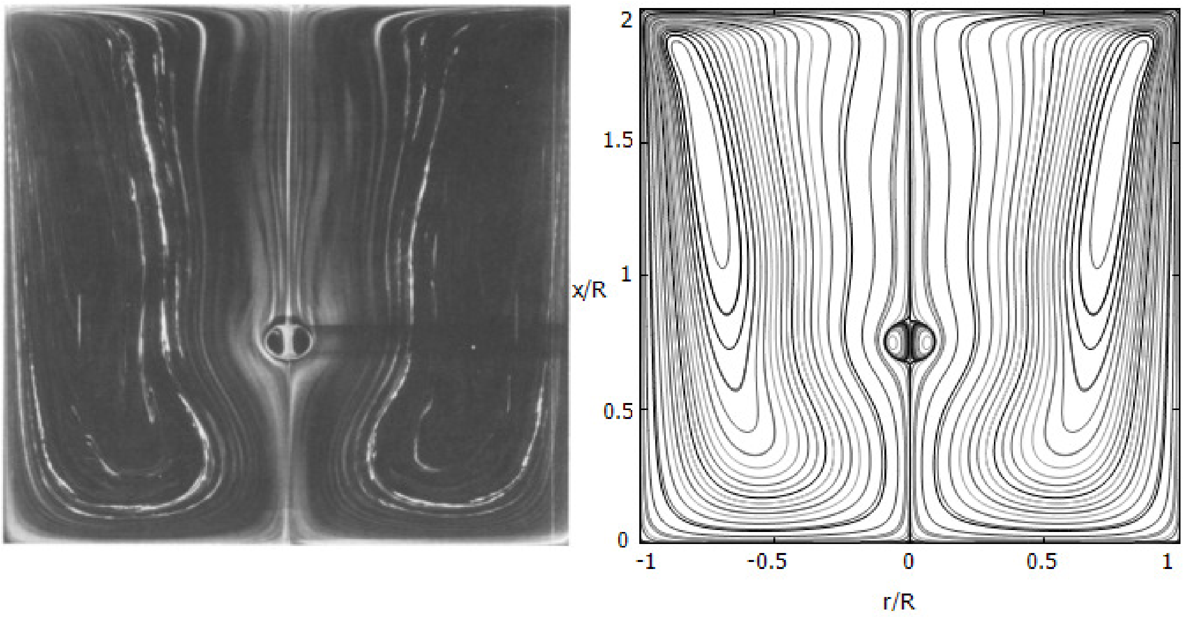

Figure 7.8: Comparison between computed streamlines and experimental flow visualisation (Escudier, 1984) of steady, axisymmetric flow in a cylindrical container for A=2, Re=1492

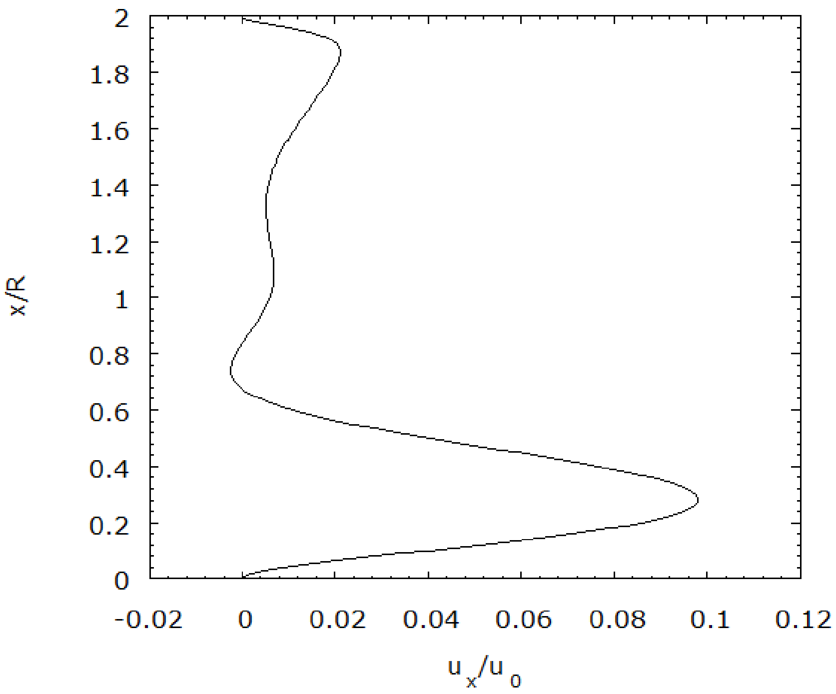

Figure 7.9: Axial velocity profile along the cylinder axis for A=2, Re=1492

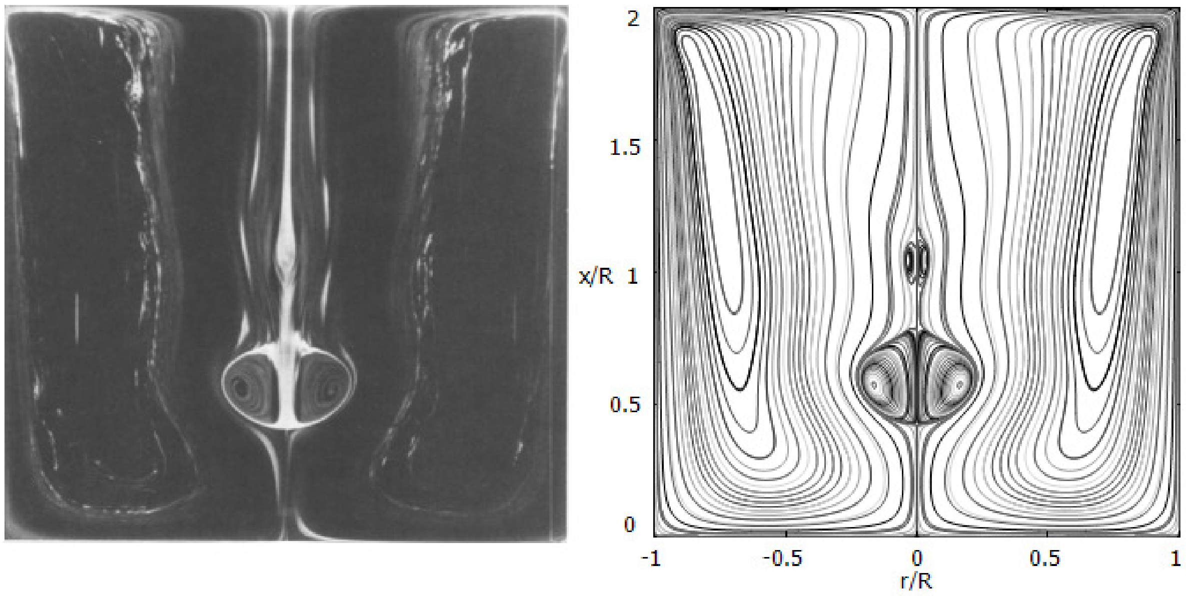

Figure 7.10: Comparison between computed streamlines and experimental flow visualisation (Escudier, 1984) of steady, axisymmetric flow in a cylindrical container for A=2, Re=1854

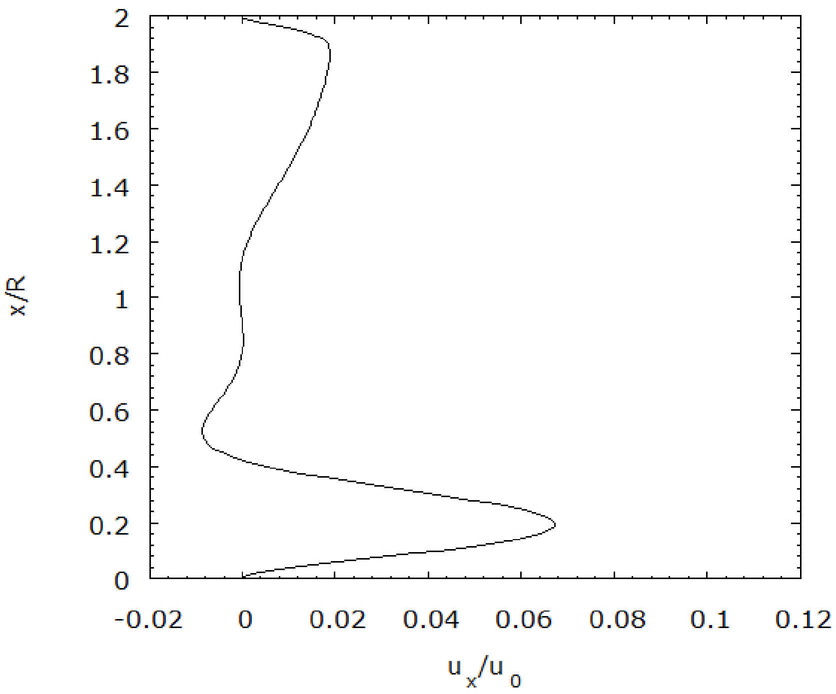

Figure 7.11: Axial velocity profile along the cylinder axis for A=2, Re=1854

Steady flows for A=2.5, Re=2126 and 2494

A second set of simulations was undertaken for A=2.5 and Re=2126 and Re=2494. Figs. 7.12 and 7.14 show the flow patterns and the fluctuation of the axial velocity components along the cylinder axis. There is just one stagnation point with two unique recirculation zones in both situations because the downstream stagnation point emerges first and moves upstream. As observed in Fig. 7.12, two entirely distinct bubbles develop for Re=2126. However, for Re=2494, downstream vortex breakdown initially manifests, and the subsequent vortex breakdown zone is fed by the low magnitude interior velocity field. As a consequence, a single bubble with two distinct vortex breakdown zones is created by merging two vortex breakdowns (Fig. 7.14). By comparing the minimum and maximum axial velocities along the cylinder axis in Figs. 7.13 and 7.15, it is found that as the Reynolds numbers rise, both the minimum and maximum axial speeds drop. Additionally, for the examples mentioned above, the symmetry of vortex breakdown with respect to the cylinder axis is evident and is consistent with Escudier's findings [67].

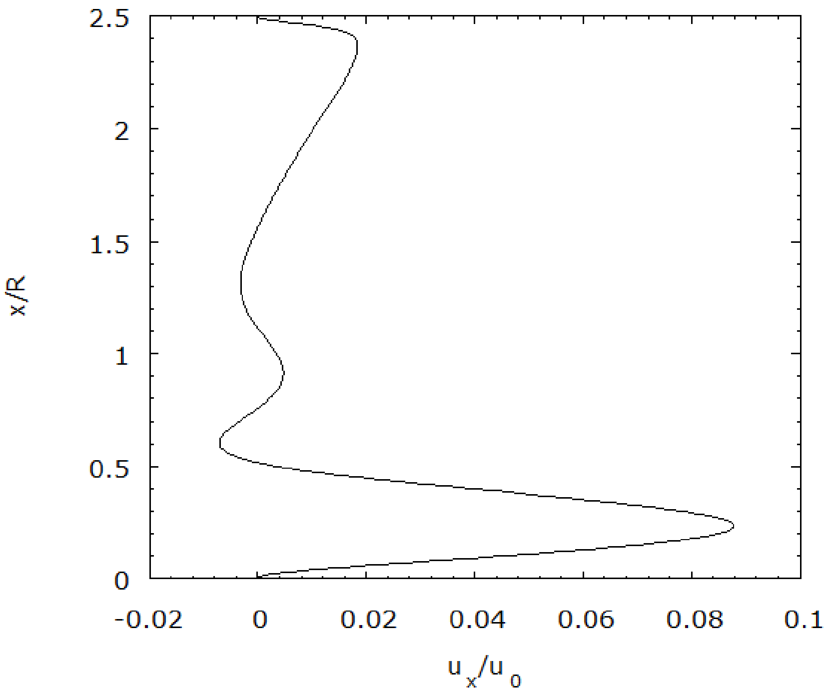

Figure 7.13: Axial velocity profile along the cylinder axis for A=2.5, Re=2126

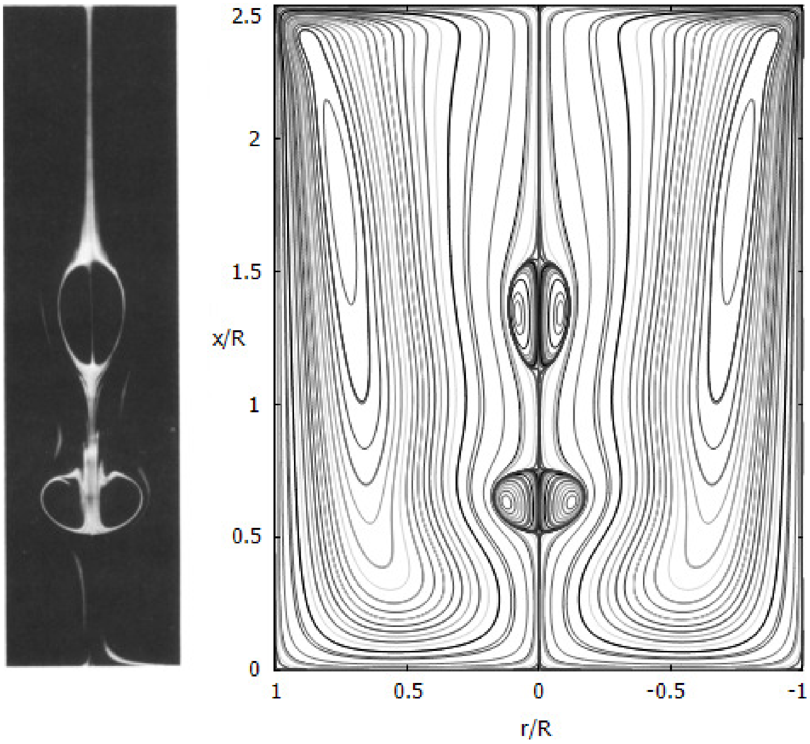

Figure 7.12: Comparison between computed streamlines and experimental flow visualisation (Escudier, 1984) of steady, axisymmetric flow produced in a cylindrical container for A=2.5, Re=2126

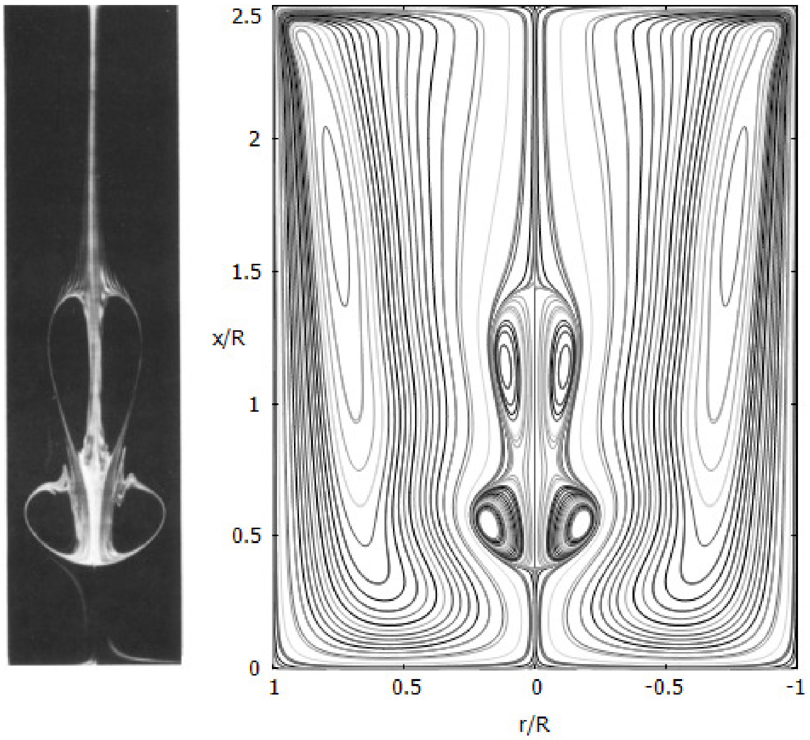

Figure 7.14: Comparison between computed streamlines and experimental flow visualisation (Escudier, 1984) of steady, axisymmetric flow produced in a cylindrical container for A=2.5, Re=2494

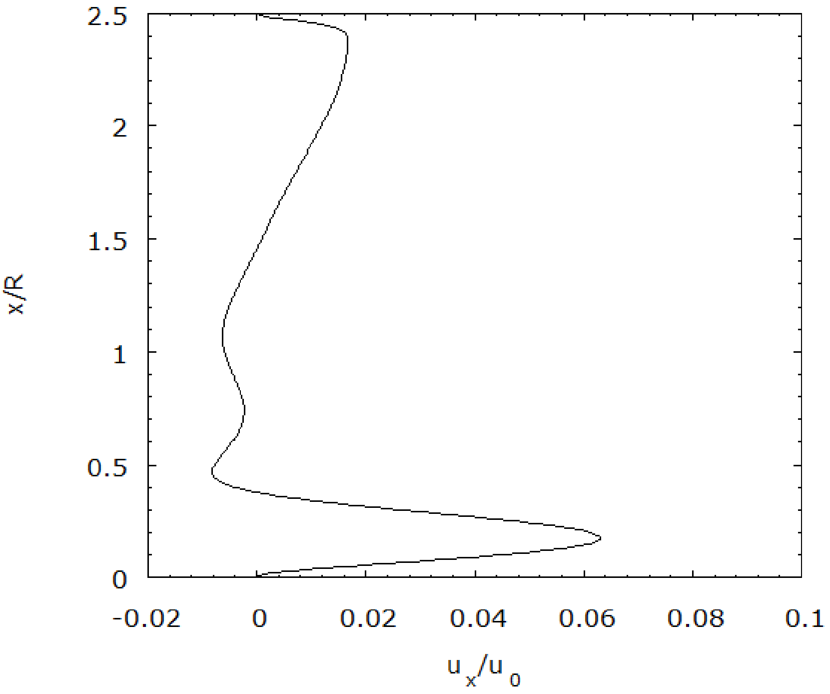

Figure 7.15: Axial velocity profile along the cylinder axis for A=2.5, Re=2494

Steady flows for *A*=3.25, *Re*=2752, 2819 and 2947

Three different spatial Reynolds numbers, Re = 2752, 2819, and 2947, are considered in the third set of simulations. Figs. 7.16 to 7.21, show the results. Here, three vortex breaks are seen. Once more, the downstream vortex breakdown emerges first, followed by two upstream vortex breakdowns that have higher axial length but smaller diameter than the first vortex breakdown. The two vortex breakdowns in the upstream region combine to form a single bubble with two distinct vortex breakdowns but remain independent of the downstream vortex breakdown. The two upstream vortexes may be observed to mix more as the Reynolds number rises. Additionally, it is discovered that, in contrast to other cases, the lowest and maximum axial velocities along the cylinder axis rise as the rotation rate increases as shown in Figs. 7.17, 7.19, 7.21. For this collection of simulations, the symmetry of vortex breakdown is once again plainly discernible.

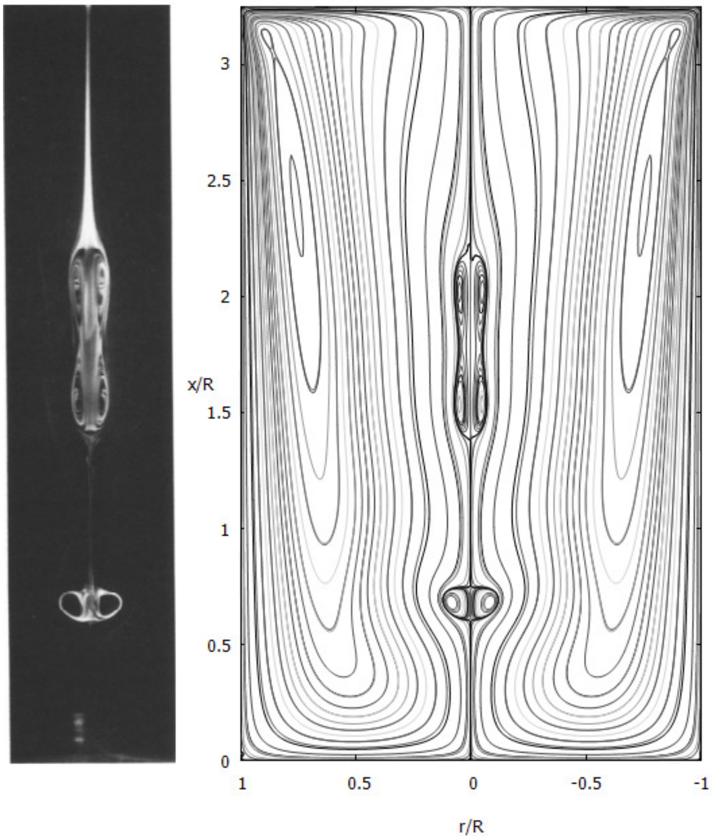

Figure 7.16: Comparison between computed streamlines and experimental flow visualisation (Escudier, 1984) of steady, axisymmetric flow produced in a cylindrical container for A=3.25, Re=2752

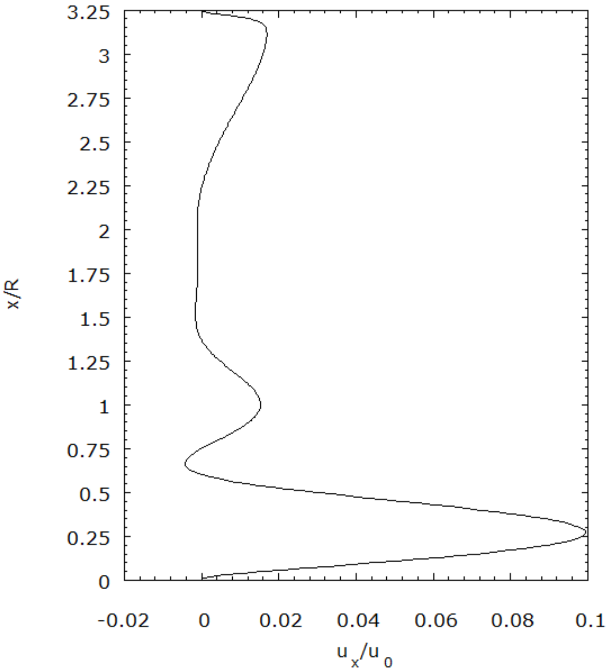

Figure 7.17: Axial velocity profile along the cylinder axis for A=3.25, Re=2752

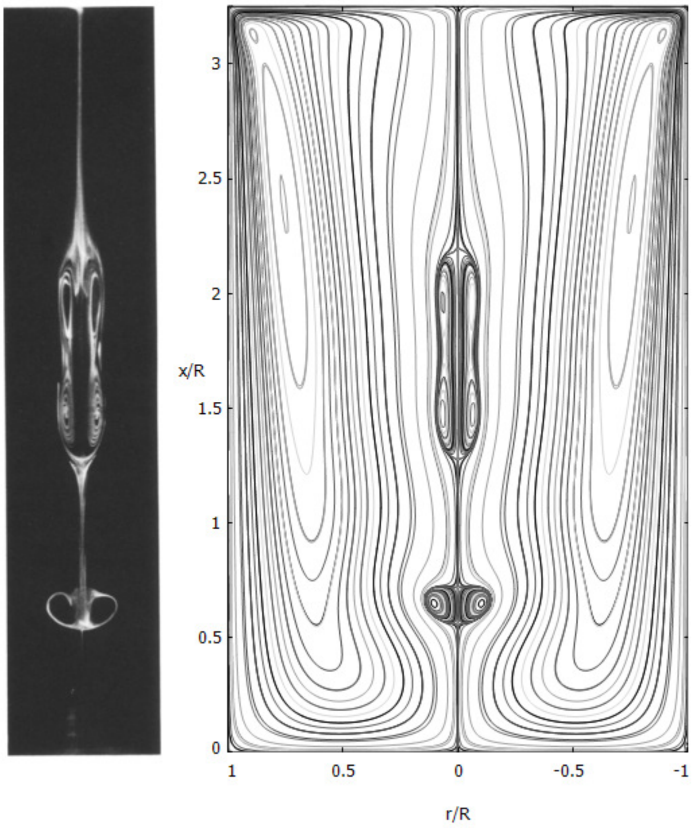

Figure 7.18: Comparison between computed streamlines and experimental flow visualisation (Escudier, 1984) of steady, axisymmetric flow produced in a cylindrical container for A=3.25, Re=2819

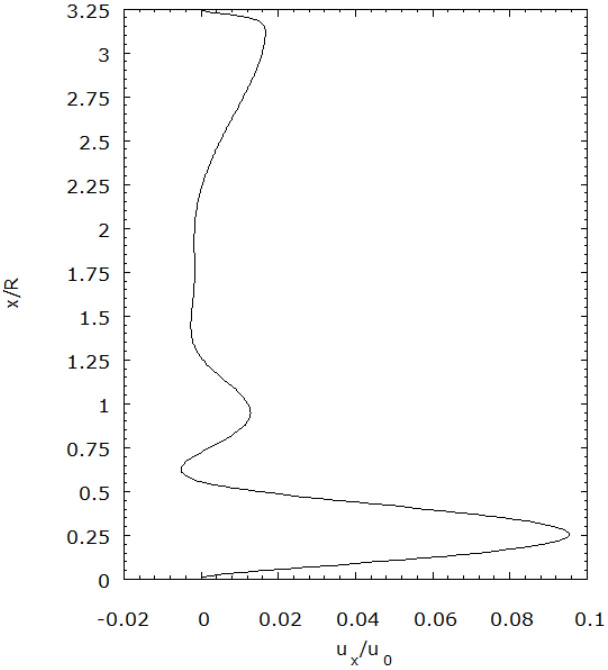

Figure 7.19: Axial velocity profile along the cylinder axis for A=3.25, Re=2819

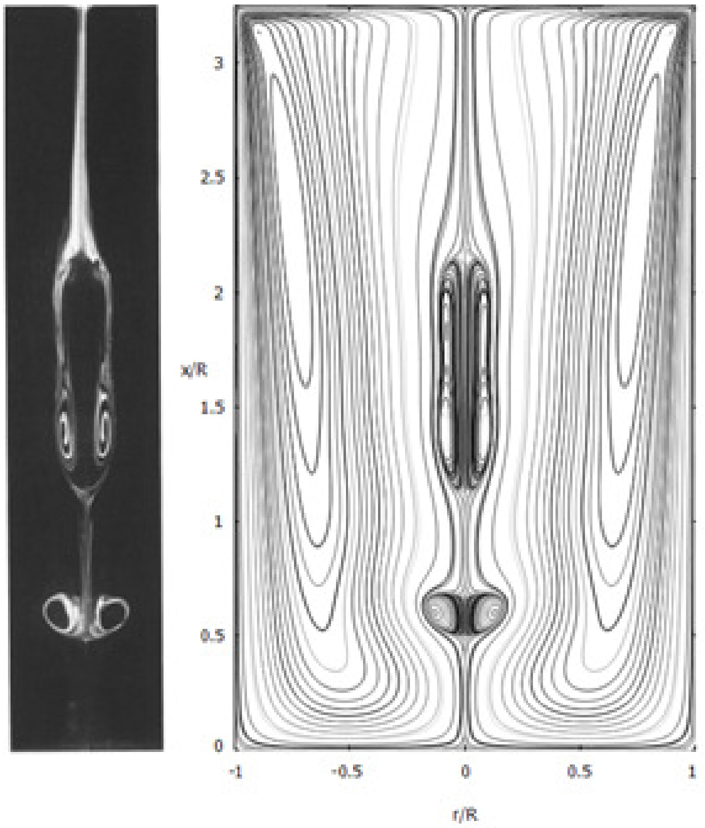

Figure 7.20: Comparison between computed streamlines and experimental flow visualisation (Escudier, 1984) of steady, axisymmetric flow produced in a cylindrical container for A=3.25, Re=2947

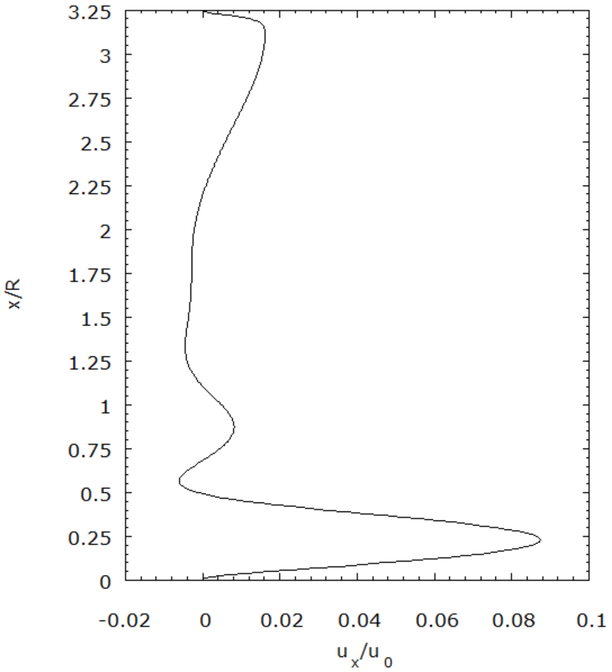

Figure 7.21: Axial velocity profile along the cylinder axis for A=3.25, Re=2947

Steady flows for A=3.5, Re=3023, 3042 and 3061

For the final set, three examples with Re=3023, 3042, and 3061 are simulated at the largest A=3.5, and three distinct vortex breakdown zones with a well-defined internal structure are seen in Figs. 7.22, 7.24, and 7.26. Whereas the centre vortex breakdown never combines with the upstream vortex breakdown, the downstream vortex breakdown initially occurs and extends away from the axis in a circular manner. The axial length and width of the central vortex breakdown grow as the Reynolds number increase. Between the two downstream vortexes and the two upstream vortexes, a single bubble was created. Additionally, it can be shown that the minimum and maximum axial velocity along the cylinder axis reduce as the Reynolds number increase as evident in Figs. 7.23, 7.25 and 7.27. Once more, the flow pattern and experimental observations are in excellent agreement, and the symmetry of the vortex pattern is clearly evident.

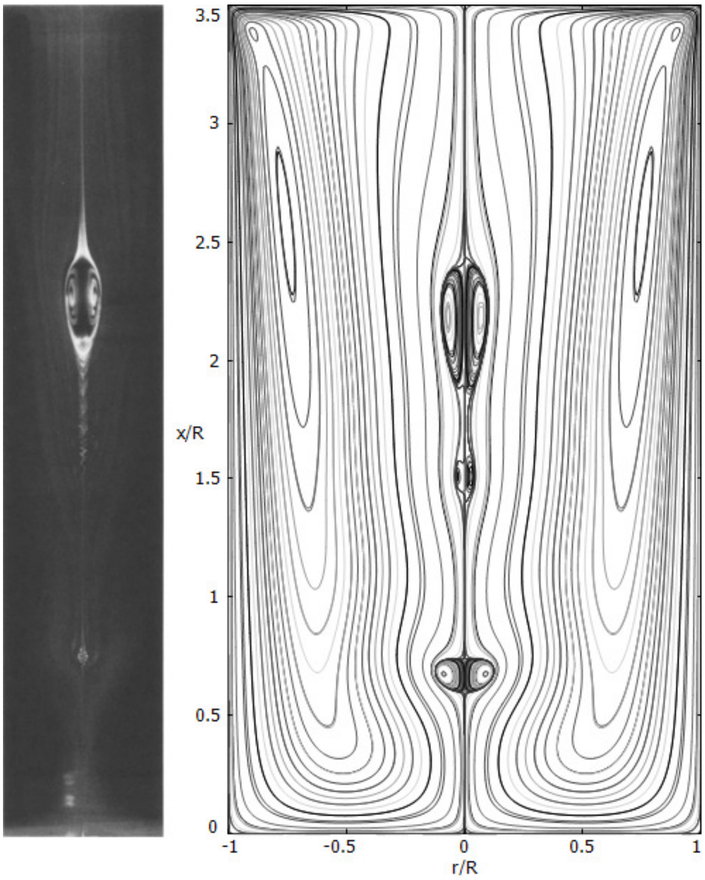

Figure 7.22: Comparison between computed streamlines and experimental flow visualisation (Escudier, 1984) of steady, axisymmetric flow produced in a cylindrical container for A=3.5, Re=3023

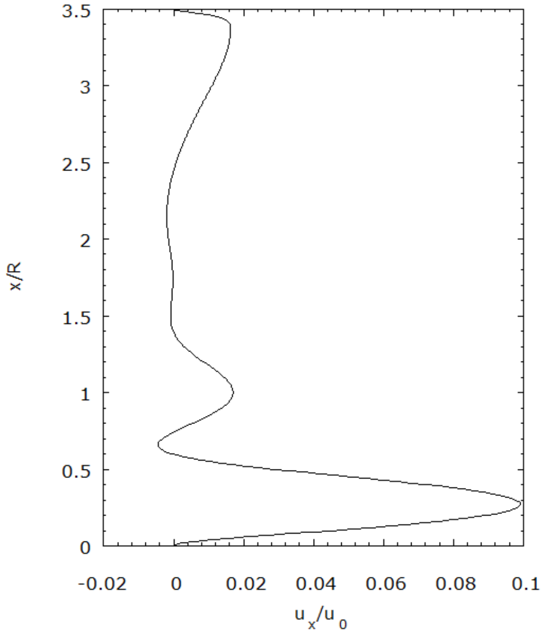

Figure 7.23: Axial velocity profile along the cylinder axis for A=3.5, Re=3023

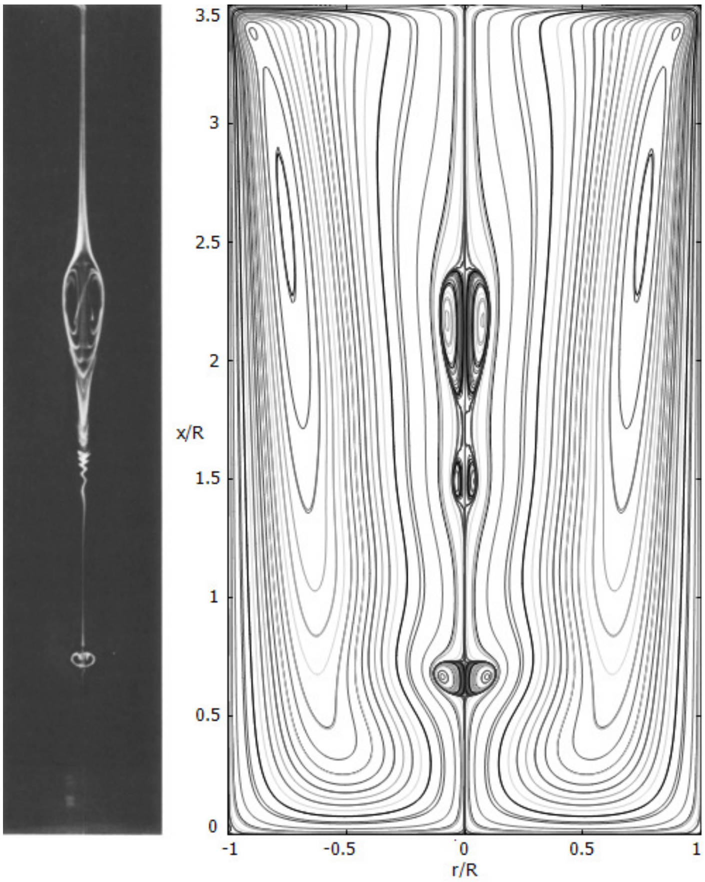

Figure 7.24: Comparison between computed streamlines and experimental flow visualisation (Escudier, 1984) of steady, axisymmetric flow produced in a cylindrical container for A=3.5, Re=3042

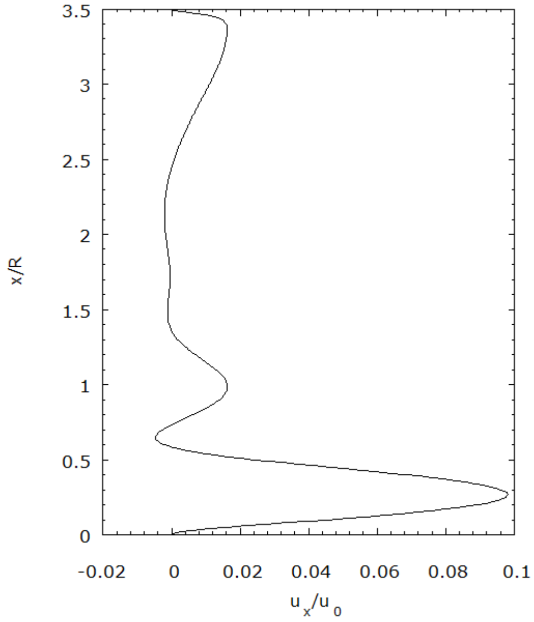

Figure 7.25: Axial velocity profile along the cylinder axis for A=3.5, Re=3042

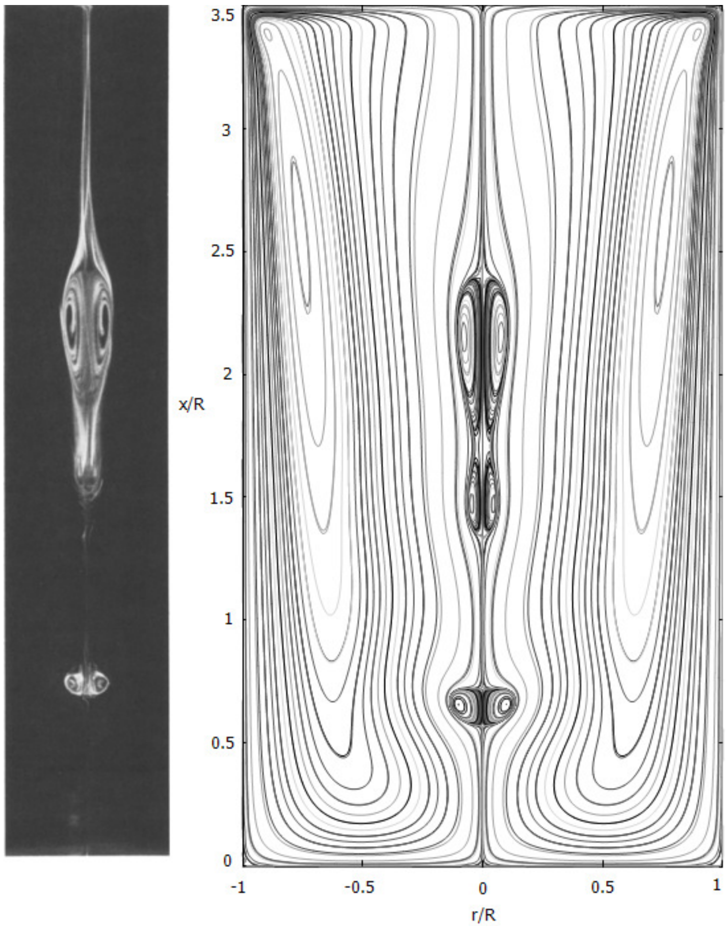

Figure 7.26: Comparison between computed streamlines and experimental flow visualisation (Escudier, 1984) of steady, axisymmetric flow produced in a cylindrical container for A=3.5, Re=3061

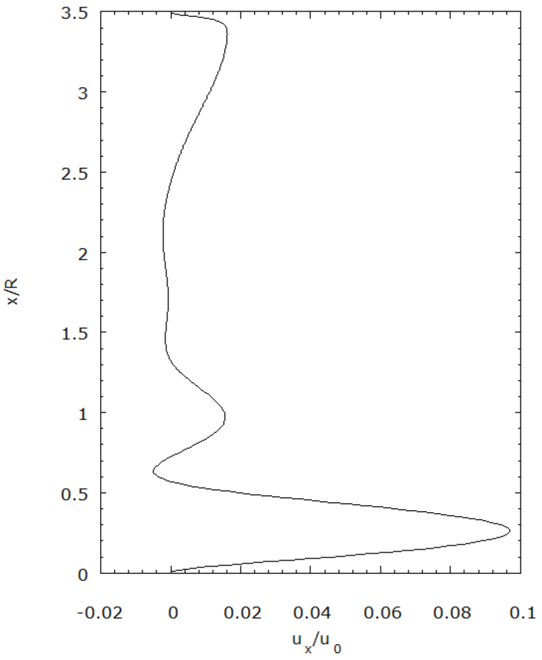

Figure 7.27: Axial velocity profile along the cylinder axis for A=3.5, Re=3061

In two case studies (A, Re) = (2.5, 2126) and (A, Re) = (3.25, 2752) the predicted location of stagnation points are compared with those obtained experimental and by the alternative numerical scheme. The results listed in Tables 9.1 and 8.2 indicate good agreement.

Table 7.1: Locations of stagnation points for (A, Re) = (2.5, 2126). (UB: upper bubble, LB: lower bubble.)

	Above UB	Below UB	Above LB	Below LB
Present	X=1.955	X=1.695	X=1.325	X=0.925
Experiment [67]	X=2	X=1.76	X=1.37	X=0.95
Yamada and Suzuki[152]	X=1.98	X=1.75	X=1.36	X=0.95

Table 7.2: Locations of stagnation points for (A, Re) = (3.25, 2752). (UB: upper bubble, LB: lower bubble.)

	Above UB	Below UB	Above LB	Below LB
Present	X=2.625	X=2.575	X=1.898	X=1.085
Experiment [67]	X=2.65	X=2.51	X=1.84	X=1.04
Yamada and Suzuki[152]	X=2.64	X=2.49	X=1.83	X=1.05

7.3.2 An Unsteady-Periodic Flow

This section identifies the period of the specific unsteady-periodic flow for Re=2765 and A=2.5. The flow behaviour is examined in terms of frequency of vortex breakdown and the position of stagnation points. To the author's best knowledge, this work provides the first numerical analysis of the peresent flow configuration. The axial velocity profile of this flow along the cylinder axis is analysed and the maximum axial velocity chosen to calculate the absolute error and relative error between two flow patterns at two different time steps ($t_1 and t_2$). This is key to finding out the period when the unique flow pattern appears again. Knowing the flow periodicity allows us to predict and control the behaviour of this flow.

Figs. 7.28 to 7.30 display the findings from the examination of three distinct cases are displayed where the estimated duration is around 350.2 seconds ($19k$ time steps). This period, however, can occasionally be larger or shorter than $350.2s$ because of numerical inaccuracy. For the first scenario, the time period between $9511.6s$ and $9548.5s$ is chosen, and the axial velocity profile of this flow along the cylinder axis are compared. Letting the maximum velocity for u_x be used to calculate the absolute error between $t_1 = 9176.1s$ and $t_2 = 9526.3s$ in Fig. 7.28, the absolute error calculated using $E_r = \mid u_{t_1,max} - u_{t_2,max} \mid$ is 0.00019 and the relative error calculated using $\mid \frac{u_{t_1,max} - u_{t_2,max}}{u_{t_1,max}} \mid$ is 0.04.

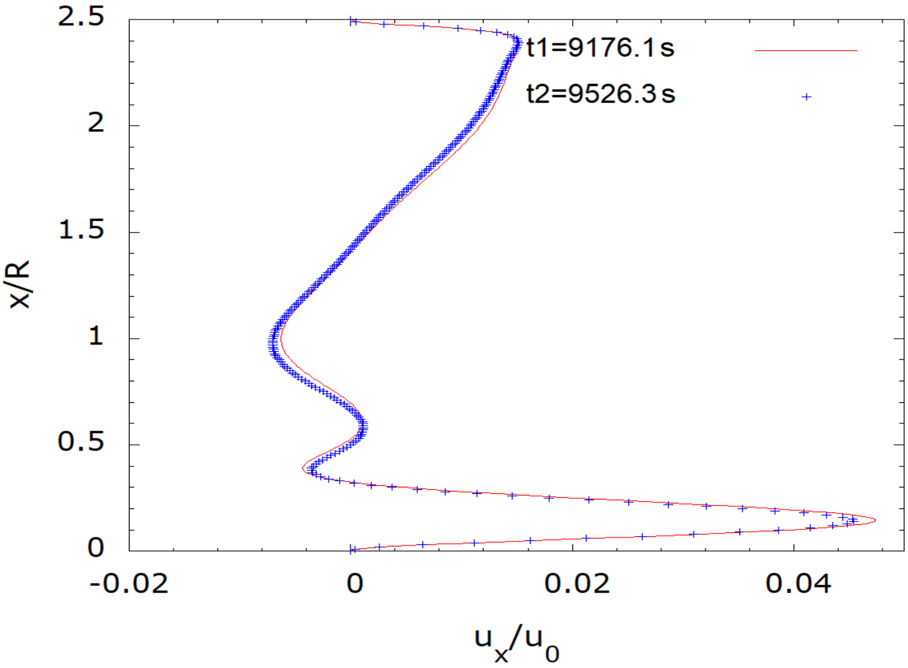

Figure 7.28: Comparison between axial velocity profiles along the cylinder axis at two time instants, $t_1 = 9176.1s$ and $t_2 = 9526.3s$

In the second instance, the time range between $14372.5s$ and $14403.8s$ is examined, and the findings are compared against the outcome at $t = 14746.6s$. The absolute error between the profiles at $t_1 = 14396.4s$ and $t_2 = 14746.6s$, shown in Fig. 7.29, is 0.00003, and the relative error is 0.006. The results of the last examination, which took place at times $t_1 = 20267.4s$ and $t_2 = 20617.6s$, are displayed in Fig. 7.30. The relative error is 0.02, and the absolute error is 0.00012.

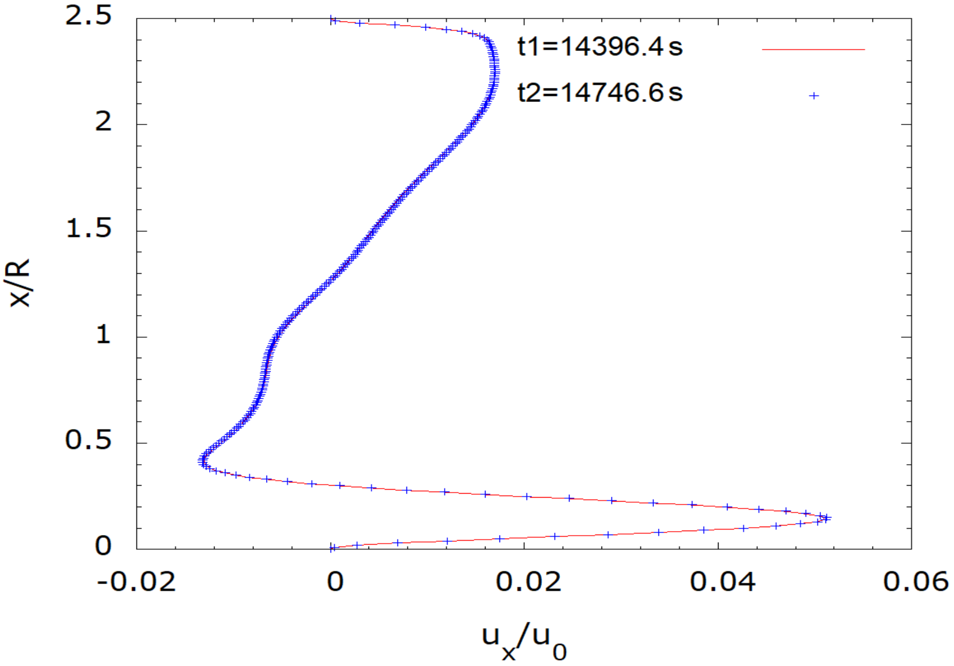

Figure 7.29: Comparison between axial velocity profile along the cylinder axis at two time instants$t_1 = 14396.4s$ and $t_2 = 14746.6s$

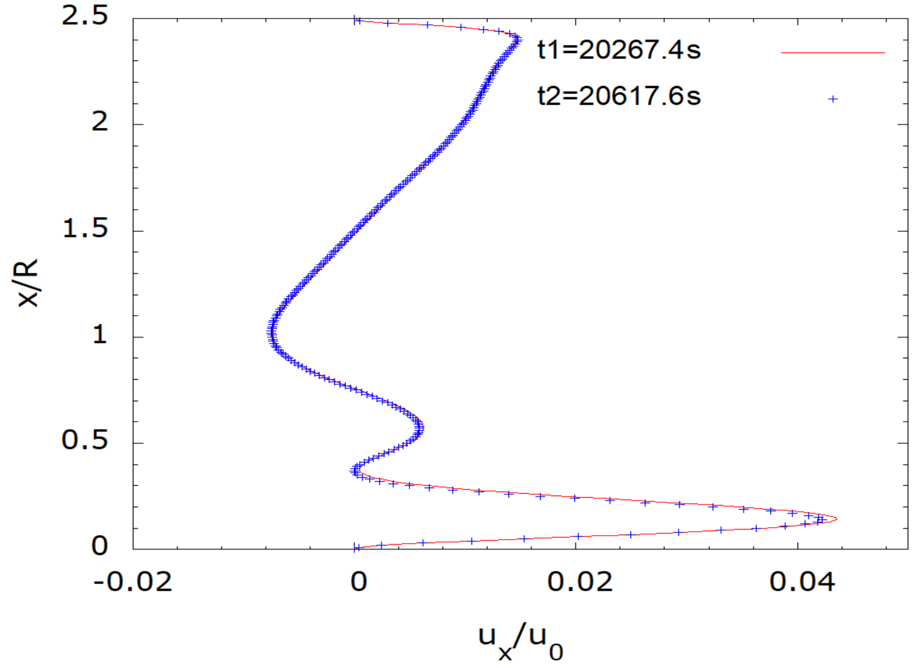

Figure 7.30: Comparison between axial velocity profile along the cylinder axis at two time instants $t_1 = 20267.4s$ and $t_2 = 20617.6s$

The results indicate that, over a sufficient length of time, the first bubble manifests with a clearly defined vortex breakdown. There are two stagnation points; the higher at

$x = 1.34$ and the lower at $x = 0.29$. The second vortex breakdown then begins to emerge in the same bubble as it grows in size along the axis of the cylinder, evolving until there are two distinct bubbles with four stagnation points. For the upstream vortex breakdown, the top stagnation point is at $x = 1.40$, whereas the lower stagnation point is at $x = 0.65$. Additionally, the downstream vortex breakdown has an upper stagnation point at $x = 0.45$, whereas the lower stagnation point is at $x = 0.31$. Then the upstream and downstream bubbles begin to collide, creating a single bubble with two vortex breakdowns before reducing to just one breakdown as before. This process takes 350.2s.

7.4 Conclusion

To show the potential of the approach for forecasting intricate vortex breakdowns, the revised axisymmetric lattice Boltzmann method has been applied to rotating axisymmetric flows. To validate the precision and effectiveness of the procedure, the findings of the current study were compared to the research by Escudier and the stability limitations determined by Vogel. In the end, the strategy has provided new knowledge of the behaviour of the axial velocity component along a cylinder axis. The numerical tests have demonstrated that the flow pattern in each case is consistent with that seen during experimental research. Throughout all simulations, the locations of the stability limits determined by Vogel [65] correspond strongly with the total number of vortex breaks. Escudier and Keller [153]'s assertion that a vortex breakdown is fundamentally axisymmetric is supported by the fact that the symmetry of vortex breakdown along a cylinder axis is readily apparent regardless of whether the rotation rate is lowered or increased. The strength of the method suggested here, relies upon the realisation that it is unnecessary to compute velocity gradients. This reduces the amount of processing required and simplifies and streamlines the simulation process. It has been demonstrated that exact solutions in complex cylindrical cavity flows may be obtained by employing local equilibrium distribution functions as boundary conditions.

It has been demonstrated how the outstanding characteristics of the revised scheme may result in changes in the minimum and maximum axial velocity components as the rotation speed increases. We can determine the period using the capacity of this scheme to model unsteady-periodic flows. This aids in the prediction and management of flow behaviour and could have engineering impact through improving the efficiency and productivity of industrial machinery.

Chapter 8

2^{nd} order bounce-back method for AxLAB®

8.1 Steady Flow inside a cylindrical cavity with rotating endwalls

The second-order bounce-back scheme improves the accuracy and efficiency of the revised axisymmetric lattice Boltzmann method when applied to problems incorporating solid wall boundaries. This enhanced technique benefits any arbitrary geometry with a non-slip boundary condition. The bounce-back approach involves particles travelling toward a solid wall and reflecting into the fluid zone in the opposite direction while maintaining their velocity. This method is second-order accurate. In this chapter, steady flow inside a cylindrical cavity with rotating is validated for the second-order axisymmetric lattice Boltzmann revised scheme. The maximum value of the axial velocity component, the position of its occurrence, and the location of stagnation points are investigated and the results compared with published experimental data [77], and alternative numerical predictions by the numerical GITT method [154], the 3D lattice Boltzmann method (LBM) and the finite volume method solution of the Navier-Stokes equations [155]. Comparison of the relative errors between the 2nd order AxLAB® and the original AxLAB® [2] demonstrates the considerable improvements of the new scheme. Furthermore, the new technique delivers additional information and more accurate results with lower error, generating a more symmetrical and detailed flow pattern.

8.1.1 Problem description

The flow problem is illustrated in Fig. 8.1 and is known to have varied complicated topologies depending on the aspect ratio $A = \frac{H}{R}$ and Reynolds number $Re = \Omega\frac{R^2}{\nu}$ [2], where Ω is the constant angular velocity of the base (Ω_b) or top (Ω_u) walls, R is the radius of the cylinder, H is the height of the cylinder, and ν is the fluid kinematic viscosity. In a closed container, the rotating endwalls act as a pump, and the spiralling motion of the flow inside the cylinder increases the swirl velocity. This can result in vortex breakdown. Different cases with parameters of (A, Re) are used to validate the improved Axisymmetric Lattice Boltzmann Method. In the simulations, $R = 1, \rho = 1$ and $\tau = 0.55$. The boundary conditions (BC) are

$$\begin{cases} u_x = u_r = 0, u_\phi = r\Omega_b, & x = 0, \\ u_x = u_r = u_\phi = 0, & r = R, \\ u_x = u_r = 0, u_\phi = r\Omega_u, & x = H. \end{cases} \tag{8.1}$$

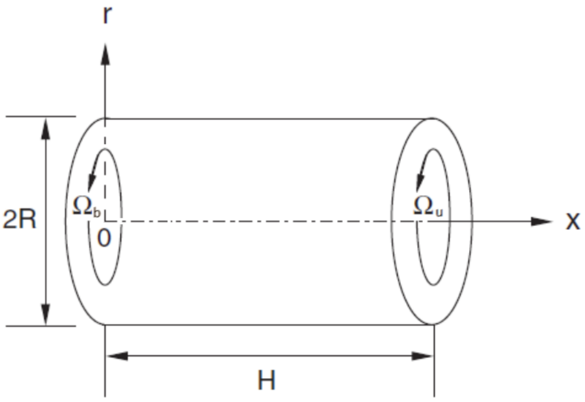

Figure 8.1: Schematic diagram of flow in a cylindrical container with rotating endwalls

8.2 Numerical results

8.2.1 Flow in a cylindrical container with two rotating endwalls

The first set of simulations was carried out for four different Reynolds numbers and aspect ratios as follows: (A, Re) = (3,300), (2,500), (3,750) and (4,1200). Fig. 8.2 shows the flow regime for (A, Re) = (3,300) for numerical results extracted from the work of Sørensen et al. [156] and predicted by the present 2nd order AxLAB® method. The flow has a simple structure and vortex breakdown does not occur. The results for (2,500), (3,750) and (4,1200) are shown in Figs. 8.3, 8.4 and 8.5 respectively. The results show cases in which re-circulating bubbles are generated and the vortex breakdown patterns are axisymmetric with respect to the cylinder axis. There is excellent agreement between the 2nd order AxLAB® and other work in each case. The present improved scheme produces further details of the fluid behaviour inside the vortices, the location of the stagnation points, and the length of the vortices.

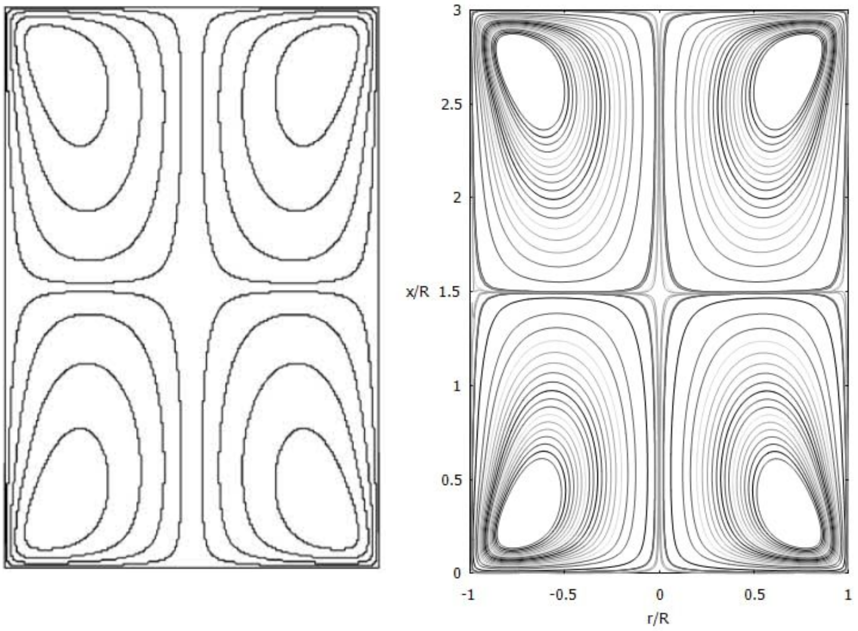

(a) (b)

Figure 8.2: Steady flow in a cylindrical container with two co-rotating end plates for for$A$=3, Re=300: (a) stream surface contours (Sørensen et al., 2005); and (b) computed streamlines.

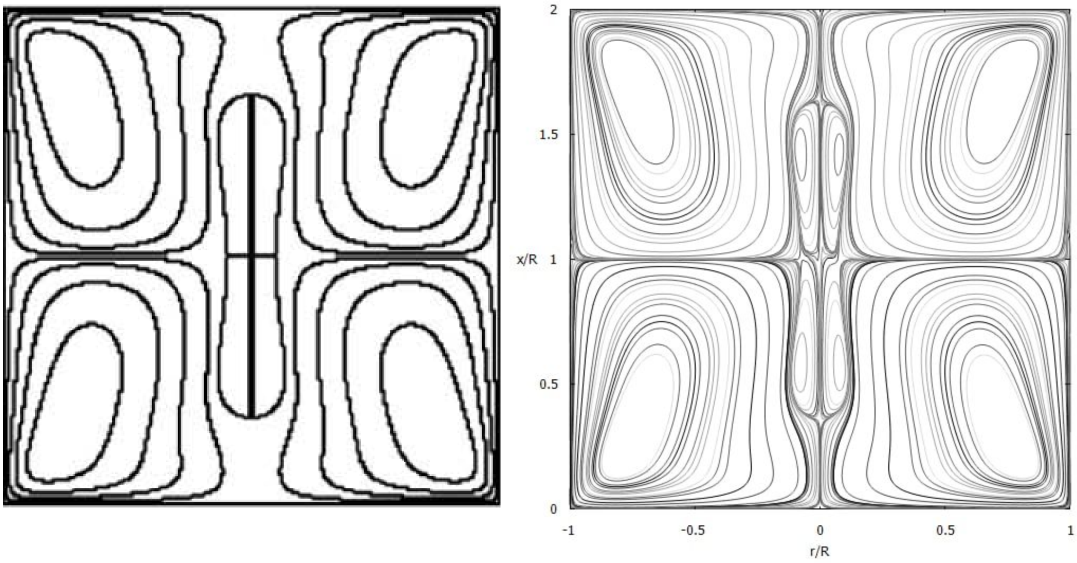

(a) (b)

Figure 8.3: Steady flow in a cylindrical container with two co-rotating end plates for A=2, Re=500: (a) stream surface contours (Sørensen et al., 2005); and (b) computed streamlines.

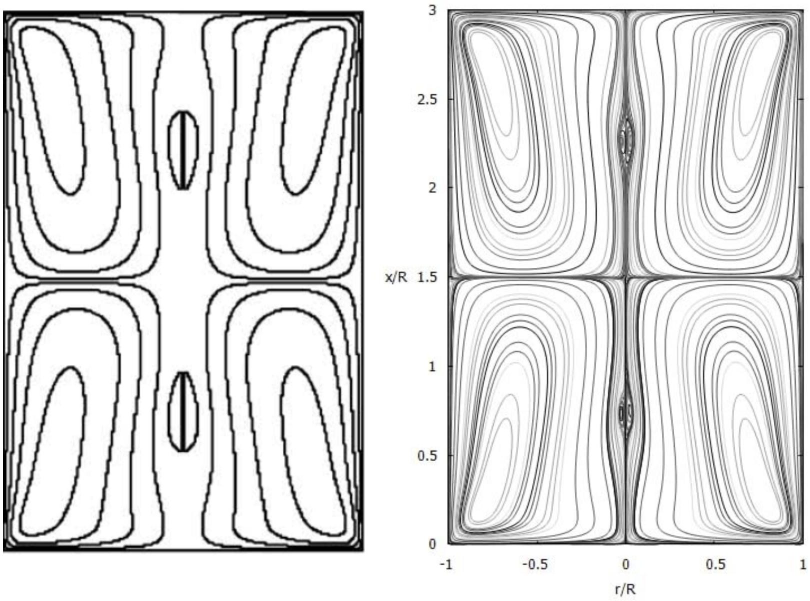

(a) (b)

Figure 8.4: Steady flow in a cylindrical container with two co-rotating end plates for A=3, Re=750: (a) stream surface contours (Sørensen et al., 2005); and (b) computed streamlines.

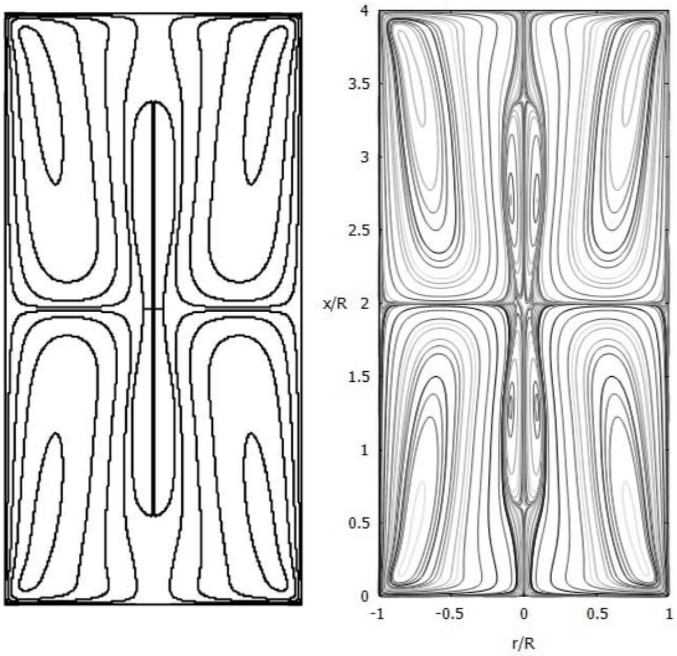

(a) (b)

Figure 8.5: Steady flow in a cylindrical container with two co-rotating end plates for A=4, Re=1200: (a) stream surface contours (Sørensen et al., 2005); and (b) computed streamlines.

8.2.2 Steady flows in a cylindrical container with one rotating (top) endwall

In this section, $\Omega_b = 0$ is chosen, indicating that the bottom endwall is stationary while the top endwall rotates. Figs. 8.6 to 8.8 show the produced flow pattern in an enclosed cylindrical container with a rotating endwall for (A, Re) = (1.5,1290), (3.25,2819), and (3.5,3061) respectively. The flow pattern seen in Fig. 8.6 is characterised by a single vortex breakdown. As a consequence, the expected findings from the current simulation are compatible with the numerical results obtained by GITT simulation [154], Bhaumik and Lakshmisha [155] and Escudier's regime diagram [67]. The present results provide more detail than the GITT simulation owing to the accuracy and improvements of the present revised LBM results. For example, details of the flow structure within the vortices are visible, highlighting the advantage of the present approach. Three vortex breakdown structures can be seen in Fig. 8.7, two connected in the central region and a separated one further below, as also found in the GITT simulation [154] and Escudier's experimental data [67]. Again, the present method provides more detail such as the flow pattern inside the bubbles, the location of stagnation points, and the length of the bubbles, which cannot be discerned in the GITT work. Fig. 8.8 illustrates three vortex breakdowns, two in the middle zone and one close to the bottom endwall, consistent with the results obtained by GITT [154] and Escudier's study [67]. Additional detail is provided on the bubble structure, concerning the flow pattern and the length of vortices, which cannot be determined from the GITT results.

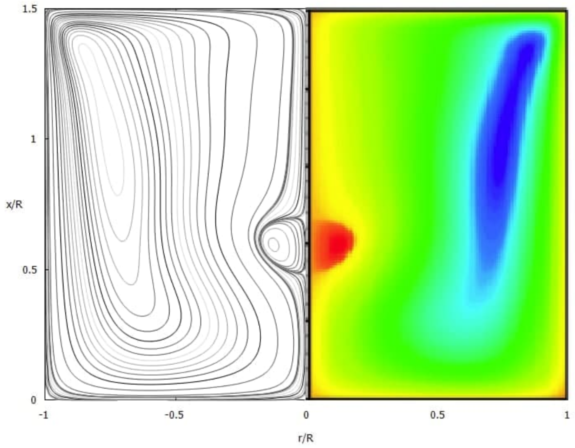

Figure 8.6: Steady flow in a cylindrical container with one rotating (top) end plate for A=1.5, and Re=1290 : (Left) computed streamlines using the present method and (Right) streamline counter by GITT method (Quaresma et al., 2021).

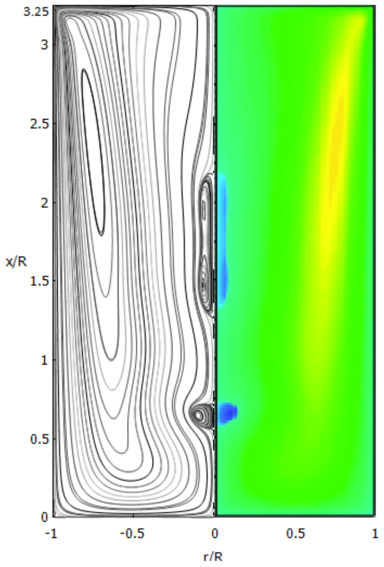

Figure 8.7: Steady flow in a cylindrical container with one rotating (top) end plate for A=3.25, Re=2819 : (Left) computed streamlines using the present method and (Right) streamline counter by GITT method (Quaresma et al., 2021).

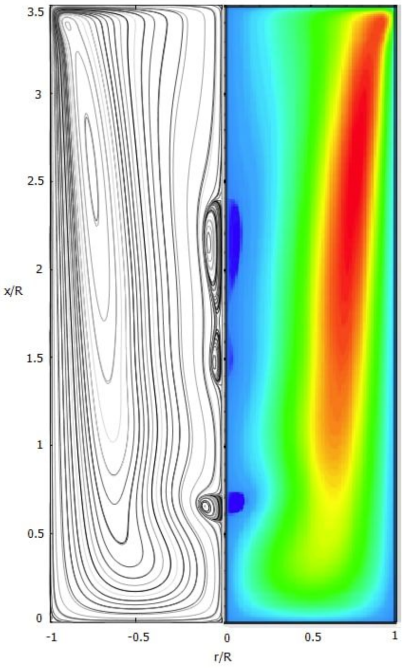

Figure 8.8: Steady flow in a cylindrical container with one rotating (top) end plate for A=3.5, Re=3061 : (Left) computed streamlines using the present method and (Right) streamline counter by GITT method (Quaresma et al., 2021).

8.3 Discussion

A computer code was created in FORTRAN that coupled the second order Bounce back method with the axisymmetric lattice Boltzmann revised method for flows involving solid wall boundary conditions. Fig. 8.9 shows steady flow in a cylindrical container with a rotating bottom endwall for (A, Re) = (2.5, 2126) and (A, Re) = (3.25, 2752). Tables 8.1 and 8.2 compare the locations of stagnation points predicted by the present scheme and previously published experimental data and alternative accessible numerical prediction. The results confirm the capability of the new code. The location of the stagnation points is in good agreement with the experimental and numerical results. It also proves that the code modifications can produce results that are more accurate. Table 8.3 compares the predicted maximum axial velocity at r=0 and its axial position against previous numerical and experimental results, again conforming the precision of the new code.

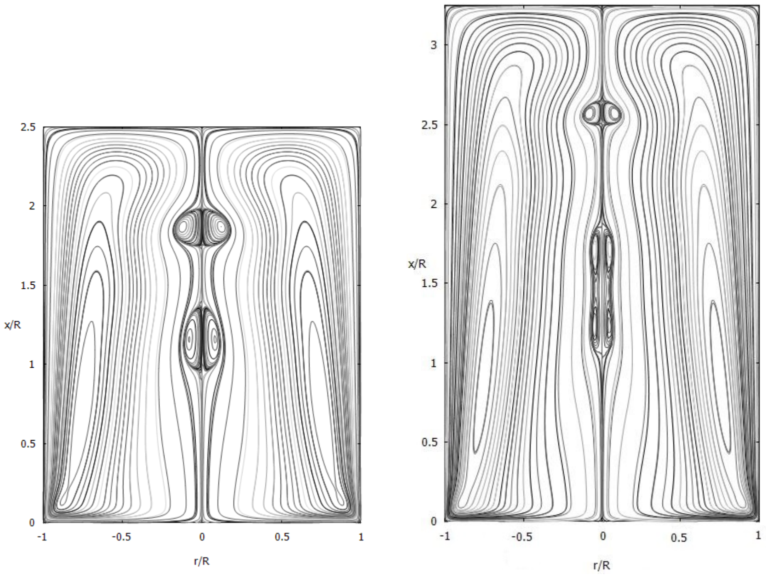

(a) (b)

Figure 8.9: Computed streamlines for steady flow in a cylindrical container with one rotating (bottom) end plate: (a) (A, Re) = (2.5, 2126); and (b) (A, Re) = (3.25, 2752)

Table 8.1: Locations of stagnation points for steady flow in a cylindrical container with rotating bottom endplate when (A, Re) = (2.5, 2126). (UB: upper bubble, LB: lower bubble.)

	Above UB	Below UB	Above LB	Below LB
Present	X=1.985	X=1.745	X=1.385	X=0.945
AxLAB®	X=1.955	X=1.695	X=1.325	X=0.925
Experimental [67]	X=2	X=1.76	X=1.37	X=0.95
Yamada and Suzuki[152]	X=1.98	X=1.75	X=1.36	X=0.95

Table 8.2: Locations of stagnation points for steady flow in a cylindrical container with rotating bottom end plate when (A, Re) = (3.25, 2752). (UB: upper bubble, LB: lower bubble.)

	Above UB	Below UB	Above LB	Below LB
Present	X=2.647	X=2.505	X=1.855	X=1.038
AxLAB®	X=2.625	X=2.575	X=1.898	X=1.085
Experiment [67]	X=2.65	X=2.51	X=1.84	X=1.04
Yamada and Suzuki[152]	X=2.64	X=2.49	X=1.83	X=1.05

The predicted value of the maximum axial velocity component ($u_{x,max}$) and its axial position h_{max}/H are listed in Table. 8.3 for (A, Re) = (1.5, 990),(1.5, 1290), and (2.5, 1010) at *r=0*, and the solutions are compared with corresponding result from AxLAB® [2], GITT [154], 3D lattice Boltzmann method (LBM) and physical test data [77]. The relative error was computed using the formula $\mid \frac{u_{x,num} - u_{x,exp}}{u_{x,exp}} \mid$. The accuracy of the new axisymmetric lattice Boltzmann revised method has been improved, as shown in Table. 8.3 and Table. 8.4. For example, the relative error between the present model and experimental results for *Re*=990 is 1.65%, which is less than that of the previous method (2.27%), 0.49% for *Re*=1010 compared to 1.94% for AxLAB®, and 3.38% for *Re*=1290, which is less than the AxLAB® result (3.82%). Table. 8.3 confirms that the present method successfully predicts the location of maximum axial velocity. Table. 8.4 indicates that the relative error between the present model and 3D LBM [155] is greater than obtained for other numerical methods. The differences can be explained by the fact that 3D LBM is constructed using compressible flow equations in the incompressible limit; as a result, there will be some errors related to changes in spatial density when simulating incompressible flows with a finite, nonzero Mach number [155]. The foregoing results demonstrate the great improvements of the new scheme at all the Reynolds numbers considered here.

Table 8.3: Comparison of maximum axial velocity and its location for different Reynolds numbers and aspect ratios at r = 0, for steady flow in a cylindrical container with rotating bottom endplate.

	Re=990,A=1.5		Re=1010, A=2.5		Re=1290, A=1.5	
	$u_{x,max}/u_0$	h_{max}/H	$u_{x,max}/u_0$	h_{max}/H	$u_{x,max}/u_0$	h_{max}/H
Present	0.0986	0.207	0.1035	0.452	0.0703	0.14
AxLAB® [2]	0.0992	0.207	0.105	0.448	0.0706	0.147
GITT [154]	0.0986	0.207	0.103	0.445	0.0704	0.142
Experiment [77]	0.097	0.21	0.103	0.46	0.068	0.14
3D LBM [155]	0.093	0.22	0.102	0.52	0.072	0.16

Table 8.4: Comparison of relative error for (A, Re) = (1.5, 990),(2.5, 1010) and (1.5, 1290), for steady flow in a cylindrical container with a rotating bottom endplate.

	Re = 990	Re = 1010	Re = 1290
Present-Exp	1.65%	0.49%	3.38%
AxLAB®-Exp	2.27%	1.94%	3.82%
Peresent-GITT	0%	0.49%	0.14%
AxLAB®-GITT	0.6%	1.9%	0.28%
present-3D LBM	6.0%	1.5 %	2.36 %
AxLAB®-3D LBM	6.67%	2.9%	1.94%

8.4 Conclusions

The traditional axisymmetric lattice Boltzmann revised method produces first-order behaviour in the solution error due to applying local equilibrium distribution functions in the boundary conditions. By introducing the second-order bounce-back scheme, the model for non-slip boundary conditions achieves second-order accurate results. This is because the exact lattice geometry of the boundary accords with the boundary equation in the LBGK simulation using the second-order bounce-back approach. A generalised bounce-back approach is suggested, in which the precise lattice geometry of the boundary is adequately taken into account for any arbitrarily irregular lattice geometry at the boundary. To demonstrate the efficacy of the novel axisymmetric lattice Boltzmann revised approach, tests were carried out for steady flow in a cavity at varying Reynolds number and aspect ratio. The resulting improvement has been demonstrated by considering the maximum axial velocity component and comparing the relative error, taking experimental data to the benchmark obtained using the conventional axisymmetric lattice Boltzmann technique with the present scheme. Moreover, the present technique provides additional information, enabling better insight into the details of the actual flow structure.

Chapter 9

AxLAB® with 2^{nd} order bounce-back method for turbulent flow

9.1 Turbulent pipe flow through an abrupt axisymmetric constriction

Let us consider a simulation of turbulent flow through an axisymmetric constriction originally carried out by Nygård [74]. Fig. 9.1, provides a sketch of the flow geometry. The computational domain has an axial length of *5D*, where D is the diameter of the cylinder. The shaded region in Fig. 9.1 represents an axisymmetric constriction, and H and L, respectively, stand for the height and length of the constriction. In this case, $H = 0.5L = 0.25D$. According to Nygard and Andersson [74], a laminar Poiseuille flow is prescribed at the inlet and outflow with random disturbance added to mimic turbulent transition.

An axial pressure gradient at the entrance to the pipe drives the flow, keeping the bulk flow constant at U_b. The Reynolds number is 22 000, following Wang [157] who conducted physical tests. Within the test segment, the long inlet and outflow produced

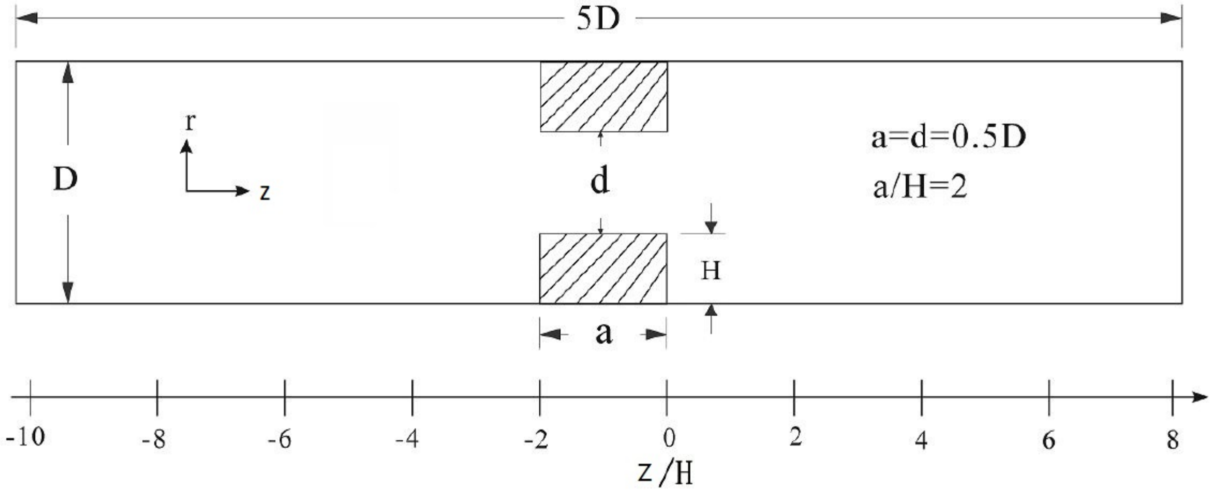

Figure 9.1: A schematic representation of the flow geometry.

a well-developed turbulent flow. The top and bottom domain walls have no slip boundary condition. A Smagorinsky constant of $Cs = 0.3$ and time-step t 0f 0.2s were employed in the simulations, which was run on uniformly 500 × 100 lattice. Different lattices in r-z plane, i.e., 25 × 125, 50 × 250, 100 × 500 and 200 × 1000, were used to check the convergence and stability of the present method. The findings show that if more than 50 × 250 lattices are used, solutions are independent of the choice of lattice number. A lattice size of $\Delta x = 0.2$ is utilised in present simulation and corresponds to 100 × 500. After steady flow was established, the numerical results were acquired, and compared with the experimental data presented by Wang [157] to prove that the current model is correct, in which all lengths and velocities are nondimensionalized by D and U_b, respectively. The end of the shaded rectangle in Fig. 9.1 is chosen as the origin $z/H = 0$. Figures 9.2, 9.3, 9.4 compare mean axial velocity profiles downstream of the constriction at three different locations, with the present model, predictions exhibiting good agreement with Wang's experimental data [157]. Further, a comparison between results from AxLAB® and the present model shows that use of the second-order bounce-back method for the boundary conditions leads to more precise results not only for the region close to the wall, but also for the entire computational domain.

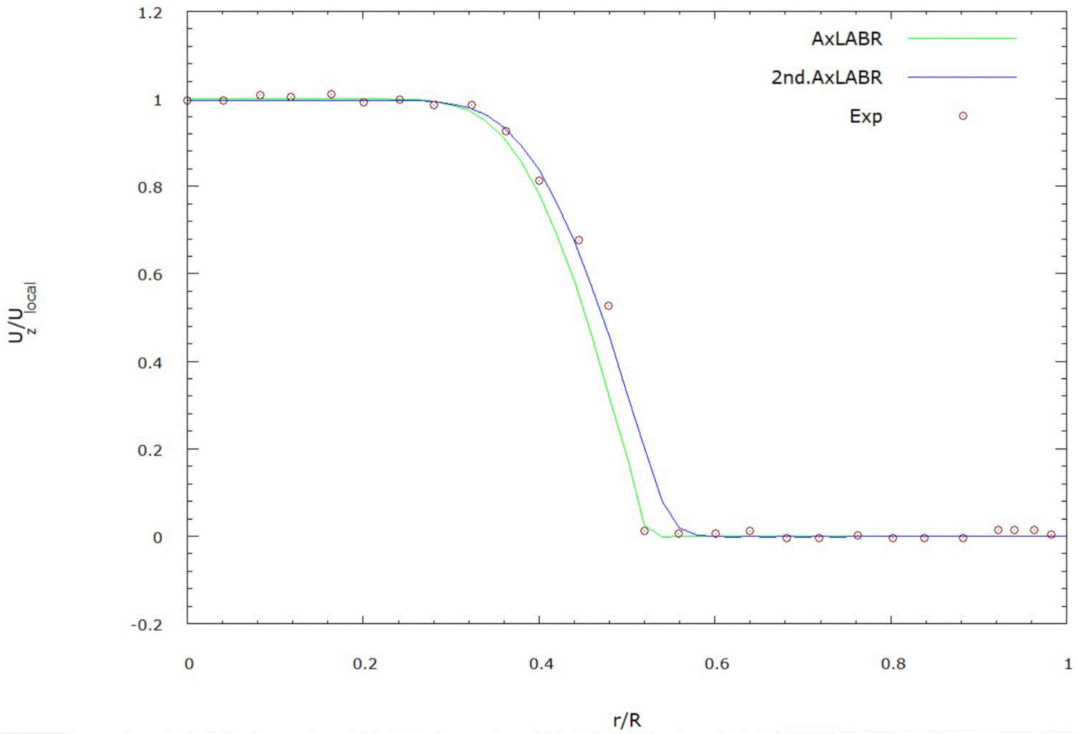

Figure 9.2: Steady turbulent flow through a pipe with axisymmetric constriction: Comparison between predicted and measured mean axial velocity profiles at $Z/H = 0.04$.

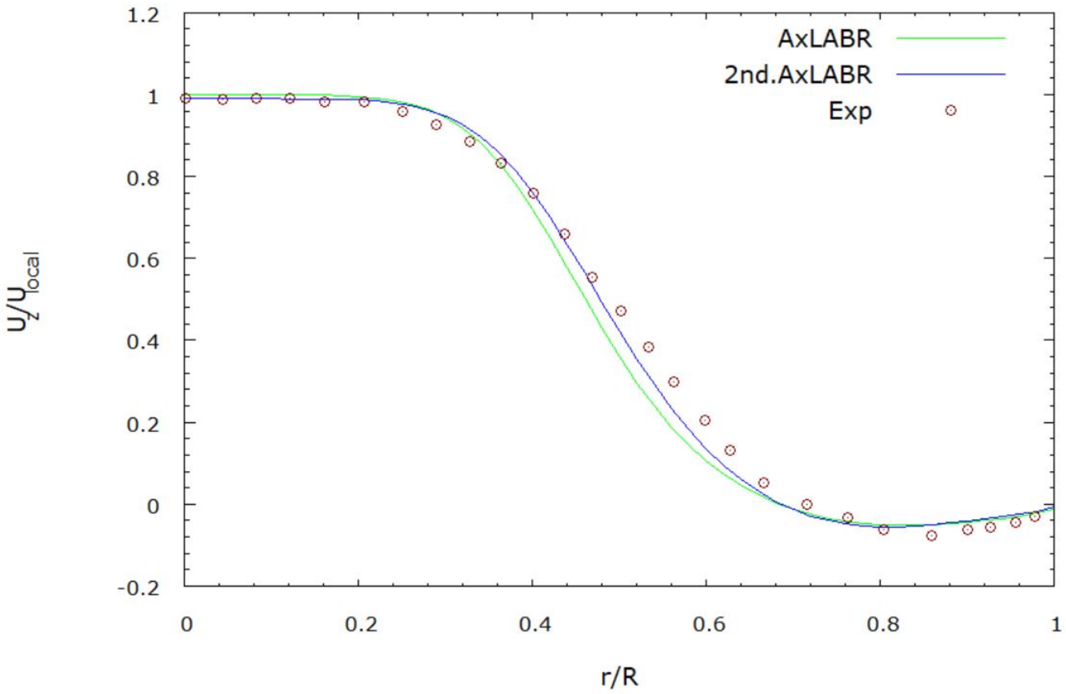

Figure 9.3: Steady turbulent flow through a pipe with axisymmetric constriction: Comparison between predicted and measured mean axial velocity profiles at $Z/H = 2$.

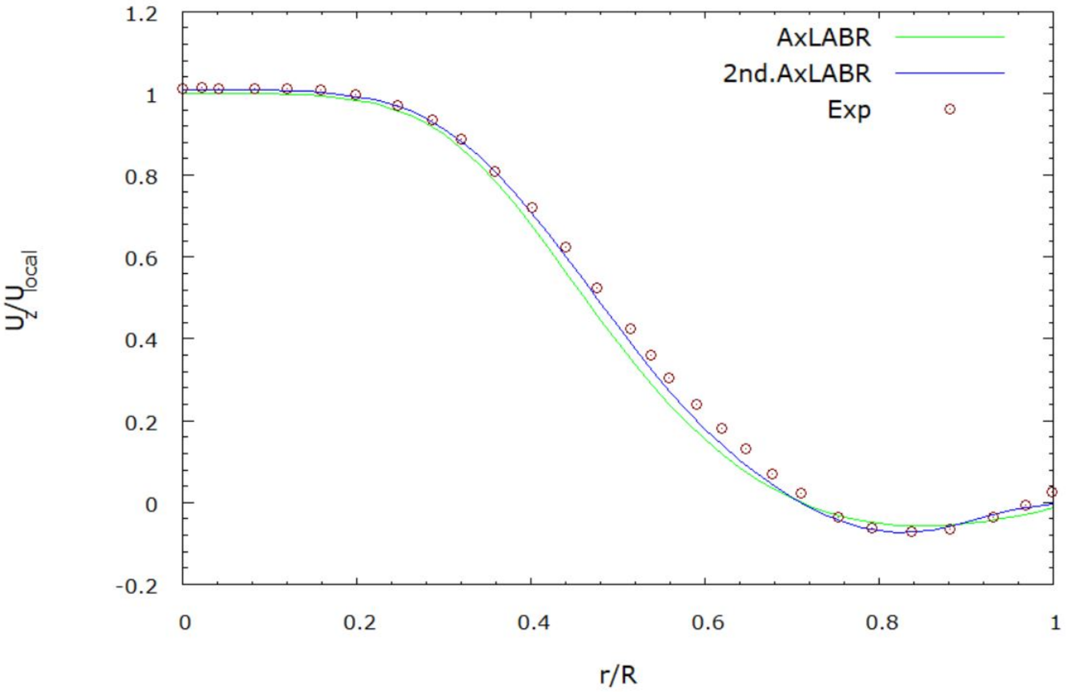

Figure 9.4: Steady turbulent flow through a pipe with axisymmetric constriction: Comparison between predicted and measured mean axial velocity profiles at $Z/H = 4$.

Figs. 9.5-9.8 present The axial velocity histories at two representative locations in the pipe. It can be seen that the axial velocity component fluctuates around a mean component over a duration of 1300s. The impact of gradual oscillation amplitude over time on solution accuracy depends on the specific problem, numerical method, and physical phenomena [158]. To maintain solution accuracy when dealing with gradually changing oscillation amplitudes, it is crucial to use adaptive mesh refinement and validate the results against experimental or analytical data if available to ensure accuracy. This shows qualitatively that turbulence modelling based on a subgrid-scale stress model provides further information than a time-average turbulence model such as the $k - \epsilon$ model [61].

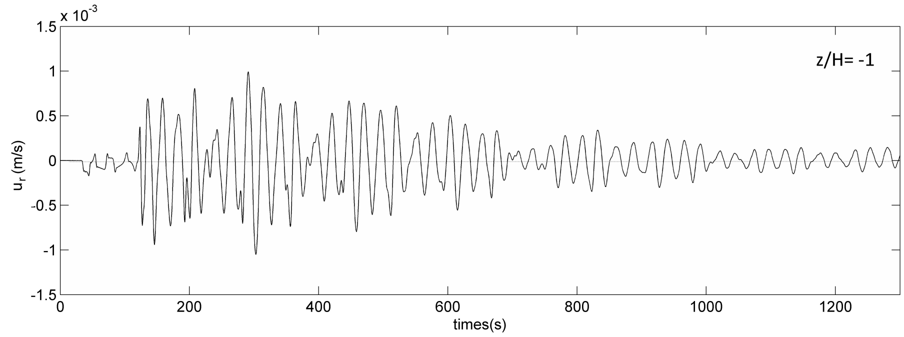

Figure 9.5: Turbulent flow through a pipe with axisymmetric constriction: time history of centerline longitudinal velocity at $Z/H = -1$.

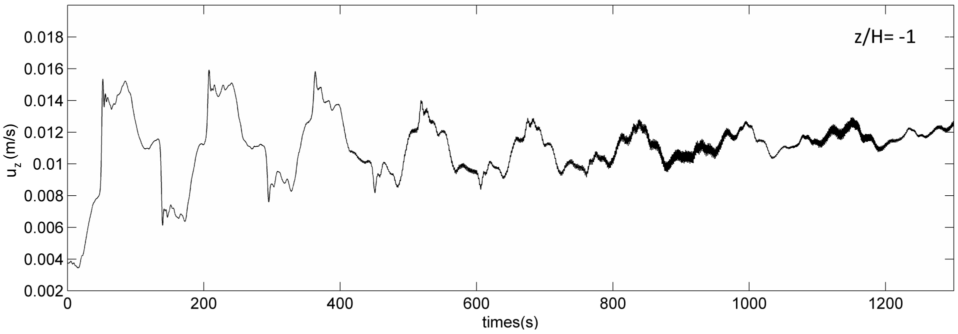

Figure 9.6: Turbulent flow through a pipe with axisymmetric constriction: time history of centerline longitudinal velocity at $Z/H = -1$.

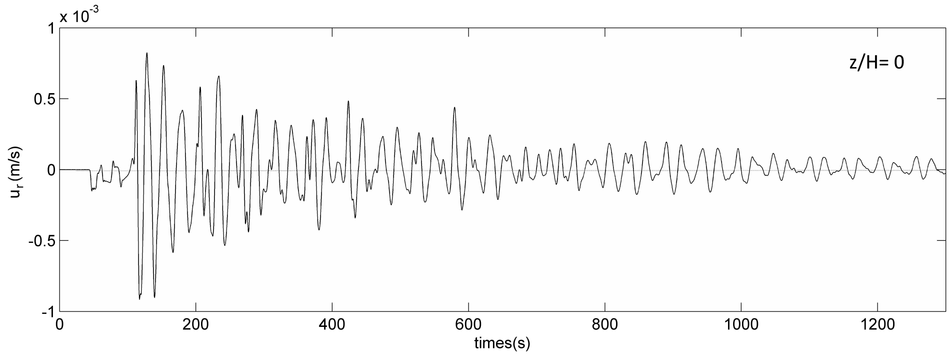

Figure 9.7: Turbulent flow through a pipe with axisymmetric constriction: time history of centerline longitudinal velocity at $Z/H = 0$.

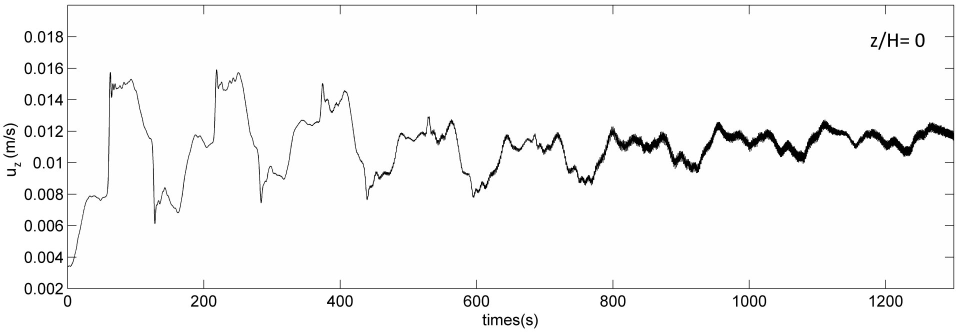

Figure 9.8: Turbulent flow through a pipe with axisymmetric constriction: time history of centerline longitudinal velocity at $Z/H = 0$.

Fig. 9.9 shows a visualisation of the axial velocity at time $t = 1200s$. Due to the short pipe domain, the streamwise velocity component decreases in the region from $z = -10H$ to $z = -4H$. The constriction has a significant impact on the velocity profile at $0.5H$ upstream of the ring. Here, the bulk flow is diverted in the direction of the axis of the pipe. As the ensuing jet spreads downwind of the constriction, the flow is then strongly accelerated through the ring before decelerating once more. The expected separation at the wall is also visible in the streamwise velocity behaviour downstream of the constriction. In Fig. 9.9, separation can be seen; the blue colour indicates negative values of axial velocity component, or flow reversal, entirely consistent with the findings by Nygråd and Anderson [74].

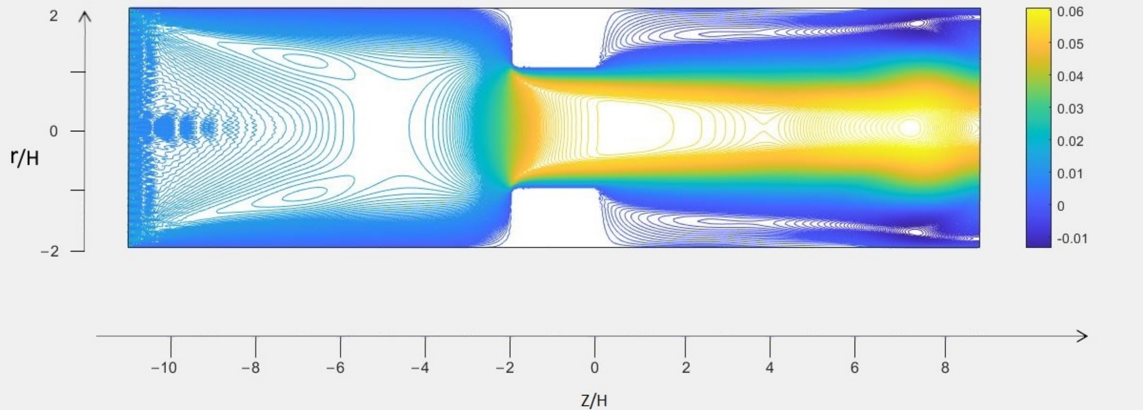

Figure 9.9: Visualization of instantaneous axial velocity at time $t = 1200s$ in the $r - z$ plane.

9.2 Axisymmetric turbulent flow pass a truncated circular cylinder

Rastgou and Saedodin [159] studied axisymmetric detached and reattached turbulent flow past a truncated circular cylinder, which is used as the second test case for the present model. Figure 9.10 schematically depicts the computational domain and the boundary conditions. The cylinder's radius is R, the domain length is $40R$, the domain radius is $30R$ from the axis, and the head of the cylinder is located $25R$ from the inlet. The computations are performed utilising 800 × 600 lattices with no-slip boundary conditions applied at the wall. The flow has a Reynolds number of 6000, following Rastgou and Saedodin [159].

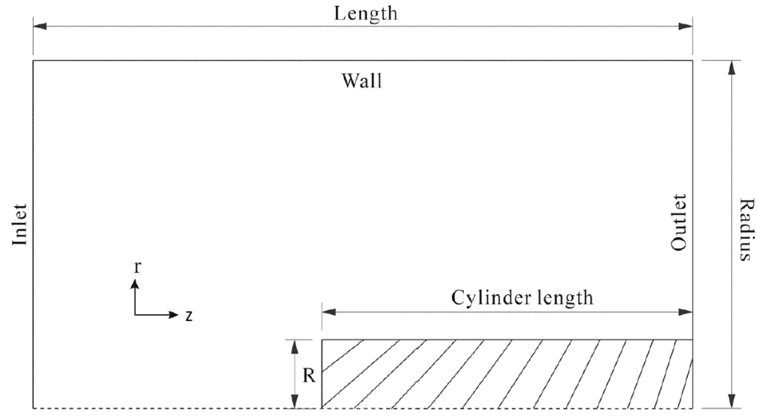

Figure 9.10: Computational domain and boundary conditions for simulation of axisymmetric turbulent flow pass a truncated circular cylinder, whose axis is oriented in the flow direction.

Figs.9.11 and 9.12 compare mean velocity profiles predicted by the present scheme with results from alternative numerical methods. Relatively good agreement is obtained at the same level of precision, as the other methods. In addition, comparisons against the experimental findings of Ota [160] with $Re = 56200$ and Kiya et al. [161] for $Re = 10^5$ indicate some slight disagreement in the reverse flow area, which depends on the Reynolds number.

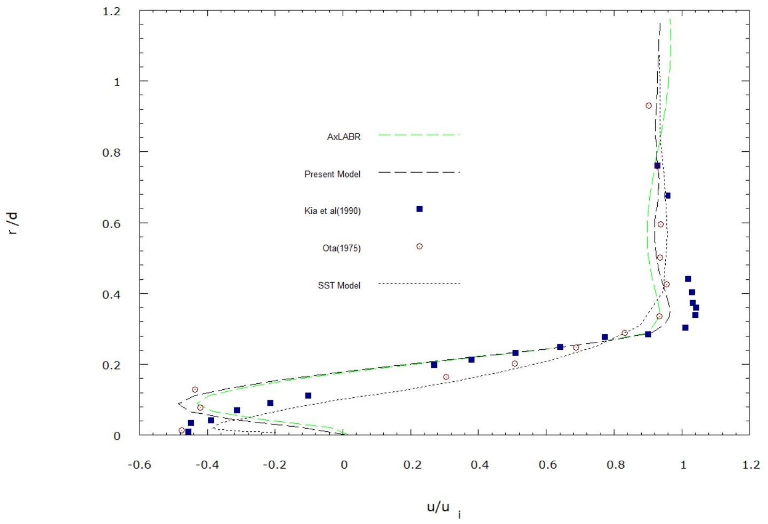

Figure 9.11: Axisymmetric turbulent flow pass a truncated circular cylinder whose axis is oriented in the flow direction: mean velocity profile in the r-direction at a section in the separation region.

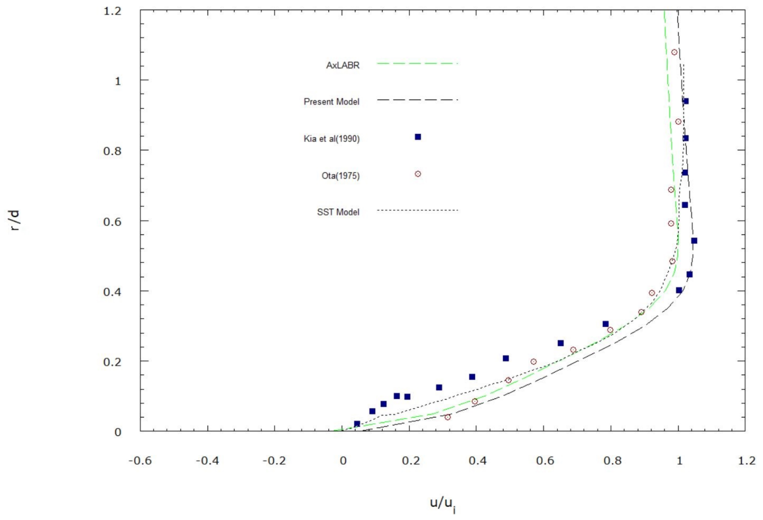

Figure 9.12: Axisymmetric turbulent flow pass a truncated circular cylinder whose axis is oriented in the flow direction: mean velocity profile in the r-direction at a section out of the separation region.

Figs.9.11 and 9.12 show that the present predictions agree closely with corresponding results from experiment and alternative numerical methods, particularly for the region close to the wall domain due to application of the second-order bounce-back method at the wall boundaries.

The reattachment length (L.R.), defined as the distance between the separation point (near the leading edge) and the reattachment point, is one of the leading features of flow separation encountered in the present study. The shear stress on the wall is zero at the separation and reattachment points. This parameter influences the aerodynamic properties of a circular cylinder with a fixed length-to-diameter ratio, an example being drag. In the heat transfer literature [162], however, it is commonly expected that the peak in the local heat transfer coefficient takes place at the reattachment point. The number of nodes in a structured uniform grid used for calculations is 480000.

Convergence tests were undertaken on different grids, revealing that the results remained unchanged on finer grids. Table 9.1 lists the reattachment length in relation to mesh resolution for the present model and AxLAB® models. The results from the 480000 mesh are considered grid independent and are included in this paper because, as Table 9.1 shows, the reattachment length obtained from the Fine Mesh is identical to that obtained from the Medium Mesh (with less than 1% difference for the AxLAB® and present models). According to Ota [160] and Kiya et al. [161]'s experimental findings, the reattachment length of the turbulent separated shear is independent of Reynolds number, being roughly 1.6 times the diameter. Figure 9.13 is a streamline plot which demonstrates that the present model produces a reattachment length of 1.62 times the cylinder diameter, which is 1.51 times that for AxLAB®, suggesting that the results obtained from the second-order AxLAB® are closer to the SST model [159], which is superior to the other techniques. The aforementioned results show that the present model performs well when simulating complex flows in the turbulent boundary layer.

Table 9.1: Reattachment length(R.L.) versus the mesh for present model and AxLAB®.

	Coarse mesh	Medium mesh	Fine mesh
Number of nodes	24000	480000	960000
R.L. For Present model	$1.6d$	$1.62d$	$1.63d$
R.L. For the AxLAB® model	$1.48d$	$1.51d$	$1.51d$

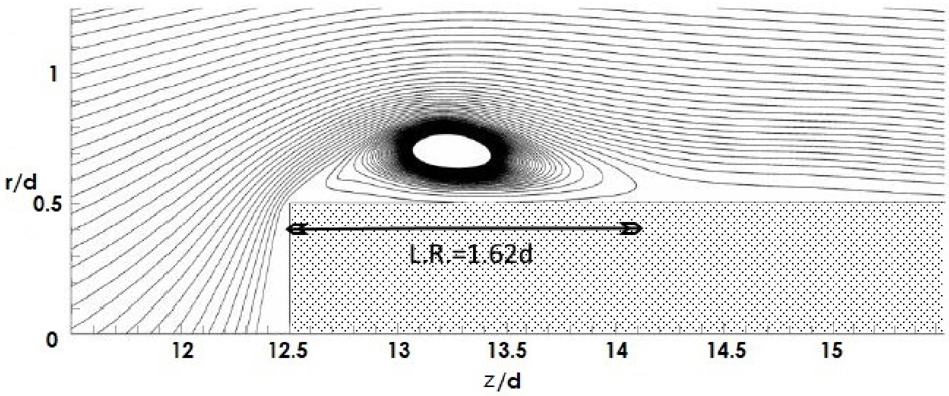

Figure 9.13: Streamlines using the second-order AxLAB® with turbulence for an axisymmetric turbulent flow pass a truncated circular cylinder whose axis is oriented in the flow direction.

Chapter 10

Conclusions and Future Work

10.1 Introduction

The axisymmetric lattice Boltzmann approachA is modern CFD technique based on the microscopic resolution of flouid physics which is especially suitable for simulating complex axisymmetric flows. This thesis examines the performance of AxLAB® in modelling axisymmetric flows within a cylindrical domain, in a pipe, and past a truncated cylinder aligned with the flow direction. The primary objectives of this work are to improve the accuracy of the AxLAB® technique and develop a new code to model axisymmetric rotating flows and turbulent flows with complex boundary conditions, and unsteady-periodic flows. This objective was achieved by first reviewing the development of the lattice Boltzmann method (LBM). LBM theory for the axisymmetric flow equations (AxLAB®) was then carefully examined. Numerous typical axisymmetric flow issues, including laminar and turbulent examples, have been addressed using the numerical approach. Published experimental data and alternative numerical solutions are used to validate the numerical scheme. Key contributions and conclusions are listed below.

10.2 Conclusions

The thesis has described the development of lattice Boltzmann methods AxLAB® for laminar and turbulent axisymmetric flows. The well-established D2Q9 lattice pattern, comprising a two-dimensional nine velocities lattice is employed. First-order and second-order bounce-back techniques are used for solid wall boundary conditions. Numerical experiments reveal that the second-order bounce-back approach for no-slip boundary conditions, provides simulation that are more similar to experimental data than other numerical scheme, demonstrating how the present scheme offers a significant improvement over exixting. Numerous simulation studies for both laminar and turbulent flows were conducted for benchmark swirling and benchmark axisymmetric flow. The subsequent paragraphs list the study's major accomplishments and findings.

- AxLAB® Application to Complex Laminar Flows

  The numerical models were tested for a number of cases for which experimental data and alternative numerical solution were available. The results demonstrated that the present model are accurate for steady cylindrical cavity flows and axisymmetric swirling flows in cylinders with rotating top and bottom endplates. Investigation into the axial flow velocity component along the cylinder axis revealed that, for a given aspect ratio, changes in the rotational Reynolds number might either increase or decrease the maximum axial velocity along the axis of the cylinder. Further research into the vortex breakdown phenomena was carried out using numerical analyses to determine how vortex breakdown occurs and how many vortex breakdowns there are in each case.

- Application to Unsteady-periodic Flow

  To the author's knowledge, this is the first numerical investigation of unsteady-periodic flows that has quantified the flow periodicity. The process of creating the vortex breakdowns for unsteady-periodic flow with Re= 2765 and A = 2.5 is fully explained and the period of vortex collapse determined after a numerical test was carried out. The highest axial velocities along the cylinder axis were used to determine the absolute error and relative error between two patterns at different time instants was the key to determining the period time step. knowledge of the flow periodicity enables better forecasting and management of the behaviour of unsteady-periodic flow, which could enhance the efficiency of industrial machinery. The number of stagnation points and their locations were discussed throughout a flow period.

- Improve model of the accuracy of AxLAB® by incorporation of the second-order bounce-back method

  To increase model accuracy, a modified version of the axisymmetric lattice Boltzmann updated method is applied in collaboration with the second-order bounce-back boundary condition for solid walls. This led to more accurate results than the other approaches. Several studies, such as flow in a cylindrical container with rotating top and bottom endplates were simulated to test the modified code. Maximum axial velocities along the cylinder's axis, their positions, and stagnation points were all considered. Results from AxLAB® and the modified code were compared against existing experimental data and alternative numerical solutions, and it was found that the modified LBM achieved significant improvement in the results where the second-order bounce-back scheme was applied at the wall boundary.

- Development of second-order AxLAB® for Turbulent Flows

  The second-order AxLAB® was enhanced to mimic turbulent flow. By incorporating the standard subgrid-scale (SGS) stress model into the axisymmetric lattice Boltzmann equation in a way that was consistent with the lattice gas dynamics, the turbulent flow was properly represented. The model was validated for two typical engineering cases. The flow behaviour, velocity components and reattachment length were investigated, with the results indicating excellent agreement with experimental data and alternative numerical solutions. The findings also demonstrate that incorporating a subgrid-scale stress model and the second order bounce back method in the AxLAB® for turbulent flows can provide more accurate results compared with the traditional AxLAB®, specifically while predicting the flow behaviour close to the solid wall.

10.3 Future Research

In future, it is recommended that the model undergo the following improvement.

- Chapters 8 and 9 discussed the enhanced accuracy of the AxLAB® for no-slip boundary conditions. The model should next be extended for more advanced slip boundary conditions. This might be accomplished by updating the model to include more precise slip boundary condition approaches. Incorporating the present model with a higher accurate scheme for slip wall boundary conditions leads to the development of the present model application.
- The feature of fluid compressibility in the AxLAB® model has an impact on the accuracy of the results, particularly for unsteady flows. Further research on incompressible AxLAB® is required to improve the outcomes for unsteady flows.
- The application of AxLAB® will be developed by simulating an actual atmospheric phenomena, such as an axisymmetric tornado. It is recommended that the link between vortex structure, intensity, and unsteadiness as functions of diffusion and rotation be investigated using axisymmetric simulations with constant viscosity.
- GPU technique and parallel computation for AxLAB®. Huge amounts of grid lattices are required to replicate axisymmetric flows that exist in real situations. Parallel computing and GPU technology are desirable to improve computational performance. High-performance graphics and processors designed for parallel computation will make it possible to achieve performance that was previously only conceivable with parallel supercomputers. The intrinsic capability of parallel computation is one of the lattice Boltzmann method's most alluring advantages. Future studies should consider parallel computation for laminar and turbulent flows.

References

[1] C. K. Aidun and J. R. Clausen, "Lattice Boltzmann method for complex flows," *Annual Review of Fluid Mechanics*, vol. 42, pp. 439–472, 2010.

[2] J. G. Zhou, "Axisymmetric lattice Boltzmann method revised," *Physical Review E*, vol. 84, no. 3, p. 036704, 2011.

[3] S. Chen and G. D. Doolen, "Lattice Boltzmann method for fluid flows," *Annual Review of Fluid Mechanics*, vol. 30, no. 1, pp. 329–364, 1998.

[4] W. Osborn, E. Orlandini, M. R. Swift, J. Yeomans, and J. R. Banavar, "Lattice Boltzmann study of hydrodynamic spinodal decomposition," *Physical Review Letters*, vol. 75, no. 22, p. 4031, 1995.

[5] M. A. Spaid and F. R. Phelan Jr, "Lattice Boltzmann methods for modelling microscale flow in fibrous porous media," *Physics of Fluids*, vol. 9, no. 9, pp. 2468–2474, 1997.

[6] J. G. Zhou, D. M. Causon, D. M. Ingram, and C. G. Mingham, "Numerical solutions of the shallow water equations with discontinuous bed topography," *International Journal for Numerical Methods in Fluids*, vol. 38, no. 8, pp. 769–788, 2002.

[7] J. G. Zhou, "A lattice Boltzmann model for groundwater flows," *International Journal of Modern Physics C*, vol. 18, no. 06, pp. 973–991, 2007.

[8] I. Halliday, L. Hammond, C. Care, K. Good, and A. Stevens, "Lattice Boltzmann equation hydrodynamics," *Physical Review E*, vol. 64, no. 1, p. 011208, 2001.

[9] T. Lee, H. Huang, and C. Shu, "An axisymmetric incompressible lattice Boltzmann model for pipe flow," *International Journal of Modern Physics C*, vol. 17, no. 05, pp. 645–661, 2006.

[10] K. N. Premnath and J. Abraham, "Simulations of binary drop collisions with a multiple-relaxation-time lattice-Boltzmann model," *Physics of Fluids*, vol. 17, no. 12, p. 122105, 2005.

[11] S. Mukherjee and J. Abraham, "A pressure-evolution-based multi-relaxation-time high-density-ratio two-phase lattice-Boltzmann model," *Computers & Fluids*, vol. 36, no. 6, pp. 1149–1158, 2007.

[12] T. Reis and T. N. Phillips, "Modified lattice Boltzmann model for axisymmetric flows," *Physical Review E*, vol. 75, no. 5, p. 056703, 2007.

[13] Z. Guo, H. Han, B. Shi, and C. Zheng, "Theory of the lattice Boltzmann equation: lattice Boltzmann model for axisymmetric flows," *Physical Review E*, vol. 79, no. 4, p. 046708, 2009.

[14] Q. Li, Y. He, G. Tang, and W. Tao, "Improved axisymmetric lattice Boltzmann scheme," *Physical Review E*, vol. 81, no. 5, p. 056707, 2010.

[15] J. G. Zhou, "Axisymmetric lattice Boltzmann method," *Physical Review E*, vol. 78, no. 3, p. 036701, 2008.

[16] R. Weber, F. Boysan, J. Swithenbank, and P. Roberts, "Computations of near field aerodynamics of swirling expanding flows," in *Symposium (International) on Combustion*, vol. 21, no. 1. Elsevier, 1988, pp. 1435–1443.

[17] J. Swithebank and N. Chigier, "Vortex mixing for supersonic combustion," in *Symposium (International) on Combustion*, vol. 12, no. 1. Elsevier, 1969, pp. 1153–1162.

[18] N. Syred and J. Beer, "Combustion in swirling flows: a review," *Combustion and Flame*, vol. 23, no. 2, pp. 143–201, 1974.

[19] O. Lucca-Negro and T. O'doherty, "Vortex breakdown: a review," *Progress in Energy and Combustion Science*, vol. 27, no. 4, pp. 431–481, 2001.

[20] M. Al-Fahham, F. A. Hatem, A. S. Alsaegh, A. Valera Medina, S. Bigot, and R. Marsh, "Experimental study to enhance resistance for boundary layer flashback in swirl burners using microsurfaces," in *Turbo Expo: Power for Land, Sea, and Air*, vol. 50848. American Society of Mechanical Engineers, 2017, p. V04AT04A030.

[21] W. Thacker, "Comparison of finite-element and finite-difference schemes. Part II: Two-dimensional gravity wave motion," *Journal of Physical Oceanography*, vol. 8, no. 4, pp. 680–689, 1978.

[22] H. Deconinck and T. Barth, "Special course on unstructured grid methods for advection dominated flows," *AGARD Report*, vol. 787, 1992.

[23] J. Murthy and S. Mathur, "Radiative heat transfer in axisymmetric geometries using an unstructured finite-volume method," *Numerical Heat Transfer, Part B*, vol. 33, no. 4, pp. 397–416, 1998.

[24] P. Lyra, R. Lima, C. Guimarães, and D. de Carvalho, "An edge-based unstructured finite volume procedure for the numerical analysis of heat conduction applications," *Journal of the Brazilian Society of Mechanical Sciences and Engineering*, vol. 26, pp. 160–169, 2004.

[25] S. Wolfram, "Statistical Mechanics of Cellular Automata," *Reviews of Modern Physics*, vol. 55, no. 3, p. 601, 1983.

[26] A. Pires, D. Landau, and H. Herrmann, "Workshop on Computational Physics And Cellular Automata," in *Workshop on Computational Physics And Cellular Automata.* World Scientific, 1990, pp. 1–207.

[27] D. Campos and V. Méndez, "A lattice-model representation of continuous-time random walks," *Journal of Physics A: Mathematical and Theoretical*, vol. 41, no. 8, p. 085101, 2008.

[28] K. Zuse, *Calculating Space.* Massachusetts Institute of Technology, Project MAC Cambridge, MA, 1970.

[29] J. Hardy, Y. Pomeau, and O. De Pazzis, “Time evolution of a two-dimensional model system. I. Invariant states and time correlation functions,” *Journal of Mathematical Physics*, vol. 14, no. 12, pp. 1746–1759, 1973.

[30] M. Gardner, “The Fantastic Combinations of John Conway’s New Solitaire Game Life,” *Sc. Am.*, vol. 223, pp. 20–123, 1970.

[31] S. Wolfram, “Theory and Applications of Cellular Automata,” *World Scientific*, 1986.

[32] H. Liu, J. G. Zhou, and R. Burrows, “Lattice Boltzmann simulations of the transient shallow water flows,” *Advances in Water Resources*, vol. 33, no. 4, pp. 387–396, 2010.

[33] U. Frisch, B. Hasslacher, and Y. Pomeau, “Lattice Gas Automata for the Navier-Stokes Equation,” in *Lattice Gas Methods for Partial Differential Equations.* CRC Press, 2019, pp. 11–18.

[34] D. A. Wolf-Gladrow, *Lattice Gas Cellular Automata and Lattice Boltzmann Models: an introduction.* Springer, 2004.

[35] G. R. McNamara and G. Zanetti, “Use of the Boltzmann equation to simulate lattice-gas automata,” *Physical Review Letters*, vol. 61, no. 20, p. 2332, 1988.

[36] F. J. Higuera and J. Jiménez, “Boltzmann approach to lattice gas simulations,” *EPL (Europhysics Letters)*, vol. 9, no. 7, p. 663, 1989.

[37] S. Chen, D. Martinez, and R. Mei, “On boundary conditions in lattice Boltzmann methods,” *Physics of Fluids*, vol. 8, no. 9, pp. 2527–2536, 1996.

[38] P. L. Bhatnagar, E. P. Gross, and M. Krook, “A model for collision processes in gases. i. small amplitude processes in charged and neutral one-component systems,” *Physical Review*, vol. 94, no. 3, p. 511, 1954.

[39] M. Fink, “Simulation von Nasenströmungen mit Lattice-BGK-Methoden,” Ph.D. dissertation, Ph. D. dissertation, Essen-Duisburg University, Germany, 2007.

[40] A. Benim, E. Aslan, and I. Taymaz, “Investigation into LBM analysis of incompressible laminar flows at high Reynolds numbers.”

[41] I. Ginzburg, “Equilibrium-type and link-type lattice Boltzmann models for generic advection and anisotropic-dispersion equation,” *Advances in Water Resources*, vol. 28, no. 11, pp. 1171–1195, 2005.

[42] B. Servan-Camas and F. T.-C. Tsai, “Two-relaxation-time lattice Boltzmann method for the anisotropic dispersive Henry problem,” *Water Resources Research*, vol. 46, no. 2, 2010.

[43] P. Nathen, D. Gaudlitz, M. J. Krause, and N. A. Adams, “On the stability and accuracy of the BGK, MRT and RLB Boltzmann schemes for the simulation of turbulent flows,” *Commun Comput Phys*, vol. 23, no. 3, pp. 1–31, 2018.

[44] A. Kuzmin, A. Mohamad, and S. Succi, “Multi-relaxation time lattice Boltzmann model for multiphase flows,” *International Journal of Modern Physics C*, vol. 19, no. 06, pp. 875–902, 2008.

[45] E. Aslan, I. Taymaz, and A. Benim, “Investigation of the lattice Boltzmann SRT and MRT stability for lid-driven cavity flow,” *International Journal of Materials, Mechanics and Manufacturing*, vol. 2, no. 4, pp. 317–324, 2014.

[46] D. d’Humières, “Multiple–relaxation–time lattice Boltzmann models in three dimensions,” *Philosophical Transactions of the Royal Society of London. Series A: Mathematical, Physical and Engineering Sciences*, vol. 360, no. 1792, pp. 437–451, 2002.

[47] Y. B. Bao and J. Meskas, “Lattice Boltzmann method for fluid simulations,” *Department of Mathematics, Courant Institute of Mathematical Sciences, New York University*, vol. 44, 2011.

[48] M. Nobari, Y.-J. Jan, and G. Tryggvason, “Head-on collision of drops—a numerical investigation,” *Physics of Fluids*, vol. 8, no. 1, pp. 29–42, 1996.

[49] J. Hua and J. Lou, “Numerical simulation of bubble rising in viscous liquid,” *Journal of Computational Physics*, vol. 222, no. 2, pp. 769–795, 2007.

[50] R. S. Maier, R. S. Bernard, and D. W. Grunau, “Boundary conditions for the lattice Boltzmann method,” *Physics of Fluids*, vol. 8, no. 7, pp. 1788–1801, 1996.

[51] R. Mei, W. Shyy, D. Yu, and L.-S. Luo, “Lattice Boltzmann method for 3-D flows with curved boundary,” *Journal of Computational Physics*, vol. 161, no. 2, pp. 680–699, 2000.

[52] A. Artoli, A. Hoekstra, and P. Sloot, “3D pulsatile flow with the lattice Boltzmann BGK method,” *International Journal of Modern Physics C*, vol. 13, no. 08, pp. 1119–1134, 2002.

[53] J. Buick and C. Greated, “Gravity in a lattice Boltzmann model,” *Physical Review E*, vol. 61, no. 5, p. 5307, 2000.

[54] Z. Guo, C. Zheng, and B. Shi, “Discrete lattice effects on the forcing term in the lattice Boltzmann method,” *Physical Review E*, vol. 65, no. 4, p. 046308, 2002.

[55] L.-S. Luo, “Unified theory of lattice Boltzmann models for nonideal gases,” *Physical Review Letters*, vol. 81, no. 8, p. 1618, 1998.

[56] Y. Cheng, F. Lien, E. Yee, and R. Sinclair, “A comparison of large eddy simulations with a standard k–ε Reynolds-averaged Navier–Stokes model for the prediction of a fully developed turbulent flow over a matrix of cubes,” *Journal of Wind Engineering and Industrial Aerodynamics*, vol. 91, no. 11, pp. 1301–1328, 2003.

[57] C. M. Teixeira, “Incorporating turbulence models into the lattice-Boltzmann method,” *International Journal of Modern Physics C*, vol. 9, no. 08, pp. 1159–1175, 1998.

[58] J. Smagorinsky, “General circulation experiments with the primitive equations: I. The basic experiment,” *Monthly Weather Review*, vol. 91, no. 3, pp. 99–164, 1963.

[59] M. Tutar and A. Holdø, “Computational modelling of flow around a circular cylinder in sub-critical flow regime with various turbulence models,” *International Journal for Numerical Methods in Fluids*, vol. 35, no. 7, pp. 763–784, 2001.

[60] S. Hou, J. Sterling, S. Chen, and G. Doolen, “A lattice Boltzmann subgrid model for high Reynolds number flows, fields inst,” in *Comm.* Citeseer, 1996.

[61] J. Zhou, “A lattice Boltzmann model for the shallow water equations with turbulence modelling,” *International Journal of Modern Physics C*, vol. 13, no. 08, pp. 1135–1150, 2002.

[62] H. Liu, M. Li, and A. Shu, “Large eddy simulation of turbulent shallow water flows using multi-relaxation-time lattice Boltzmann model,” *International Journal for Numerical Methods in Fluids*, vol. 70, no. 12, pp. 1573–1589, 2012.

[63] J. Lopez, “Axisymmetric vortex breakdown Part 1. Confined swirling flow,” *Journal of Fluid Mechanics*, vol. 221, pp. 533–552, 1990.

[64] A. Y. Gelfgat, P. Bar-Yoseph, and A. Solan, “Three-dimensional instability of axisymmetric flow in a rotating lid–cylinder enclosure,” *Journal of Fluid Mechanics*, vol. 438, pp. 363–377, 2001.

[65] H. U. Vogel, “Experimentelle Ergebnisse ueber die l Laminare Stroemung in einem zylindrischen Gehaeuse mit darin rotierender Sceibe,” *Max-Plank-Institute für Strömungsforschung, Göttingen, Bericht*, vol. 6, 1968.

[66] B. Ronnenberg, “Ein Selbstjustierendes 3-komponenten-Laserdoppler-anemometer nach dem Vergleichsverfaren, angewandt auf Untersuchungen in einer stationären zylindersymmetrischen Drehströmung mit enimen Rückströmgebiet,” *GoĽttingen: Max-Planck-Institut fuĽr StroĽmungsforschung*, 1977.

[67] M. Escudier, “Observations of the flow produced in a cylindrical container by a rotating endwall,” *Experiments in Fluids*, vol. 2, no. 4, pp. 189–196, 1984.

[68] A. Spohn, M. Mory, and E. Hopfinger, “Experiments on vortex breakdown in a confined flow generated by a rotating disc,” *Journal of Fluid Mechanics*, vol. 370, pp. 73–99, 1998.

[69] F. Sotiropoulos, D. R. Webster, and T. C. Lackey, “Experiments on lagrangian transport in steady vortex-breakdown bubbles in a confined swirling flow,” *Journal of Fluid Mechanics*, vol. 466, pp. 215–248, 2002.

[70] G. Brown and J. Lopez, “Axisymmetric vortex breakdown Part 2. Physical mechanisms,” *Journal of Fluid Mechanics*, vol. 221, pp. 553–576, 1990.

[71] J. Lopez and A. Perry, “Axisymmetric vortex breakdown. part 3 onset of periodic flow and chaotic advection,” *Journal of Fluid Mechanics*, vol. 234, pp. 449–471, 1992.

[72] F. Sotiropoulos and Y. Ventikos, “The three-dimensional structure of confined swirling flows with vortex breakdown,” *Journal of Fluid Mechanics*, vol. 426, pp. 155–175, 2001.

[73] F. Sotiropoulos, Y. Ventikos, and T. C. Lackey, “Chaotic advection in three-dimensional stationary vortex-breakdown bubbles: Šil’nikov’s chaos and the devil’s staircase,” *Journal of Fluid Mechanics*, vol. 444, pp. 257–297, 2001.

[74] F. Nygård and H. Andersson, “Numerical simulation of turbulent pipe flow through an abrupt axisymmetric constriction,” *Flow, Turbulence and Combustion*, vol. 91, no. 1, pp. 1–18, 2013.

[75] K. Roesner, “Recirculation zones in a cylinder with rotating lid,” in *Proceedings of the IUTAM Symposium on Topological Fluid Mechanics, 1989*, 1989.

[76] G. Gauthier, P. Gondret, F. Moisy, and M. Rabaud, “Instabilities in the flow between co-and counter-rotating disks,” *Journal of Fluid Mechanics*, vol. 473, pp.

1–21, 2002.

[77] K. Fujimura, H. S. Koyama, and J. M. Hyun, "An experimental study on vortex breakdown in a differentially-rotating cylindrical container," *Experiments in Fluids*, vol. 36, no. 3, pp. 399–407, 2004.

[78] D. T. Valentine and C. C. Jahnke, "Flows induced in a cylinder with both end walls rotating," *Physics of Fluids*, vol. 6, no. 8, pp. 2702–2710, 1994.

[79] J. Lopez, "Unsteady swirling flow in an enclosed cylinder with reflectional symmetry," *Physics of Fluids*, vol. 7, no. 11, pp. 2700–2714, 1995.

[80] M. Yoshino, Y.-h. Hotta, T. Hirozane, and M. Endo, "A numerical method for incompressible non-Newtonian fluid flows based on the lattice Boltzmann method," *Journal of Non-Newtonian Fluid Mechanics*, vol. 147, no. 1-2, pp. 69–78, 2007.

[81] D. Wang and J. Bernsdorf, "Lattice Boltzmann simulation of steady non-Newtonian blood flow in a 3D generic stenosis case," *Computers & Mathematics with Applications*, vol. 58, no. 5, pp. 1030–1034, 2009.

[82] X. Niu, C. Shu, and Y. Chew, "An axisymmetric lattice Boltzmann model for simulation of Taylor–Couette flows between two concentric cylinders," *International Journal of Modern Physics C*, vol. 14, no. 06, pp. 785–796, 2003.

[83] Y. Peng, C. Shu, Y. Chew, and J. Qiu, "Numerical investigation of flows in Czochralski crystal growth by an axisymmetric lattice Boltzmann method," *Journal of Computational Physics*, vol. 186, no. 1, pp. 295–307, 2003.

[84] X. He and L.-S. Luo, "Lattice Boltzmann model for the incompressible Navier–Stokes equation," *Journal of Statistical Physics*, vol. 88, no. 3, pp. 927–944, 1997.

[85] H. Huang, T. Lee, and C. Shu, "Hybrid lattice Boltzmann finite-difference simulation of axisymmetric swirling and rotating flows," *International Journal for Numerical Methods in Fluids*, vol. 53, no. 11, pp. 1707–1726, 2007.

[86] H. Huang, Z. Li, S. Liu, and X.-y. Lu, “Shan-and-Chen-type multiphase lattice Boltzmann study of viscous coupling effects for two-phase flow in porous media,” *International Journal for Numerical Methods in Fluids*, vol. 61, no. 3, pp. 341–354, 2009.

[87] H. Huang and X.-Y. Lu, “Theoretical and numerical study of axisymmetric lattice Boltzmann models,” *Physical Review E*, vol. 80, no. 1, p. 016701, 2009.

[88] H. An, C. Zhang, J. Meng, and Y. Zhang, “Analytical solution of axisymmetric lattice Boltzmann model for cylindrical Couette flows,” *Physica A: statistical mechanics and its applications*, vol. 391, no. 1-2, pp. 8–14, 2012.

[89] M. A. Sekachev, “Essentially Analytical Theory Closure for Space Filtered Thermal-Incompressible Navier-Stokes Partial Differential Equation System on Bounded Domains,” 2013.

[90] H. Tennekes, J. L. Lumley, J. L. Lumley *et al.*, *A first course in turbulence.* MIT press, 1972.

[91] O. Reynolds, “Xxix. an experimental investigation of the circumstances which determine whether the motion of water shall be direct or sinuous, and of the law of resistance in parallel channels,” *Philosophical Transactions of the Royal Society of London*, no. 174, pp. 935–982, 1883.

[92] J. D. Sterling and S. Chen, “Stability analysis of lattice Boltzmann methods,” *Journal of Computational Physics*, vol. 123, no. 1, pp. 196–206, 1996.

[93] R. Benzi, S. Succi, and M. Vergassola, “The lattice Boltzmann equation: theory and applications,” *Physics Reports*, vol. 222, no. 3, pp. 145–197, 1992.

[94] Y.-H. Qian, D. d’Humières, and P. Lallemand, “Lattice BGK models for Navier-Stokes equation,” *EPL (Europhysics Letters)*, vol. 17, no. 6, p. 479, 1992.

[95] S. Chen, J. Tölke, and M. Krafczyk, “Simulation of buoyancy-driven flows in a vertical cylinder using a simple lattice Boltzmann model,” *Physical Review E*, vol. 79,

no. 1, p. 016704, 2009.

[96] M. Krafczyk, J. Tölke, and L.-S. Luo, "Large-eddy simulations with a multiple-relaxation-time LBE model," *International Journal of Modern Physics B*, vol. 17, no. 01n02, pp. 33–39, 2003.

[97] H. Yu, L.-S. Luo, and S. S. Girimaji, "LES of turbulent square jet flow using an MRT lattice Boltzmann model," *Computers & Fluids*, vol. 35, no. 8-9, pp. 957–965, 2006.

[98] T. B. Benjamin, "Theory of the vortex breakdown phenomenon," *Journal of Fluid Mechanics*, vol. 14, no. 4, pp. 593–629, 1962.

[99] D. Peckham, "Preliminary Results of Low-Speed Wind Tunnel Tests on a Gothic Wing of Aspect Ratio, 1. 0," *Aeronaut. Res. Counc. Tech. Rep*, vol. 508, p. 2504, 1957.

[100] B. Elle, "On the breakdown at high incidences of the leading edge vortices on delta wings," *The Aeronautical Journal*, vol. 64, no. 596, pp. 491–493, 1960.

[101] N. Lambourne and D. Bryer, "The bursting of leading-edge vortices-some observations and discussion of the phenomenon," 1961.

[102] M. Michaud, "Observation d'une trombe de mer faite a Nice de Provence en," *J. Phys. Chim. Hist. Nat. Arts*, vol. 30, pp. 284–289, 1787.

[103] M. Sharma and A. Sameen, "Axisymmetric vortex breakdown: a barrier to mixing," *Physica Scripta*, vol. 94, no. 5, p. 054005, 2019.

[104] I. C. Kim, "Second order bounce back boundary condition for the Lattice Boltzmann fluid simulation," *KSME International Journal*, vol. 14, no. 1, pp. 84–92, 2000.

[105] A. Leonard, "Energy cascade in large-eddy simulations of turbulent fluid flows," in *Advances in Geophysics.* Elsevier, 1975, vol. 18, pp. 237–248.

[106] H. Le, P. Moin, and J. Kim, “Direct numerical simulation of turbulent flow over a backward-facing step,” *Journal of Fluid Mechanics*, vol. 330, pp. 349–374, 1997.

[107] J. Boussinesq, “Theorie de l’ecoulement tourbillant,” *Mem. Acad. Sci.*, vol. 23, p. 46, 1877.

[108] B. E. Launder and D. B. Spalding, “The numerical computation of turbulent flows,” in *Numerical prediction of flow, heat transfer, turbulence and combustion.* Elsevier, 1983, pp. 96–116.

[109] D. C. Wilcox *et al.*, *Turbulence modelling for CFD.* DCW industries La Canada, CA, 1998, vol. 2.

[110] C. D. Scott-Pomerantz, “The k-epsilon model in the theory of turbulence,” Ph.D. dissertation, University of Pittsburgh, 2004.

[111] B. E. Launder, G. J. Reece, and W. Rodi, “Progress in the development of a Reynolds-stress turbulence closure,” *Journal of Fluid Mechanics*, vol. 68, no. 3, pp. 537–566, 1975.

[112] O. Malaspinas and P. Sagaut, “Consistent subgrid-scale modelling for lattice Boltzmann methods,” *Journal of Fluid Mechanics*, vol. 700, pp. 514–542, 2012.

[113] D. R. Noble, S. Chen, J. G. Georgiadis, and R. O. Buckius, “A consistent hydrodynamic boundary condition for the lattice Boltzmann method,” *Physics of Fluids*, vol. 7, no. 1, pp. 203–209, 1995.

[114] V. V. Titov and C. E. Synolakis, “Modeling of breaking and nonbreaking long-wave evolution and runup using VTCS-2,” *Journal of Waterway, Port, Coastal, and Ocean Engineering*, vol. 121, no. 6, pp. 308–316, 1995.

[115] D. R. Fuhrman and P. A. Madsen, “Simulation of nonlinear wave run-up with a high-order Boussinesq model,” *Coastal Engineering*, vol. 55, no. 2, pp. 139–154, 2008.

[116] Y.-L. He, Q. Liu, Q. Li, and W.-Q. Tao, “Lattice Boltzmann methods for single-phase and solid-liquid phase-change heat transfer in porous media: A review,” *International Journal of Heat and Mass Transfer*, vol. 129, pp. 160–197, 2019.

[117] J. Koelman, “A simple lattice Boltzmann scheme for Navier-Stokes fluid flow,” *EPL (Europhysics Letters)*, vol. 15, no. 6, p. 603, 1991.

[118] Y. H. Qian, “Lattice gas and lattice kinetic theory applied to the Navier-Stokes equations,” *Doktorarbeit, Universite Pierre et Marie Curie, Paris*, 1990.

[119] C. Shu, X. Niu, and Y. Chew, “Taylor-series expansion and least-squares-based lattice Boltzmann method: Two-dimensional formulation and its applications,” *Physical Review E*, vol. 65, no. 3, p. 036708, 2002.

[120] J. Fietz, M. J. Krause, C. Schulz, P. Sanders, and V. Heuveline, “Optimized hybrid parallel lattice Boltzmann fluid flow simulations on complex geometries,” in *Euro-Par 2012 Parallel Processing: 18th International Conference, Euro-Par 2012, Rhodes Island, Greece, August 27-31, 2012. Proceedings 18.* Springer, 2012, pp. 818–829.

[121] J. Zhou, “An elastic-collision scheme for lattice Boltzmann methods,” *International Journal of Modern Physics C*, vol. 12, no. 03, pp. 387–401, 2001.

[122] D. H. Rothman and S. Zaleski, “Lattice-gas models of phase separation: interfaces, phase transitions, and multiphase flow,” *Reviews of Modern Physics*, vol. 66, no. 4, p. 1417, 1994.

[123] H. Liu, G. J. Zhou, and R. Burrows, “Lattice Boltzmann model for shallow water flows in curved and meandering channels,” *International Journal of Computational Fluid Dynamics*, vol. 23, no. 3, pp. 209–220, 2009.

[124] T. Toffoli and N. H. Margolus, “Invertible cellular automata: a review,” *Physica D: Nonlinear Phenomena*, vol. 45, no. 1-3, pp. 229–253, 1990.

[125] H. Chen, S. Chen, and W. H. Matthaeus, "Recovery of the Navier-Stokes equations using a lattice-gas Boltzmann method," *Physical Review A*, vol. 45, no. 8, p. R5339, 1992.

[126] Y. Guangwu, "A lattice Boltzmann equation for waves," *Journal of Computational Physics*, vol. 161, no. 1, pp. 61–69, 2000.

[127] K. Zuse, "Rechnender Raum (calculating space)," *Schriften Zur Dataverarbeitung*, vol. 1, 1969.

[128] S. Chen, J. Tölke, S. Geller, and M. Krafczyk, "Lattice Boltzmann model for incompressible axisymmetric flows," *Physical Review E*, vol. 78, no. 4, p. 046703, 2008.

[129] S. Ponce Dawson, S. Chen, and G. D. Doolen, "Lattice Boltzmann computations for reaction-diffusion equations," *The Journal of Chemical Physics*, vol. 98, no. 2, pp. 1514–1523, 1993.

[130] J. G. Zhou, "A lattice Boltzmann method for solute transport," *International Journal for Numerical Methods in Fluids*, vol. 61, no. 8, pp. 848–863, 2009.

[131] W. Graebel, "Engineering Fluid Mechanics. Taylor Francis," 2001.

[132] Q. Zou and X. He, "On pressure and velocity boundary conditions for the lattice Boltzmann BGK model," *Physics of Fluids*, vol. 9, no. 6, pp. 1591–1598, 1997.

[133] G. Zhao-Li, Z. Chu-Guang, and S. Bao-Chang, "Non-equilibrium extrapolation method for velocity and pressure boundary conditions in the lattice Boltzmann method," *Chinese Physics*, vol. 11, no. 4, p. 366, 2002.

[134] O. Filippova and D. Hänel, "Grid refinement for lattice-BGK models," *Journal of computational Physics*, vol. 147, no. 1, pp. 219–228, 1998.

[135] M. Bouzidi, M. Firdaouss, and P. Lallemand, "Momentum transfer of a Boltzmann-lattice fluid with boundaries," *Physics of Fluids*, vol. 13, no. 11, pp. 3452–3459, 2001.

[136] I. Ginzburg and D. d'Humieres, "Multireflection boundary conditions for lattice Boltzmann models," *Physical Review E*, vol. 68, no. 6, p. 066614, 2003.

[137] S. Succi, *The lattice Boltzmann equation: for fluid dynamics and beyond.* Oxford University Press, 2001.

[138] M. S. Ghidaoui, J. Deng, W. G. Gray, and K. Xu, "A Boltzmann-based model for open channel flows," *International Journal for Numerical Methods in Fluids*, vol. 35, no. 4, pp. 449–494, 2001.

[139] F. H. Harlow and J. E. Welch, "Numerical calculation of time-dependent viscous incompressible flow of fluid with free surface," *The Physics of Fluids*, vol. 8, no. 12, pp. 2182–2189, 1965.

[140] D. Yu, R. Mei, L.-S. Luo, and W. Shyy, "Viscous flow computations with the method of lattice Boltzmann equation," *Progress in Aerospace Sciences*, vol. 39, no. 5, pp. 329–367, 2003.

[141] A. J. Ladd, "Numerical simulations of particulate suspensions via a discretized Boltzmann equation. Part 2. Numerical results," *Journal of Fluid Mechanics*, vol. 271, pp. 311–339, 1994.

[142] J. F. Douglas, J. M. Gasiorek, J. A. Swaffield, and L. B. Jack, *Fluid Mechanics.* Pearson education, 2005.

[143] J. Zhou and I. Goodwill, "A finite volume method for steady state 2d shallow water flows," *International Journal of Numerical Methods for Heat & Fluid Flow*, 1997.

[144] K. Grissa, R. Chaabane, Z. Lataoui, A. Benselama, Y. Bertin, and A. Jemni, "Lattice Boltzmann model for incompressible axisymmetric thermal flows through porous media," *Physical Review E*, vol. 94, no. 4, p. 043306, 2016.

[145] W. Wang and J. G. Zhou, "Lattice Boltzmann method for axisymmetric turbulent flows," *International Journal of Modern Physics C*, vol. 26, no. 09, p. 1550099, 2015.

[146] A. K. Gupta, A. K. Gupta, and D. Lilley, *Flowfield modelling and diagnostics*. Taylor & Francis, 1985, vol. 4.

[147] J. Harvey, "Some observations of the vortex breakdown phenomenon," *Journal of Fluid Mechanics*, vol. 14, no. 4, pp. 585–592, 1962.

[148] C. C. Jahnke and D. T. Valentine, "On the Recirculation Zones in a Cylindrical Container," in *ASME International Mechanical Engineering Congress and Exposition*, vol. 18534. American Society of Mechanical Engineers, 1997, pp. 117–124.

[149] H. J. Lugt and M. Abboud, "Axisymmetric vortex breakdown with and without temperature effects in a container with a rotating lid," *Journal of Fluid Mechanics*, vol. 179, pp. 179–200, 1987.

[150] A. Yalagach and A. Salih, "Study of Vortex Breakdown in a Cylindrical Cavity with a Rotating Endwall," *International Journal of Fluid Mechanics Research*, vol. 43, no. 3, 2016.

[151] M. Bertelá and F. Gori, "Laminar flow in a cylindrical container with a rotating cover," 1982.

[152] K. Yamada and K. Suzuki, "Numerical Study on Detailed Structure of Vortex Breakdown Behaviour for Landing of Spaceplane," *Tranactions of the Japan Society for Aeronautical and Space Science, Aerospace Technology Japan*, vol. 14, no. ists30, pp. Pe_77–Pe_85, 2016.

[153] M. Escudier and J. Keller, "Recirculation in swirling flow-a manifestation of vortex breakdown," *AIAA Journal*, vol. 23, no. 1, pp. 111–116, 1985.

[154] C. C. S. da Cruz, L. M. Pereira, E. N. Macêdo, J. N. N. Quaresma, and R. M. Cotta, "Integral transform solution of swirling laminar flows in cylindrical cavities with rotating end walls," *Journal of the Brazilian Society of Mechanical Sciences and Engineering*, vol. 43, no. 8, pp. 1–16, 2021.

[155] S. Bhaumik and K. Lakshmisha, “Lattice Boltzmann simulation of lid-driven swirling flow in confined cylindrical cavity,” *Computers & Fluids*, vol. 36, no. 7, pp. 1163–1173, 2007.

[156] V. L. Okulov, J. N. Sørensen, and L. K. Voigt, “Vortex scenario and bubble generation in a cylindrical cavity with rotating top and bottom,” *European Journal of Mechanics-B/Fluids*, vol. 24, no. 2, pp. 137–148, 2005.

[157] A.-B. Wang, “Strömungen in Rohren mit ringförmigem Hindernis,” Ph.D. dissertation, Universität Erlangen-Nürnberg, 1991.

[158] J. G. Vasconcelos, S. J. Wright, and P. L. Roe, “Numerical oscillations in pipe-filling bore predictions by shock-capturing models,” *Journal of Hydraulic Engineering*, vol. 135, no. 4, pp. 296–305, 2009.

[159] H. Rastgou and S. Saedodin, “Numerical simulation of an axisymmetric separated and reattached flow over a longitudinal blunt circular cylinder,” *Journal of Fluids and Structures*, vol. 42, pp. 13–24, 2013.

[160] T. Ota, “An axisymmetric separated and reattached flow on a longitudinal blunt circular cylinder,” *Journal of Applied Mechanics*, vol. 42, no. 2, pp. 311–315, 1975.

[161] M. Kiya, O. Mochizuki, H. Tamura, T. Nozawa, R. Ishikawa, and K. Kushioka, “Turbulence properties of an axisymmetric separation-and-reattaching flow,” *AIAA Journal*, vol. 29, no. 6, pp. 936–941, 1991.

[162] T. Ota, “A survey of heat transfer in separated and reattached flows,” 2000.

Appendix A

Publications

1. Journal name: *MATERIALS EVALUATION*, ISSN: 0025-5327

Article title: Numerical study on the vortex breakdown flows in an enclosed cylinder with a rotating endwall

Farokh Morakabi[1], *Jian Zhou*[2], *Tariq Jarad*[3]

The article will be published in the 2nd Issue of volume 81.

2. Journal name: *INTERNATIONAL JOURNAL OF MATHEMATICS FOR INDUSTRY*, IJMI-D-22-00017

Article title: Incorporation of the 2nd order-accurate bounce-back scheme into axisymmetric lattice Boltzmann revised method

Farokh Morakabi[1], *Jian Zhou*[2], *Tariq Jarad*[3]

The article is under review.